POLITECNICO
MILANO 1863

School of Industrial and Information Engineering
Department of Physics

Master of Science Thesis

Charge density fluctuations in unconventional cuprate superconductors: a comparative analysis between experimental data and theoretical model

Supervisor:

Prof. Marco Moretti

Co-Supervisors:

Dr. Riccardo Arpaia

Candidate:

Pietro Camisa (**920817**)

Academic Year 2019 – 2020

Charge density fluctuations in unconventional cuprate superconductors: a comparative analysis between experimental data and theoretical model

Master of Science Thesis
April, 2021

By Pietro Camisa

Published by: Politecnico di Milano, Department of Physics, P.zza Leonardo da Vinci 32, Building 8, 20133 Milano (MI) Italy
www.fisi.polimi.it/en

Dare un senso, questo compito
resta assolutamente da assolvere,
posto che nessun senso vi sia già.

Friedrich Nietzsche

Abstract (ENG)

This thesis is developed in the context of the study of cuprate superconductors: a promising class of high-T_c superconductors, by means of Resonant Inelastic X-ray Scattering (RIXS). RIXS measurements of cuprates show a variety of interesting phenomena, among which are charge density waves (CDW) and recently discovered charge density fluctuations (CDF): two rather exotic types of charge order excitations which still lack a widely accepted theoretical description. The purpose of this thesis is to develop the computational analysis of a recently proposed model by first running simulations with reasonable guesses of parameters, and then, most importantly, extracting a range of physically relevant parameters through a global fit of experimental data collected at various temperatures on high quality YBCO and BSCCO samples. Results encouraged an exciting discussion regarding the physics behind charge density modulations and their interplay with other phenomena, and yielded promising matches between theory and experiment in the whole temperature range under scrutiny.

Abstract (ITA)

Questa tesi si sviluppa nel contesto dello studio dei cuprati superconduttori: una promettente classe di superconduttori ad alta temperatura critica, tramite lo scattering risonante ed inelastico di raggi X (RIXS). Le misure RIXS sui cuprati mostrano una gran varietà di fenomeni interessanti, tra i quali troviamo le "charge density waves" (CDW), i.e. onde di densità di carica, e le "charge density fluctuations" (CDF), più recentemente scoperte: due tipi piuttosto esotici di eccitazioni dell'ordine di carica per i quali ancora non esiste una descrizione teorica ampiamente condivisa. Lo scopo di questa tesi è quindi quello di sviluppare un'analisi computazionale di un modello recentemente proposto, tramite -in primo luogo- una simulazione facente uso di un set ragionevole di parametri e -in secondo luogo- estraendo dei parametri fisicamente rilevanti attraverso un fitting globale dei dati sperimentali, raccolti a diverse temperature su campioni di YBCO e BSCCO (ad alta qualità). I risultati ottenuti hanno incoraggiato una stimolante discussione in merito alla fisica delle modulazioni della densità di carica elettronica e delle loro interazioni con altri fenomeni fisici, e hanno prodotto interessanti corrispondenze tra teoria ed esperimento nell'intero intervallo di temperature preso in considerazione.

Introduction

Through the fall semester of 2020 and the beginning of 2021 I've had the opportunity to join the research team lead by Giacomo Ghiringhelli at the Department of Physics of Politecnico di Milano. This group has a solid and well established expertise in the branch of experimental physics performed through soft X-ray spectroscopy at synchrotron facilities, for the study of electronic and magnetic properties of matter. At the heart of their activity is a technique called RIXS: Resonant Inelastic X-ray Scattering, which is a cutting-edge technology suitable for the investigation of excitations bound to the charge, spin, orbital, lattice degrees of freedom in systems with strong electron correlation. The group has pioneered the development of this technique and of its applications, providing an enlightening, innovative and often complementary, perspective with respect to the previously known techniques (such as X-ray Absorption Spectroscopy (XAS), Inelastic Neutron Scattering (INS) and many more) in the world of experimental physics for the study of suitable systems.

Since 2009 the group has coordinated its efforts towards the investigation of materials based on $3d$ transition metals oxides ($3d$TM in short), which offer an abundance of electronic and magnetic properties thanks to their strong electron correlation; and more specifically to superconductive layered copper oxides. These are a class of peculiar quasi-bi-dimensional structured materials which exhibit superconductive behavior at relatively high temperatures, constituting an extremely exciting and promising frontier for research, yet one of the longest standing problems of contemporary solid state physics due to the lack of a deep understanding of the mechanisms regulating their properties.

A thorough study of cuprates using RIXS is unveiling the existence of many physical phenomena, among which we find charge density waves (CDW) and fluctuations (CDF) which are rather exotic and intriguing types of charge density oscillations, occurring in specific regions of these crystals' reciprocal space. The fast-paced quest for an extensive understanding of the nature of cuprates, and therefore also of all related phenomena such as CDW and CDF, is leading experimental physicists to collect data and theorists to formulate models. The aspiration is that the scientific community will soon be able to provide accurate predictions and insights into the physics behind charge order, and the role it might play in superconductivity.

Following the exciting and possibly revolutionary findings of recent experimental activities ([1],[2]), this thesis arises in the context of seeking a match between the RIXS experimental data collected by our research group at various synchrotron facilities throughout Europe, and a mathematical model developed by a team of theoretical physicists at Universitá la Sapienza, Rome, lead by Carlo Di Castro.

The first chapter will be devoted to a brief introduction on highly correlated systems and superconductivity, and to a description of $3d$TM-based systems, with a closer look on layered copper oxides (cuprates). It will end with an overview of the most up-to-date findings on charge density modulations.

The second chapter will commit to the characterization of the RIXS experimental technique, and a presentation of the excitations it can get access to.

The third chapter will specifically focus on the experimental data used for the analysis and on the mathematical model which will be at the heart of the simulations. I will then provide the first results which emerge from the implementation of the model by using a reasonable set of physical parameters, and by quantitatively exploring what role each of them plays in the simulated intensity signal; paving the way for the central part of the work: the global fit.

The fourth chapter introduces the logic behind the fitting scheme and focuses on the methods adopted to face the main challenges related to finding a match between experimental data and simulations. Among these the presence of a background, an elastic peak in Γ and the temperature dependence of the characteristic frequency of CDF: ω_0. Then the outcomes of the fit are displayed, together with an explanation of where it provides encouraging insights, highlighting its limits and their possible explanation.

In the conclusions I summarize the main results of the project and provide a concise description of its successes and limits, and how they encourage further research and analysis. Hence, I present a range of thrilling future perspectives pointed out by the findings of this work, which involve the interplay of a wide variety of physical phenomena and experimental techniques.

In Appendix A and B the reader can find (respectively) a brief remark on computation times and the code used for the fit.

Lastly, I shall note that due to the Covid-19 pandemic I was unfortunately not able to attend in person any of the measurements sessions at the beamlines of synchrotrons, and therefore my work closely focused on the data analysis and interpretation.

Contents

List of Figures

1 $3d$TM-based systems

1.1 Highly correlated systems

One of the most active branches of contemporary solid state physics is that which investigates the nature and properties of the so called *quantum materials*, i.e. systems which exhibit *strong electronic correlations*.

In such structures, the electron-electron interaction taking place within the valence band is non-negligible, and has to be taken into account beyond the perturbative correction. The single particle description provided by one-electron theories fails to reproduce their observed physical properties due to the intermediate character of the valence electron wave functions, neither localized on the atoms nor totally spread over the whole solid. Put simply, we have to discard the approximation of considering an identical Hamiltonian for every electron, which decouples their wave functions by accounting for their mutual interactions through the use of a mean-field approach. In certain quantum materials, the divergence from the behavior predicted by one-electron theories is so large that instead of behaving as metals with a conductive band cutting the Fermi level, they are instead insulators with wide band gaps (at least at room temperature). This is the case for ceramic high temperature superconductors based on CuO_2 layers, which exhibit a poorly conducting antiferromagnetic phase below their Néel temperature (~ 300 K) and a superconductive phase below a critical temperature T_c.

In principle, many body calculations should be employed to provide a more physical characterization of the structure of these materials, nevertheless many body theories rely on technical mathematical representations, such as density functional theory (DFT)[3], and are beyond the purpose of this work, which favors an experimental approach.

A general discussion of the electronic structure of transition metal (TM) oxides can be found in [4].

Several systems based on $3d$ transition metals fall within the definition of quantum materials. In such structures, which we will refer to as $3d$TM, the open $3d$ shell is

sufficiently atomic-like to lead to strong electronic correlation and localized magnetic moments; but also radially extended enough to form highly covalent bonds with partnering anions, resulting in large hopping integrals and strong superexchange interaction. This explains the very rich phenomenology of these systems, which exist in various forms (alloys, oxides, calchogenides...) and is reflected in the fact that their crystalline structure, local orbital symmetry, atomic spin orientation and charge density are all coupled and have comparable energy scales, leading different orders to compete and/or cooperate, and allowing the existence of a variety of exotic phases (such as high critical temperature superconductivity in layered copper oxides [5]).

1.2 High T_c superconductors

Superconductors are systems which, below a certain critical temperature T_c, undergo a phase transition to the so-called superconducting state, characterized by an identically null resistivity and a magnetic field repellent condition.

Superconductors hint at one of the most desirable technological applications of solid state physics: loss-free electricity transfer. As one can easily imagine, such a discovery would completely revolutionize the energy sector and the whole world as a consequence; nevertheless there remain a huge challenge standing in the way of such a scientific leap: the temperature (or pressure [6]) ranges required to enter the superconductive state of currently studied materials.

Conventional superconductors, described by BCS theory [8] rely on a well understood mechanism of phonon-mediated coupling of electrons, (see Fig. 1.2) which leads to a breakdown of the resistance below T_c. In simplified terms, electrons involved in the mentioned pairing are endued with opposite momenta and opposite spin: they are in a singlet state. These paired particles, called *Cooper Pairs*, are therefore bosons and, according to the Bose-Einstein distribution, are increasingly more likely to populate the (same) ground state as T decreases. Below the critical temperature Cooper pairs condense in a bosons superfluid and this causes, as a macroscopic effect, the insurgence of the superconductive state. Fundamental to the BCS mechanism is the fact that, despite the strong direct Coulomb repulsion, the relatively weak attractions between electrons induced by the coupling to the vibrations of the lattice (phonons) can bind the electrons into pairs at energies smaller than the typical phonon energy [9]. These materials have been studied for decades

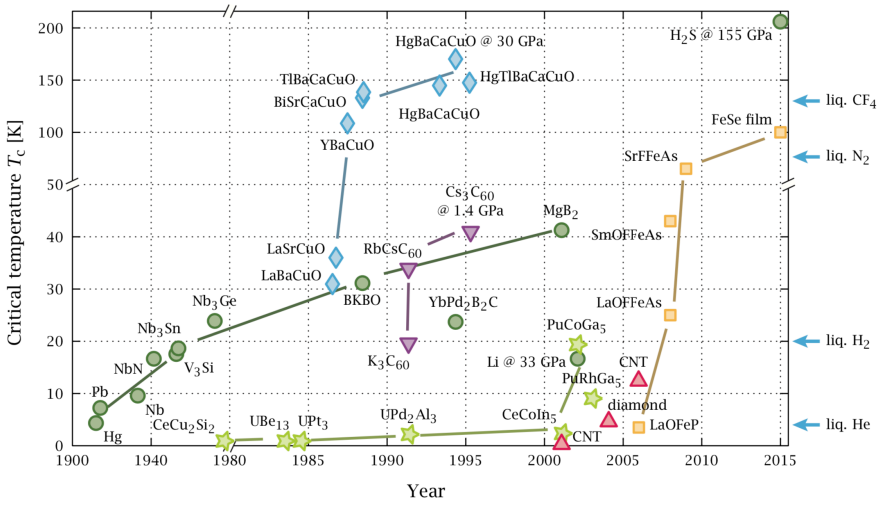

Figure 1.1: T_c versus time. Superconducting transition temperatures versus year of discovery for various classes of superconductors. Note in particular BCS superconductors (green circles), cuprates (blue diamonds), and iron-based superconductors (yellow squares). Fig. from [7]

and are characterized to a satisfactory extent by the current depiction; their critical temperatures vary depending on the specific material, nonetheless they remain quite low, (the current 'record' is held by MgB_2 with T_c around 40 K) as can be observed in figure 1.1.

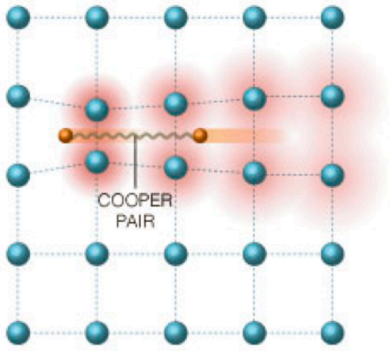

Figure 1.2: A naive depiction of the mentioned phonon-mediated pairing mechanism which leads to superconductivity in the BCS framework.

In 1986 Bednorz and Muller discovered that a certain class of materials (cuprates, indeed) entered the superconductive state at a relatively high temperature (as high as 138 K at atmospheric pressure), forbidden by canonical BCS theory [10]. In gen-

eral, for this class of materials, the mechanisms behind BCS do not fit or justify the experimentally observed behavior. For example, whereas in conventional superconductors the superconducting electrons wavefunctions have the same symmetry of the underlying lattice, in high temperature cuprate superconductors unconventional symmetries arise (see *unconventional pairing* in [11]). Despite the fact that a thorough description of superconductivity falls well beyond the purpose of this work, it is interesting to point out that a coherent and complete theory explaining the mechanisms behind high-T_c superconductivity is still missing. This encourages the further development of a broad range of experimental techniques such as inelastic neutron scattering (INS), X-ray absorption spectroscopy (XAS), resonant inelastic X-ray scattering (RIXS) and many more, and calls for novel theories to be formulated and tested.

It must be noted that in the study of highly correlated $3d$TM-based systems and, specifically, layered copper oxides, it is crucial to to understand also the physics behind the normal state from which the superconductive (SC) state emerges, and all the other unconventional phases and exotic elementary excitations that can take place (such as phonons, magnons, paramagnons, charge density fluctuations and so on).

1.3 Layered copper oxides

We refer to layered copper oxides as *cuprates*, these materials are the only ones currently reliably known to be SC at ambient pressure above the boiling point of liquid nitrogen (77 K) thus having great practical as well as theoretical interest [10]. In general, the peculiar physical properties of cuprates derive from their electronic structure. Indeed, differently from what happens in most $3d$ transition metals, where the conduction of electrons takes place in bands which originate (in the sense of a tight-binding calculation) from the $3d$ orbitals, in cuprates there is a fair degree of O($2p$)–Cu($3d$) hybridization [12], and therefore the electronic band which dictates a significant portion of their properties has non-negligible contributions from both the $3d$ orbitals of copper and the $2p$ orbital of oxygen; this is a distinctive and fundamental characteristic arising from the very narrow energy difference between those orbitals.

Despite cuprates having appreciable size in all 3 dimensions, their physical properties are bound to CuO_2 layers which constitute a powerful example of two dimensional

systems. In the CuO_2 plane, copper atoms are in the Cu^{2+} ionization state, thus manifesting a $3d^9$ electronic configuration (starting from $3d^{10}4s$ of Cu) in which nine of the ten available $3d$ orbitals are filled up [13]. The presence of oxygen ligands surrounding copper atoms, both in plane (i.e. in the CuO_2 plane) and out of plane, due to their geometrical coordination within the cell, breaks the spherical symmetry of the potential that Cu^{2+} ions are subject to and lifts degeneracy in energetic levels having the same quantum numbers, i.e. among $3d$ orbitals in this case. These systems can have various coordination polyhedra: octahedral, pyramidal or squared (see Fig. 1.3). For example, in the octahedral case there is a 6-fold coordination, where the $3d$TM cation is at the center of an octahedron and the ligands lie at the vertices. In this case the in-plane distance between Cu and O atoms is roughly $\sim$ 1.9 Å, while the distance from out-of-plane oxygen atoms (called apical oxygens) is $\sim$ 2.4 Å[14]; each crystal can present an indefinite number of planes, separated by a *spacing layer*. The interlayer distance typically ranges from about 6 to 15 Å, being much larger than the in-plane lattice constant, in addition much of the inter-plane material is fairly insulating while the CuO_2 planes are conducting, this means that cuprates are strongly anisotropic, and this partially makes sense of the fact that their properties are mostly determined by the behavior of the electrons (holes) in the CuO_2 planes, as mentioned. Moreover, for the same motivation it is thus not surprising that they show a fair degree of universality [14].

A simple representation of the periodical repetition of two-dimensional unit cells of a cuprate, together with the most important electronic orbitals, Cu $d_{x^2-y^2}$ and O p_σ, are shown in figure 1.4. Its respective reciprocal lattice unit cell is found in figure 1.5. The representation in reciprocal space is fundamental in regards to this work given that, during a RIXS experiment, incident and scattered x-ray photons have to obey momentum conservation, and therefore their exchanged momentum is a significant vector in the solid's reciprocal space. This will be explained more in detail later on, but it is enough to understand that, depending on the incidence angle of the incoming beam with respect to the sample, different regions of its reciprocal space will be probed. The data that will be used for the analysis described in the following chapters was collected sampling points along the (H,0) and (H,K=H) directions (respectively Γ-X and Γ-M directions in figure 1.5).

In particular, considering an octahedral geometry of the surrounding oxygen anions, the five $3d$ orbitals split into two groups called t_{2g} and e_g according to their symmetry (as represented in Fig. 1.6). t_{2g} orbitals, identified as *yz, xz, xy*, are the lowest-energy ones since their electronic spatial distribution is such that Coulombian repulsion with

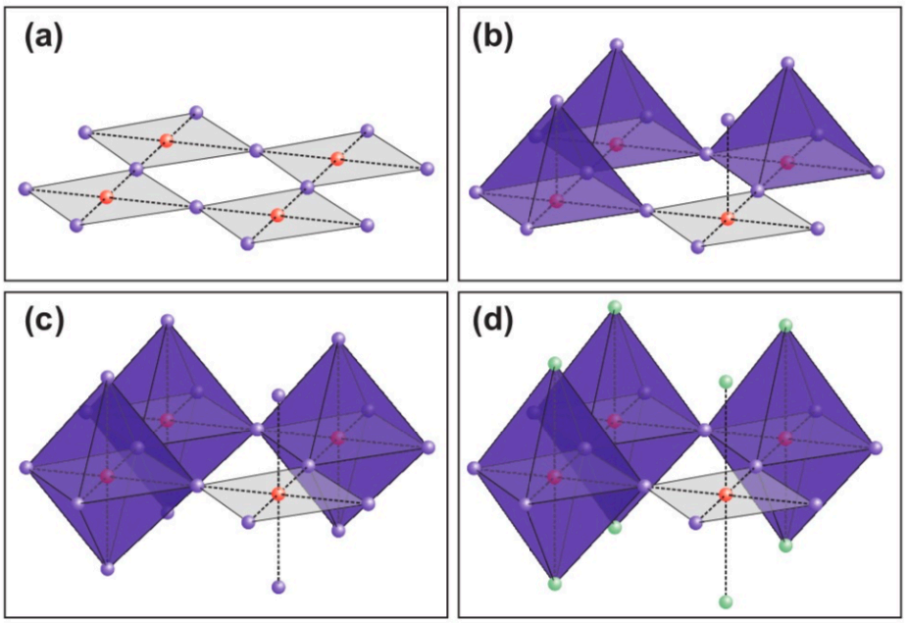

Figure 1.3: Some of the possible coordination polyhedra in cuprates. In (a) we have the CuO_2 plane. In (b), (c), (d) we have different geometrical coordinations of the ligands. Fig. from [15]

neighboring oxygen ions is minimized, while e_g orbitals, specifically $x^2 - y^2$ and z^2, have higher energies. Moreover, the octahedral geometry can be regular or distorted: if a pair of opposite ligands is farther or closer to the center than the other four, i.e. if two in-plane unit cell vectors, namely a and b are slightly different from each other, a tetragonal distortion is present and the actual geometry is orthorombic. Due to the departure from a cubic crystalline field, degeneracy is lost also among orbitals within each single group.

A one-electron theory would predict a metallic behavior for cuprates because of the

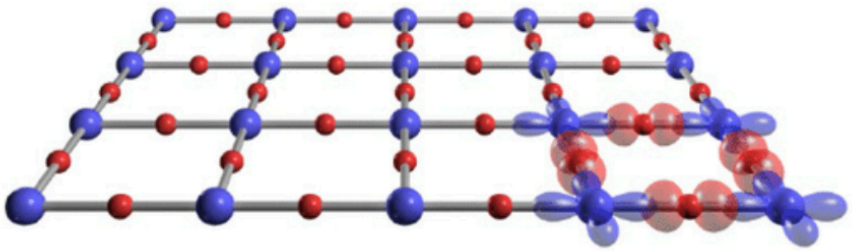

Figure 1.4: The universal building block of high-T_c cuprates: the CuO_2 sheet, formed by the periodical repetition of a square lattice. The most important electronic orbitals, Cu $d_{x^2-y^2}$ and O p_σ, are shown. (Copper atoms in blue and oxygen atoms in red). The interatomic distance between copper atoms is a ~ 3.8 Å. Fig. from [16]

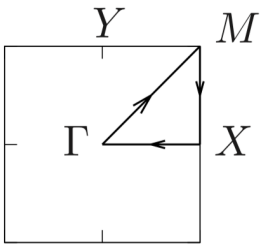

Figure 1.5: Typical representation of a 2D square lattice in reciprocal space showing high symmetry points and directions. We refer to the Γ-X direction as (H,0) or simply H0, and to the Γ-M direction as (H,H) or simply HH.

presence of a non completely filled outer shell (the $3d$ shell, indeed). Nevertheless, in these systems, the energy associated with an electron hopping from a ligand site to a metal site, known as *charge transfer energy*: Δ, is non-negligible, where $\Delta = \mathrm{E}(\mathrm{d}^{n+1}\mathrm{L}) - \mathrm{E}(\mathrm{d}^{n})$, and L represents a hole on the ligand site. This is clearly not taken into account by one-electron theories and introduces an energy gap (typically on the order of a few eV) which forces cuprates to be insulators, or more precisely Mott charge-transfer insulators, at room temperature [18].

Cuprates also show interesting magnetic properties: each Cu^{2+} ion in the CuO_2 plane has spin 1/2 and spins arrange themselves in an antiferromagnetic fashion, parallel to the CuO_2 layer (see Fig. 1.7). The process behind such an arrangement is a super-exchange mechanism [19] mediated by oxygen, that can be well described by a bi-dimensional Heisenberg model (more on magnetic ordering in [15]). Magnetic excitations in cuprates offer a rich phenomenology and their study through techniques such as neutron scattering or RIXS is of utmost relevance in the contemporary solid state physics debate.

Layered copper oxides as have been described so far, as mentioned, are electric insulators. In order to allow the insurgence of the superconductive state, cuprates (of every kind) have to be doped with extra holes or electrons in the CuO_2 plane by acting on the chemical composition of the material outside the plane (in the so-called *charge reservoir* layers). Actually, the critical temperature which determines the phase transition to the SC state is a function of doping, this allows us to map the behavior of cuprates in *phase diagrams* as a function of temperature and doping level; we call *optimal doping* the value associated to the highest T_c for a given material. As it turns out SC is only one among many exotic phases in which cuprates can be found, and each of them entails properties very much different from the others. Among these we find the pseudo-gap state, the strange-metal state, the antiferromagnetic

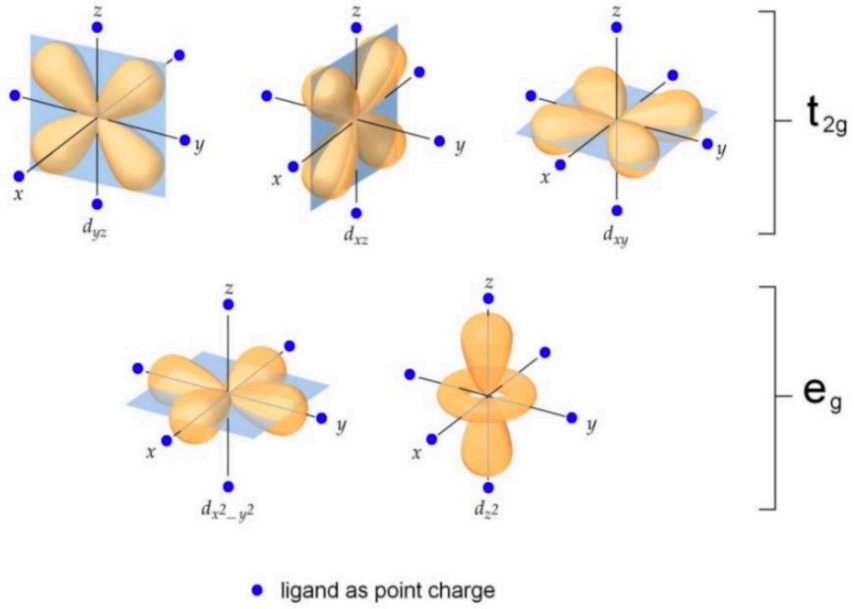

Figure 1.6: Cu d orbitals splitting in energy due to the lower symmetry of the system, using a crystal field approach. Electronic configurations which minimize Coulombian repulsion with oxygen ligands are the most stable in energy. Fig. from [17]

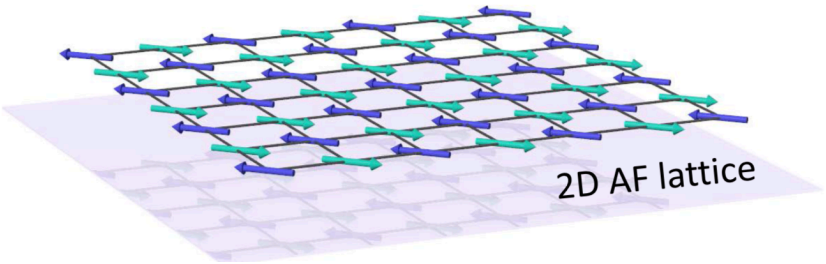

Figure 1.7: Simple representation of a 2D antiferromagnetic (AF) lattice. Fig. from [20]

state and, of course, the superconductive state. Also interestingly, in given domains of doping and temperature, phenomena such as spin density (SDW) waves and charge density waves (CDW) can take place, where the latter will be of foremost relevance for this thesis. In figure 1.8 one can observe a typical phase diagram of cuprates.

Note that what controls the interesting behavior of cuprates (in the sense of phase transitions) is the number of doping-induced extra carriers in the CuO_2 plane, more often than not p-carriers i.e. the number of holes per CuO_2-unit below and above the value (namely 0) of the stoichiometric parent compound (i.e. the undoped cuprate), moreover it becomes of key importance to ascertain the relation between p and the chemical stoichiometry [14].

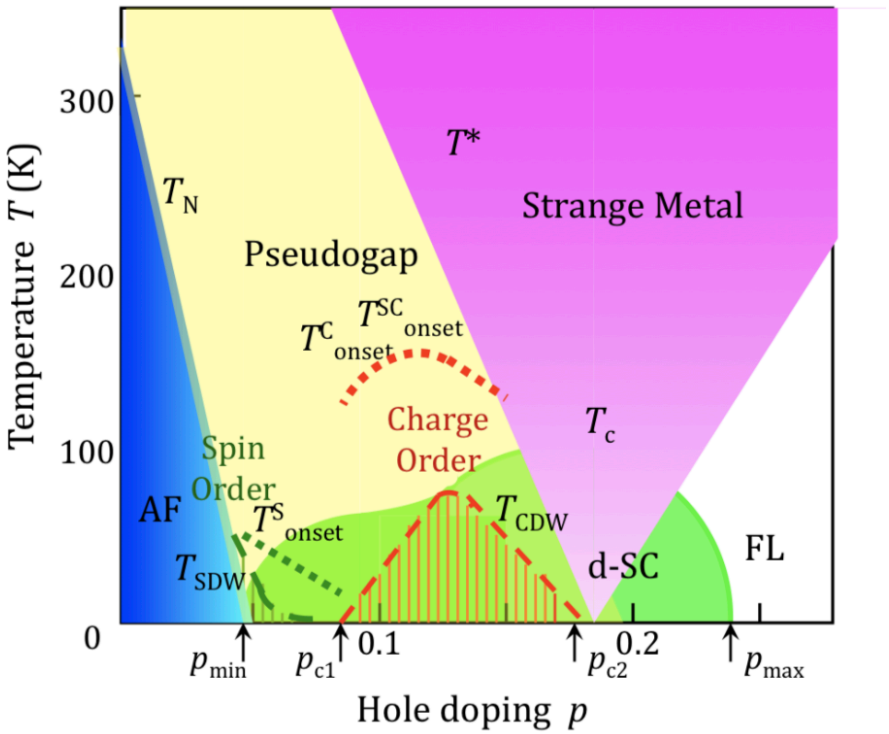

Figure 1.8: Phase Diagram. Temperature versus hole doping level for cuprates, indicating where various phases occur. AF is antiferromagnetic, d-SC d-wave superconductivity, and FL Fermi liquid. SDW and CDW represent incommensurate spin density wave and charge density wave order. "onset" marks where precursor order or fluctuations become apparent. Fig. from [9]

1.3.1 YBCO

Yttrium Barium Copper Oxide (generally informally referred to as YBCO) is a variety of high-T_c superconducting cuprate crystal. It includes the first SC material ever recorded to have a critical temperature above the boiling point of liquid nitrogen (77 K) at around 93 K, discovered in 1987 [21]. Most YBCO compounds have the general formula $YBa_2Cu_3O_{7-\delta}$ (also known as Y123), where δ is used as a doping level controller, and the *parent compound* is $YBa_2Cu_3O_6$. As already mentioned for cuprates by and large, their SC properties are strongly dependent on doping, this is the case for YBCO in particular, where the SC state emerges for $0 \leq \delta \leq 0.65$ below the relative T_c, and has a maximum value of $T_c \approx 95$ K at p ≈ 0.16 (holes per Cu atom).

YBCO compounds crystallize in layered-perovskite structures, with the presence of now-well-known CuO_2 layers. Parallel to those planes are CuO chains (laying in top and bottom planes of Fig. 1.9), which act as a charge reservoir when YBCO is

hole-doped. Yttrium atoms are found between CuO_2 planes, and barium atoms are located between CuO chains and CuO_2 planes [13], the structure is represented in figure 1.9.

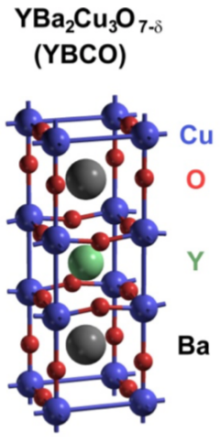

Figure 1.9: Crystal structure of YBCO. Fig. from [16]

It should be noted that neighboring planes may be shifted by (1/2, 1/2) relative to one another, so that the true crystallographic unit cell contains *two* CuO_2 planes. The BaO layers, called spacing layers or buffer layers, are more or less independent of δ.

Experimental data analyzed in the following chapters is relative to a *slightly overdoped* YBCO sample, having hole doping p $\approx$ 0.19, whereas the optimal doping is found at p $\approx$ 0.16. The reason for this doping choice will be detailed more carefully in Sect. 1.4. The sample was grown by pulsed laser deposition (PLD) at Chalmers University, Göteborg and the doping was regulated actively controlling the oxygen pressure in the chamber during the post-annealing process which brings the sample's temperature down from $\sim$ 750 C° to room T [22]. The quality of the sample was determined through a thorough work of characterization which can be found in Ref. [23].

1.3.2 BSCCO

Bismuth Strontium Calcium Copper Oxide (generally informally referred to as BSCCO), is another type of cuprate high-T_c superconductor. Its studied stoichiometries vary depending on the number of the metallic ions which it contains. The variant we considered belongs to the category commonly referred to as Bi2212, hav-

ing stoichiometry $Bi_2Sr_2CaCu_2O_{8+x}$. Similarly to YBCO, BSCCO crystallizes in a layered-perovskite geometry, with BiO–SrO–CuO_2–Ca–CuO_2–SrO–BiO stacking of crystallographic planes, characterized by a weak, van der Waals-type bonding between adjacent BiO layers [12]. BSCCO needs to be hole-doped with an excess of oxygen atoms to superconduct, and the optimal doping for Bi2212 is around $p \approx 0.16$, which leads to $T_c \approx 98$ K. Bi2212 was the second compound in which charge order was ever observed in 2002 through STM studies by Hoffman *et al.* in Ref. [24]. In our case, the sample which will be analyzed was grown at the Institute of Physics, Beijing and is (again, as for YBCO) slightly overdoped: $p \approx 0.19$. The sample quality is testified by the work done in Ref. [23].

1.4 Charge Density Modulations

The phenomenon of charge order in solids consists in a broken-symmetry state occurring when valence electrons self-organize into periodic structures incompatible with the symmetry of the underlying lattice [12]. Charge density waves constitute indeed a rather peculiar phenomenon, being periodic modulations of conduction electron density typical of highly correlated systems. In these structures the on-site Coulomb repulsion between two electrons in the same d orbital can overcome the kinetic energy part of the Hamiltonian, inducing the electronic distribution to find new ways to lower its total energy, often by spontaneous breaking of the native symmetries of the lattice [12]. Charge density modulations are often found in low-dimensional systems such as $NbSe_2$ or different types of copper layered oxides [25], where they originate in CuO_2 planes in correspondence of well defined incommensurate wave vectors values denominated Q_c, thus breaking the translational symmetry of prototypical orbitals.

Actually, charge density modulations of some kind have been observed in all families of high–critical temperature superconducting cuprates, and they are consistently found in the underdoped region of phase diagrams at relatively low temperatures (see Fig. 1.10). Nevertheless, despite being such a widespread phenomenon, it is still debated to what extent they influence the unusual properties of these systems in broad terms [1].

Over the last decade, interest in this field has been fueled by evidence that unconventional superconductivity arises more often than not in the vicinity of another ordered electronic state, and a wealth of experimental results has suggested the pres-

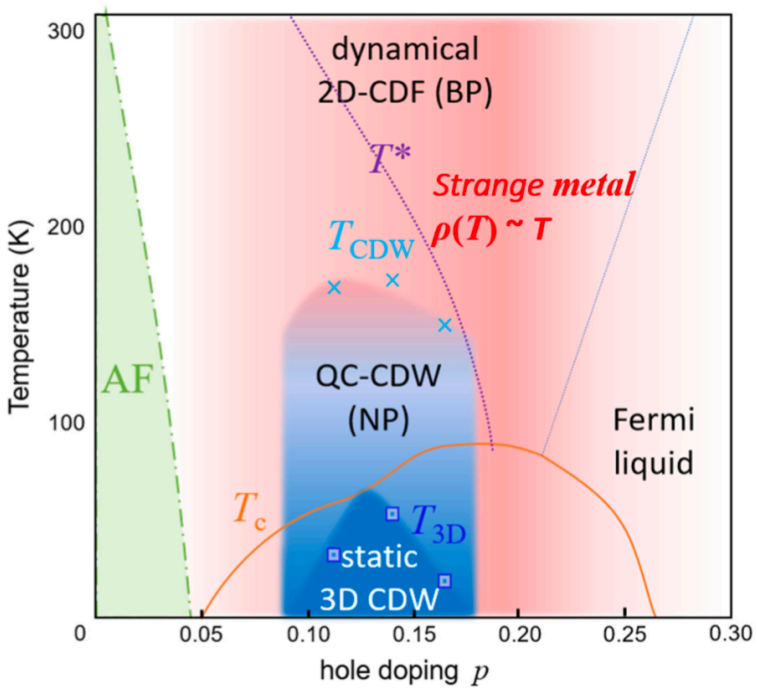

Figure 1.10: Phase diagram T vs p-doping of YBCO

The green zone is the antiferromagnetic phase. In the cone above optimal doping between T^* and the Fermi liquid the Strange Metal phase is found. In the light-blue shaded area below T_{CDW} we find quasi-critical CDW responsible for the NP, whereas in the darker blue triangular area we find 3D static CDW characterized by long-range order (hidden in absence of high magnetic fields because of their competition with SC). The reddish area represents 2D dynamical CDF (BP). Figure from [26].

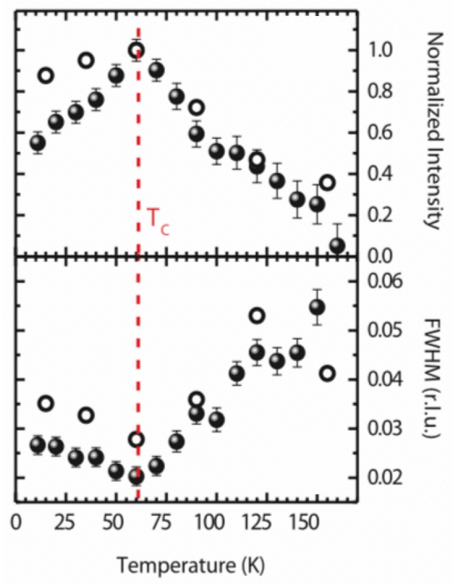

Figure 1.11: Evidence of competition between CO and SC.
Temperature evolution of the charge order peak intensity (above) and full-width-at-half-maximum (below), showing a cusp at T_c, thereby providing evidence of competition between charge order and superconductivity. RIXS-measured data readapted from [2].

ence of forms of charge order in the pseudogap region of the cuprate phase diagram, thus underlying a possible connection between the two [27]. Moreover, experimental results using nuclear magnetic resonance (NMR) in strong magnetic fields [28], and elastic X-ray scattering [29] have confirmed the similar energy scale of charge density modulations and superconductivity in YBCO. Nevertheless, strong evidence has emerged that these two processes actually compete with each other, being CDW quenched by SC below T_c, while otherwise appearing also at lower temperatures in the presence of intense magnetic fields which prevent the onset of superconductivity. Indeed, RIXS intensity and FWHM data indicate a clear weakening of the charge ordered (CO) state both in its amplitude and spatial correlations at the emergence of the superconducting state [12], as can be observed in Fig. 1.11.

As it also occurs for high-T_c in cuprates in general, a widely accepted theory of CDW, inclusive of what triggers their onset, what other phenomena they are bound to, how they respond to variations of temperature, doping, material and so on, is still missing. Nonetheless, an increasing amount of scientific research is being carried out, and experimental evidence is being collected all around the world, encouraging and guiding the efforts of physicists in unraveling the true nature of charge density modulations in quantum materials.

In some theoretical scenarios being proposed by contemporary solid-state physics theorists, charge density modulations are pivotal to the anomalous characteristics of cuprates; in such models they are expected to permeate, through dynamical *charge density fluctuations* (CDF), a broad range of the phase diagram. RIXS measurements of YBCO, BSCCO and NBCO ($NdBa_2Cu_3O_{7-\delta}$) have recently found evidence to support such theories, strengthening the idea that charge density modulations might be crucial in the determination of normal properties of cuprates [1]. This, as we will see, has triggered much interest in seeking a correspondence between latest measurements and most up-to-date models, and is the starting point of this thesis.

One of the most prominent ways in which experimental evidence of the existence of charge density modulations is manifested, is through the presence of quasi-lorentzian peaks in the RIXS quasi-elastic scattered intensity obtained scanning reciprocal space along the (H,0) direction (i.e. Γ-X direction in figure 1.5), as can be observed in figure 1.12. Notably, the existence of four similar in-plane modulations ($\pm Q_c$,0) and (0,$\pm Q_c$) indicates that they are associated to the (nearly square) CuO_2 planes rather than the CuO chains, and this, along with their weak (close to non-existent) correlation in the direction perpendicular to the planes, makes them a bi-dimensional phenomenon [30] [31].

Notably, in this thesis I will resort to reciprocal lattice units (r.l.u.) to quantitatively map wavevectors in momentum space. Reciprocal lattice units represent a notation where wavevectors are expressed as Q = (H,K,L), corresponding to Q = (H·$2\pi/a$, K·$2\pi/b$, L·$2\pi/c$) in physical units (typically $Å^{-1}$). Also, I will refer wavevectors to the undistorted unit cell, where a and b axes (and correspondingly the reciprocal axes H and K) are parallel to the Cu-O bond directions with lattice parameters equal to the nearest Cu-Cu distance. Whenever c (and correspondingly L) is omitted, it means the discussion refers to phenomena taking place in CuO_2 planes (and respectively to their reciprocal lattice), so $c = L = 0$.

An extremely interesting recent observation in RIXS data collected on underdoped YBCO and NBCO (see Fig. 1.12) is the presence of both a narrow peak (NP), which shows all characteristics of medium-ranged incommensurate CDW widely found in underdoped cuprates, and the existence of a broader peak (BP) which shares with the NP the position in reciprocal space (besides a small amount), *but* displays a far weaker temperature dependence [1]. The larger width of the BP (in momentum space) is reflected onto its correlation length ξ through a sharp decrease, given that $\xi \sim \frac{1}{FWHM}$, it is therefore attributed to very short-ranged charge modulations (i.e. $\xi_{CDF} \approx 3$ *lattice spacings* [26]) which, for this reason, have been called charge density

fluctuations and not *waves*. Indeed, the CDW-related narrower peak implies a correlation length of several lattice spacings, which actually keeps increasing at lower temperatures, supposedly reaching divergence at a putative CDW quantum critical point (QCP), e.g. located at p $\sim$ 0.17 in YBCO [32] corresponding to the lower-right corner of the dark-ish blue triangle in Fig. 1.10. At low T, ξ_{CDW} is so large that CDW become correlated also in the direction perpendicular to CuO_2 planes, giving rise to what has been identified as 3D charge density waves (indicated with a dark-ish blue triangular area in Fig. 1.10). These are not of immediate detection, given that at such low temperatures huge magnetic fields are needed to quench superconductivity, which otherwise ends up competing with (and suppressing) charge order. Vice versa $\xi_{CDW} \rightarrow \xi_{CDF}$ when T is raised, suggesting, possibly, a common origin of the two phenomena, backed up by their almost equal wave vectors Q_c. Interestingly, CDF have been found to permeate a much broader portion of cuprates' phase diagrams with respect to CDW, occurring also well above the pseudogap temperature T^* and in a larger doping range, thus supposedly constituting the *bulk* of the iceberg of charge density excitations. The energy of CDF is doping dependent, being higher at lower doping, whereas its temperature dependence is still quite debated and we will take me time to discuss it in the following chapters. It is indeed this particular phenomenon (i.e. CDF) that will be the subject of the fitting at the heart of this thesis.

By exploiting the high energy-resolution of RIXS measurements, it is possible to extract estimates of the characteristic energy of these charge modulations. Results point at an $\omega_0^{BP} \approx 15$ meV, whereas the energy of the NP is found to be fairly elastic. This gives on to the idea that the NP has nearly-static nature, whereas the BP is the result of a dynamic fluctuation.

Moreover, high energy X-ray scattering and NMR experiments have confirmed that the medium-range charge order associated to CDW is truly static, and one of the hypotheses is that these static CDW might arise from pinning of correlated charge fluctuations by defects which are always present in any sample [25].

As observed in Ref. [1], two-dimensional dynamical CDF carry with them most of the overall scattered intensity (volume of the associated BP) at every temperature, and pervade a large portion of the phase diagram of cuprates (see red-shaded area in Fig. 1.10): this places them quite at the center of the discussion regarding charge order in these materials. Also, quite notably, they do not compete with superconductivity (as CDW do [28] [29] [33] [30]), and therefore are not quenched at subcritical temperatures; this allows their detection also in systems in which

static CDW would be undetectable, being their onset temperature lower than T_c, which would call for strong magnetic fields to avoid the SC transition to emerge [34]. This also means that if the doping we choose is higher than values which allow the existence of CDW, let's say $p \approx 0.19$ in YBCO or BSCCO, we can study CDF's BP *alone* even well below T_c without interference from the more intense NP. This is exactly what was done to collect the data which is analyzed in this thesis, justifying the doping choice for our samples.

The complexity of charge order-related phenomena is evident, and reinforced by studies which draw attention to the fact that many different kinds of order, such as superconductivity, pseudogap, CDW and antiferromagnetism, occur on comparable temperature scales, and this could be non-accidental highlighting that they could be strongly intertwined [31].

As mentioned, the nature of CDF is yet far to be fully understood, but their extensive presence for different T and q ranges, together with their large width in momentum space, suggests them as quite an effective scattering mechanisms for other quasi-particles, thus possibly justifying some of the peculiar behaviors of cuprates such as the linear temperature dependence of the resistivity in the strange-metal state [1] [26] [34] .

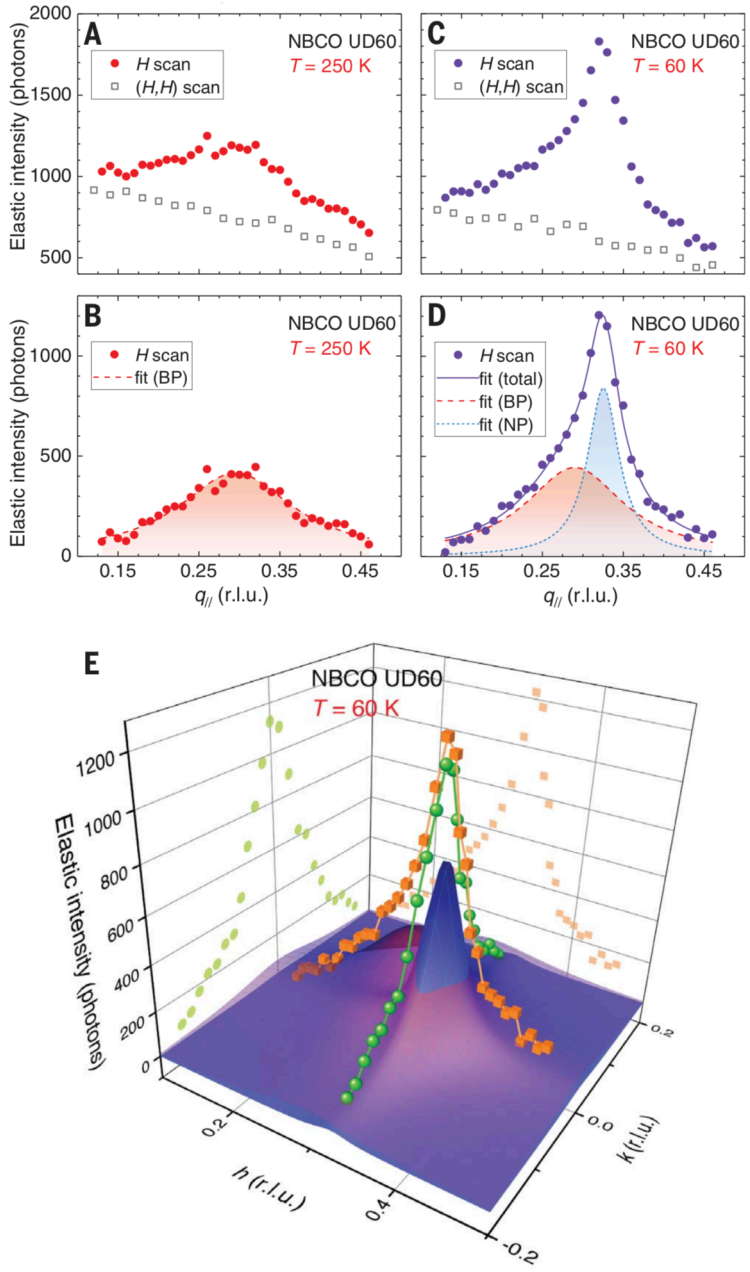

Figure 1.12: Two distinct peaks in fits to NBCO data. **(A)** Quasi-elastic scan measured along (H,0) on NBCO at T = 250 K (red circles). **(B)** After subtracting the linear background, given by the quasi-elastic scan measured along the Brillouin zone diagonal [open squares in (A)], a clear peak is still present, which can be fitted by a Lorentzian profile (dashed line). **(C)** Same as (A), but at T = 60 K (violet circles). **(D)** After subtracting the linear background [open squares in (C)], the data can be fitted with a sum of two Lorentzian profiles (solid line): one broader (dashed line), similar to that measured at 250 K, and the second one narrower and more intense (dotted line). **(E)** The 3D sketch shows the quasi-elastic scans measured along H (cubes) and along K (spheres) at T = 60 K, together with the Lorentzian profiles used to fit them. A narrow peak (NP, blue surface) emerges at q_{NP} = (0.325,0) from a much broader peak (BP, red surface) centered at q_{BP} = (0.295,0). Fig. from [1]

2 Resonant Inelastic X-ray Scattering (RIXS)

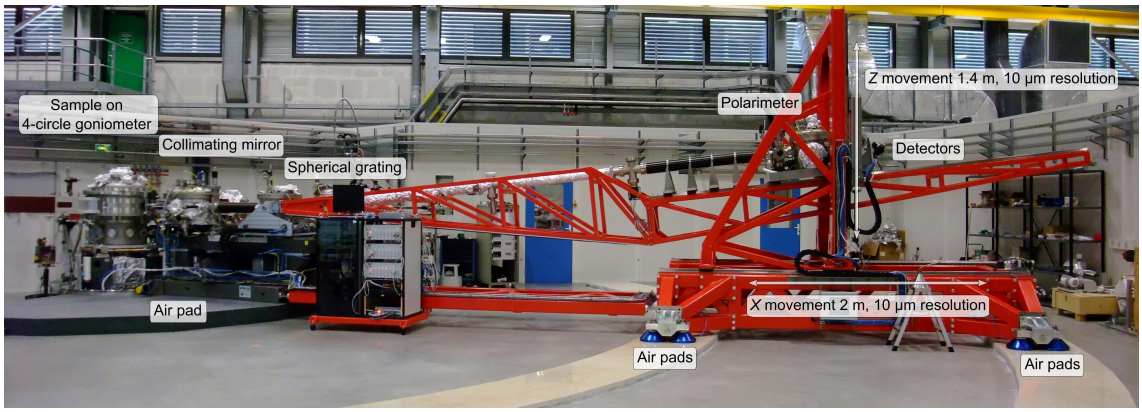

Figure 2.1: ID32 RIXS beamline at ESRF. Figure from [35].

2.1 The motivation

The investigation of the properties of highly correlated systems, the so-called quantum materials, and in particular $3d$TM oxides, requires the choice of an adequate probe, able to interact with all the excitations that contribute in determining the physics which governs their behavior.

The most common probes used for research in experimental solid state physics are electrons, neutrons and photons.

Electrons beams are easy and cheap to produce and control (i.e. mainly accelerate and focus). They can be used for microscopy with techniques such as scanning electron microscopy (SEM), transmission electron microscopy (TEM), leading to astounding results, eventually even reaching single atom resolution. They can also be employed to perform diffraction experiments: low energy electron diffraction (LEED) and reflection high energy electron diffraction (RHEED) are powerful tools for the characterization of surfaces' reciprocal lattice geometry (and therefore also their real lattice geometries through Fourier transformation). Electron energy loss spectroscopy (EELS) is also used to identify the ionization energy of given atoms'

shells in chemical compounds and to point out the energy of phenomena such as plasmons. The issue with the use of electrons beams, is that they can only penetrate few atomic layers because of their strong interaction with matter, thus resulting in an extremely surface sensitive probe, which overlooks completely bulk properties.

Neutrons, on the other hand, are remarkably weakly interacting with matter thanks to their neutral charge. Consequently, they are quite bulk sensitive and this makes them ideal for diffraction experiments, and maybe even more for the investigation of matter's magnetic properties. This is due to their spin (1/2) which interacts with atomic moments in the sample and allows us to measure magnetic dispersion relations with extremely high resolution. Up until a decade ago, neutrons were the only probe suitable for this purpose. Nevertheless, the downside of neutrons is that, lacking charge, they are much harder (and therefore more expensive) to generate, accelerate and focus on samples, often resulting in poor count rates and large spot sizes. Additionally, being so weakly interacting with matter they require thick samples, so their use for the study of thin films is completely unfeasible.

Photons in the visible range are good for microscopy, but they are far from reaching atomic resolution despite the recent progress in near field microscopy (NFM), which aims at reducing the resolution by confining the source down to the nanometric scale, thus reconstructing the evanescent components in the object's spectrum. The use of photons in the visible range to perform spectroscopy sets a rather low limit on the maximum energy that can be transferred to the system, and therefore to the electronic transition that can be induced.

Finally, X-ray photons are great probes for a broad range of applications such as diffraction (XRD) and spectroscopies (XAS, RIXS). Having penetration depths ranging from tens of nanometers to few microns, they are perfectly bulk sensitive, and their energy (e.g. $\sim$ 1000 eV for soft X-ray) allows the excitation of core levels of atoms within crystal structures thus suggesting their compatibility with the study of $3d$TM oxides (e.g. L_3 absorption edge of Cu $\sim$ 931 eV).

Over the last decades, the development of brilliant and powerful synchrotron sources has opened the gates to X-ray energy loss spectroscopy. Synchrotrons guarantee high photon fluxes: the intensity on the sample can be around $\sim 10^{11} - 10^{12}$ $\frac{photons}{s}$, allowing much better count rates with respect to other experimental techniques (such as neutron scattering). One fundamental advantage which comes with the use of X-rays is that high-energy photons carry much more significant momentum with respect to visible ones (see Fig. 2.2), and thus momentum conservation between

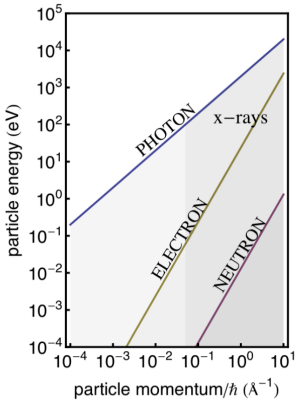

Figure 2.2: (Kinetic) energy and momentum carried by the different elementary particles that are often used for inelastic scattering experiments. Fig. from [18]

incident and scattered photons will make experiments sensitive to collective excitations in solids whose energy depends on momentum. X-rays are also sensitive to orbital symmetry and can couple to the spin degree of freedom thanks to the spin orbit splitting of electronic levels in matter, which can reach tens of eV in $2p$ levels of $3d$TM oxides.

Resonant Inelastic soft X-ray Scattering (RIXS) is an ideal spectroscopy to study $3d$TM oxides because, quite uniquely, it can get access to elementary excitations related to all degrees of freedom: charge, orbital, spin and lattice. It is an energy loss spectroscopy which uses X-rays tuned to match the binding energy of a core level, or more precisely the absorption edge of an atomic species in the sample [18]. During a RIXS experiment therefore, as it occurs in general for all spectroscopies, scattered photons have to obey energy conservation: $\hbar\Omega = \hbar\omega - \hbar\omega'$ where ω is the incident photon's frequency, ω' is the scattered one, and $\hbar\Omega$ is the energy loss; and, as mentioned, they also have to obey momentum conservation. This means $\mathbf{q} = \mathbf{k'} - \mathbf{k}$, where the momentum transfer $\mathbf{q}$ is a significant vector of the crystal's reciprocal space if the sample is a single crystal (to a significant extent) and can be taken (or given) by a variety of particles, quasi-particles and excitations, such as magnons, phonons, CDW and so on. The first resonant scattering measurements on cuprates in the soft X-ray regime were performed in 2002 by Abbamonte *et al.* [36].

If performed off-resonance, it can be used to measure processes which entail large energy losses (in the eV to hundreds of eV range), for example to study plasmons and core level excitations (X-ray Raman Spectroscopy); or, conversely, for few meV

energy-loss values, when vibrational and lattice excitations are probed (High Resolution Inelastic X-ray Scattering [37]).

2.2 The RIXS mechanism

In the resonant process (RIXS), on the other hand, incoming photons match an absorption edge of the 3*d*TM under scrutiny, therefore guaranteeing a large absorption cross section. They trigger the promotion of a core electron into a bound state just above the Fermi level; subsequently, the core hole left "below" is filled back by either the same or a different electron, with the emission of another photon. If it is the same electron going back to its ground state, we have -strictly speaking- an elastic scattering event, which probes the static component of the charge and magnetization density occurring in the system under study. Conversely, if an electron with a different energy fills the core hole, we talk about inelastic scattering, which is sensitive to dynamical processes and low-energy excitations. However, due to the finite energy resolution ΔE of the spectrometer, perfectly elastic scattering cannot be accessed, and it is more appropriate to use the term quasi-elastic, referring to a regime which is static up to a timescale $\tau \sim \hbar/\Delta$E [12]. That being so, in both cases this process involves three states: initial, intermediate and final (differently from non-resonant techniques such as XRD which lack an intermediate state). Only initial and final states can be observed with the measurement, so we will have a combination of all the possible processes that share the same initial and final states. A complete theory of RIXS, detailed for different classes of materials, can be developed quantitatively (e.g. in Ref. [18]), but it is beyond the scope of this work. Nevertheless, it is remarkable that the lack of a core hole in the initial and final states prevents it from taking part in additional lifetime broadening which would be detrimental for the spectral resolution, as it occurs in other processes such as XAS [38].

RIXS in 3*d*TM-based systems is usually performed at $L_{2,3}$ edges of transition metal oxides, which is ideal being 3*d* orbitals those that govern the magnetic and electronic properties of these materials. This means that upon absorption of the incoming photon, a 2*p* electron is promoted to an empty state of the 3*d* shell just above the Fermi level (see figure 2.3). This transition is allowed for electric dipole radiative transitions, resulting in a large cross section and reassessing the power of resonant scattering methods as opposed to conventional diffraction techniques, which, being

non-resonant, are largely insensitive to subtle electronic ordering phenomena not involving lattice degrees of freedom (such as CDW and CDF) [12]. Nevertheless, we must keep in mind that inelastic scattering is a second order process, so its cross section, even at resonance, is intrinsically small, thus making RIXS much more *photon hungry* with respect to its elastic counterpart REXS. The intermediate state is highly excited, being the energy difference between the levels involved comprised between 450 eV and 950 eV going from Ti to Cu. Its spin state is mixed because of the large spin-orbit interaction in the $2p$ level, which splits into the $2p_{1/2}$ and $2p_{3/2}$ levels, falling 7 eV to 20 eV apart. This intermediate state also happens to be very short lived: few *fs*, due to other non-radiative processes such as Auger decay, which we choose to neglect, but still play an essential role in setting the lifetime of this state [18]. Then, in *direct* RIXS, before the solid has time to readjust its magnetic and lattice structure according to the excitation, some $3d$ electron will fill the $2p$ core hole, with the consequential emission of an X-ray photon of a similar yet slightly different energy (where $\hbar\Omega$ is the energy loss introduced earlier). Contrarily, *indirect* RIXS occurs when the crystal does have time to change some of its properties according to the intermediate excited state. This occurs for example when the presence of the newly promoted electron in the $3d$ orbital induces a deformation in the lattice structure due to Coulombian attraction/repulsion with neighboring sites, triggering the excitation of a phonon. Similarly, the excited electron adds a spin vector 1/2 to the $3d$ shell, and this perturbation can set off one or more magnons (e.g. bi-magnon). As it occurs, magnons and phonons appear in RIXS spectra as indirect transitions.

The combination of the fact that the $3d$ shell is directly involved in the optical transition, and the strong spin orbit splitting of p levels conjure in allowing a broad range of possible excitations, as at this point has been brought up quite a few times, such as the charge transfer between anions and $3d$TM ions, electron-hole pairs formation, phonons, CDW, spin excitations and so on. Clearly, the photon energy is bound to the $2p$ - $3d$ energy difference, so to $\hbar\omega \leq 1$ KeV, which falls in the soft X-ray range. For the same reason also the maximum momentum transfer is bound to the X-ray photons' wave vector $k \leq 0.5$ Å^{-1}, which allows us to span most of the Brillouin zone size of typical $3d$TM-based systems.

So RIXS is evidently a very powerful instrument to perform momentum-resolved measurements of the properties of quantum materials, eventually reaching extremely high spectral resolution. In these terms, from a practical standpoint, the key for successful RIXS lies in the quality of the instrumentation [39].

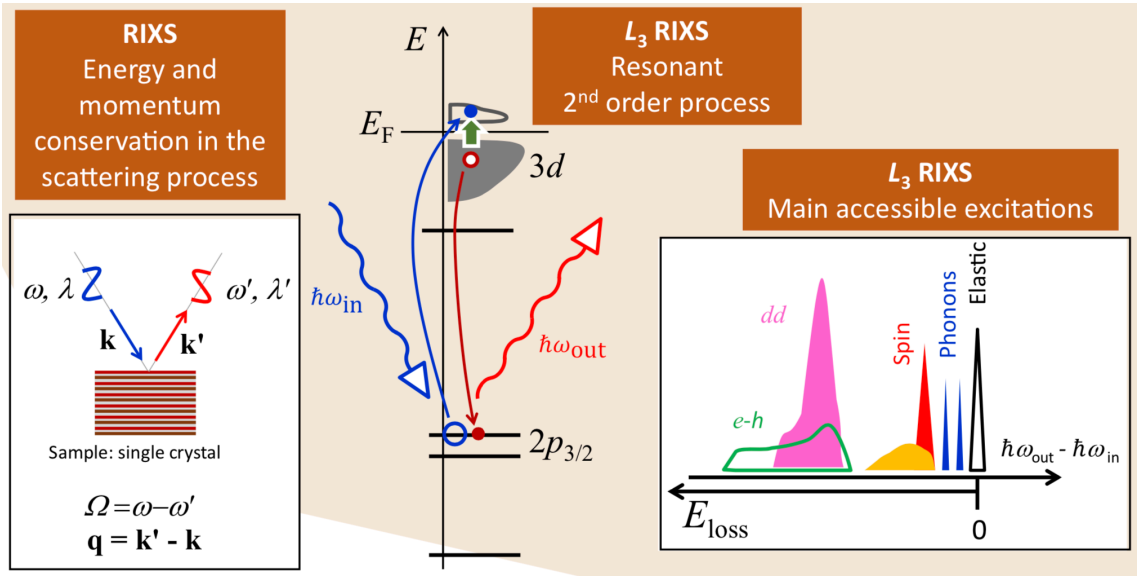

Figure 2.3: The RIXS process. The scattering process is illustrated for the case of $2p$ core state (L_3 absorption edge) of a $3d$ transition metal element: the final result can be seen as an electron-hole (e-h) pair excitation. Actually several classes of excitations (final states) are possible: e-h and charge transfer, dd (ligand field), spin (magnons, paramagnons, mutimagnons), lattice (phonons) excitations are all present in a RIXS spectrum at different energy ranges. Fig. from [20]

2.3 The RIXS instrumentation

The characteristics and quality of the instrumentation used to perform RIXS experiments ultimately settles the resolution of the measurement. Over the last years, efforts in developing better setups have lead to a decisive improvement of the resolving power, as can be observed in Fig. 2.5. Current RIXS systems can reliably go below 50 meV with photons around 1 KeV (resonance with the L_3 absorption edge of Cu $\sim$ 930 eV). Additionally, as mentioned, RIXS is a second order process and is thus very photon-hungry. The combination of these requirements (i.e. X-ray energies and large photon fluxes) leads to the necessity for synchrotron radiation, which is the first thing to be considered when designing a RIXS facility.

Incident beams are hence generated at dedicated beam lines by long (4 – 6 m) undulators of 3^{rd} generation synchrotron radiation storage rings. Undulators can provide fully polarized radiation with linear (σ or π with respect to the horizontal scattering plane) or circular polarization. Then, soft X-ray monochromators (incident beam) and spectrometers (scattered photons) are realized with the use of diffraction gratings mounted on high-quality X-ray mirrors and used at very grazing incidence (1.5°

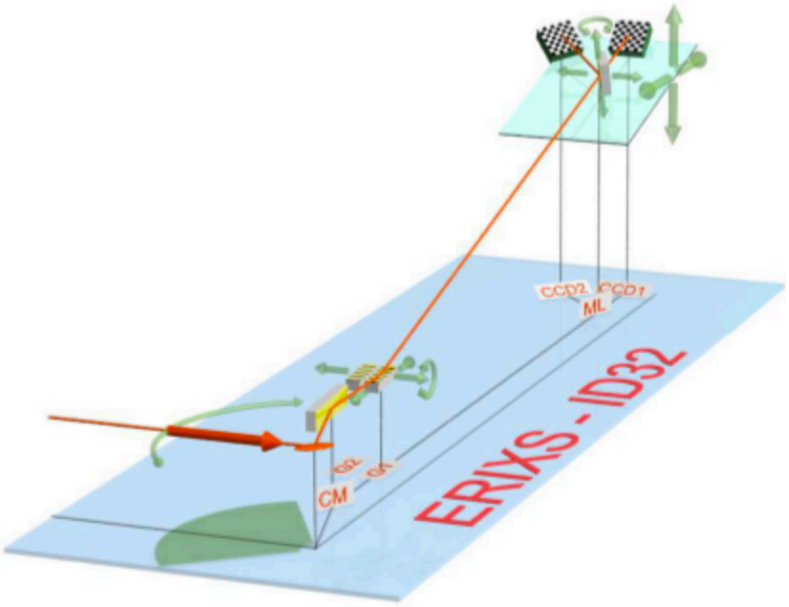

Figure 2.4: RIXS setup. Schematic representation of the experimental setup of ERIXS (beamline ID32). Figure from [40].

to 2.2° from the surface, see Fig. 2.4) [18]. The monochromator has the function of cutting the bandwidth down to 2 - 8 · 10^5 of the photon energy and then optical elements are used to focus it onto the sample surface to few micrometers in height and some tens of micrometers horizontally [20].

In the simplest cases, a single optical element: a grating with spherical shape (radius of curvature $\sim$ 100 m), disperses the scattered photons, and then a 2D Si CCD detector (cooled to reduce thermal noise) collects the intensity over a few eV energy of range, in parallel. Then, translating the detector coordinate into energy, the spectrum is then easily obtained [20].

As one can imagine, arm lengths are crucial in the determination of the final resolving power: longer instruments can reach higher resolution. For example, in order to reach sub-40 meV the ERIXS facility (ID32 beamline at ESRF) was built with an 11 m-long arm [35] as can be seen in Fig. 2.5. For this reason RIXS apparatuses are becoming extremely large, complex and expensive, so that dedicated buildings outside the main experimental facilities are manufactured [20]. The structure in Fig. 2.1 can provide a continuous rotation of the spectrometer from 50° to 150° with respect to the incident beam, and adjust the orientation and alignment of the sample with a high-quality 6 axis diffractometer, both without breaking ultra-high-vacuum operation conditions ($\sim 10^{-9}$ mbar) [41]. ERIXS has set a new standard and is being followed by equally or even more ambitious projects at other storage

rings (Diamond Light Source, NSLS in Brookhaven, MAX IV, TPS, Sirius) [20]. We can therefore expect exciting scientific findings coming forth in the next decades.

A)

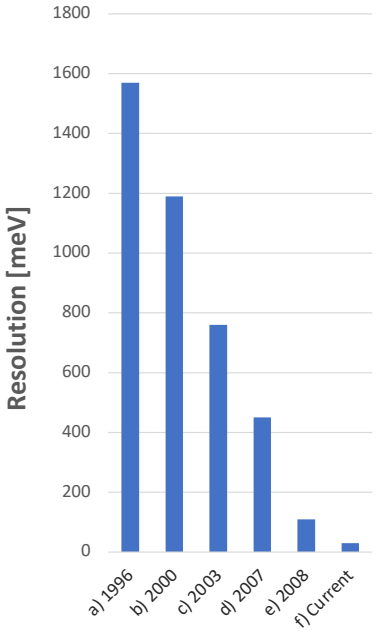

B)

	through-put w.r.t. high-resolution setup	combined energy resolution at Cu L_3 edge*
low resolution, high through-put	x12	42 meV
medium resolution, medium through-put	x4	32 meV
high resolution, low through-put	x1	28 meV 25 meV**

Figure 2.5: RIXS resolution. A) Progress in soft X-ray RIXS resolution at the Cu L_3 edge at 931 eV; (a) (Ichikawa et al., 1996), BLBB @ Photon Factory; (b) I511 - 3 @ MAX II (Duda et al., 2000b); (c) AXES @ ID08, ESRF(Ghiringhelli et al., 2004); (d) AXES @ ID08, ESRF(Braicovich et al., 2009); (e) SAXES @ SLS (Ghiringhelli et al., 2010); (f) Current @ ID32, ESRF. Figure readapted from [18].
B) Current RIXS throughput and resolution @ ID32 ESRF. Figure readapted from [35].

2.4 Data acquisition

Data produced by the CCD photodetector during a RIXS experiment is, for a fixed point of reciprocal space, a two dimensional map where on one axis we see the different spectral components of the scattered signal, separated in space by the diffraction element in the optics, which are collected in parallel on a few hundred points spanning an interval of a few eV, and along the other axis we have isofrequancy lines, as can be observed in figure 2.6. Such an image is taken in a few to several tens of seconds, and up to hundreds of such maps have to be acquired to gain a significant statics. We will then sum along the iso-energetic direction to add extra signal and reject more noise [42].

This is how we end up with the precursor of a spectrum, a plot displaying *scattered*

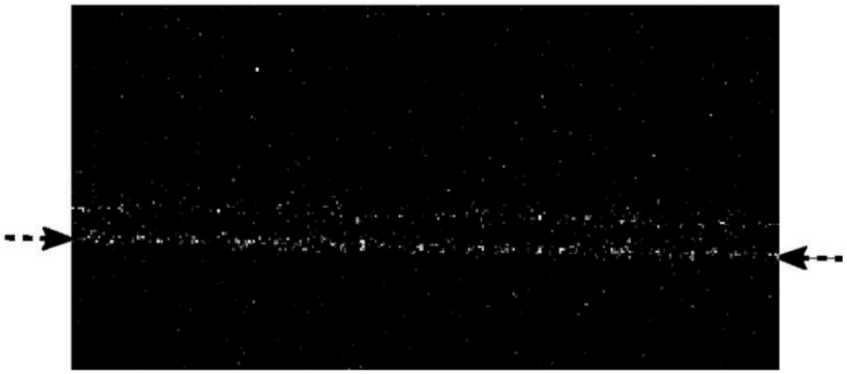

Figure 2.6: RIXS raw data. Typical image produced by the CCD detector during a RIXS experiment. Along the vertical direction we see the energy-related spatial coordinate, where photons have been diffracted by the grating. At the same time, photons with the same energy will hit the detector along iso-energetic lines perpendicular to the diffraction plane. This is shown in the horizontal direction as a degenerate spatial dimension over which we sum to obtain a spectrum. The two arrows indicate the presence of the zero energy-loss peak, i.e. the elastic peak. Figure from [42].

photons vs pixels. The correspondence meV-per-pixel can be determined by using an elastic scatterer and looking at the shift of the elastic line in pixels when varying the incoming photon energy [42]. This procedure yields a "regular" spectrum, i.e. an I(ω) curve, then the sample is tilted in order to act on the projection $\mathbf{q}_{\parallel}$ of the vector $\mathbf{q}$, where $\mathbf{q} = \mathbf{k}' - \mathbf{k}$ is the difference between the scattered and the impinging photons' wave vectors. This allows us to probe different points of the crystal's reciprocal space in the parallel direction with respect to the CuO_2 planes, so along Cu-O bonds as indicated in Fig. 2.7. Using angles as defined in this figure we get: $|\mathbf{q}_{\parallel}| = 2|\mathbf{k}|\sin(\theta)\sin(\delta)$. This course of action can then be replicated in a similar way for many values of the sample's temperature, thus ending up with I(ω,T,$\mathbf{q}$): a function of energy, temperature and momentum, which retains a vast amount of information.

2.5 Accessible excitations

An important issue is understanding *which* excitations RIXS allows us to probe in a sample.

All RIXS spectra share the presence of a strong peak at zero energy loss; this elastic peak is therefore associated to elastically scattered X-ray photons: photons

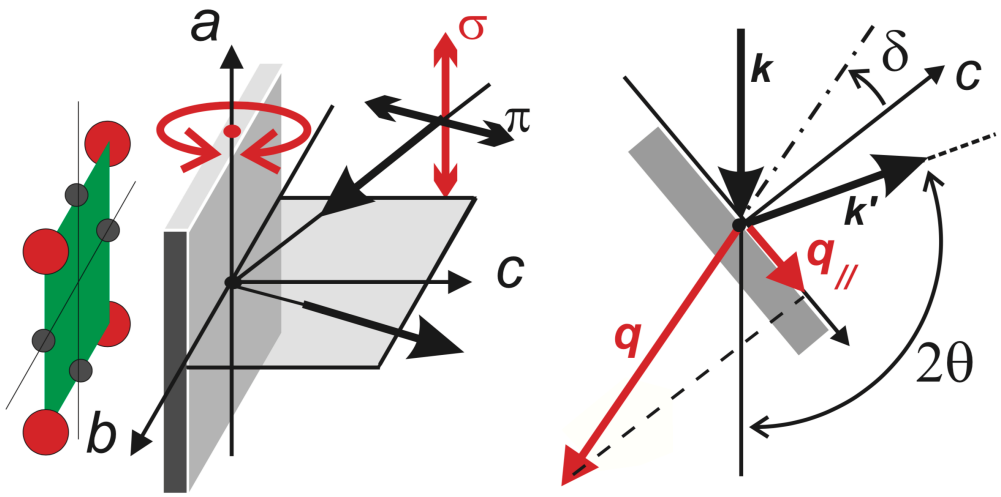

Figure 2.7: RIXS geometry. The incoming beam hits the sample surface, assumed to be parallel to the *ab* plane (Cu atoms in red and O atoms in grey). The scattering angle 2θ is fixed, while the incident angle and the azimuthal angle can be changed. They define δ, the angle between the sample *c*-axis and the transferred momentum $\mathbf{q}$ (red arrow). The projection of $\mathbf{q}$ onto the sample *ab*-plane, $\mathbf{q}_{\parallel}$, is also shown. During experiments δ is changed by rotating the sample around a vertical axis. Figure from [43]

re-emitted by the material with the same energy of the incident beam. This feature is so prominent that it often winds up obscuring other interesting phenomena which are characterized by a low energy loss, but smaller intensity. As one can imagine this ultimately translates in a matter of improving the resolution of the instrument.

Among all other processes that one can investigate through resonant inelastic X-ray scattering which appear in measured spectra, in the next sections I will point out two which are of major relevance, and mention a few more for completeness.

2.5.1 Magnetic Excitations

Magnetic excitations happen when incoming X-ray photons perturb the ground state of the magnetic order of the crystal. In a naive but intuitive single-ion model, we can think of a purely magnetic excitation as arising from an electron that, decaying from an (intermediate) excited state, returns to its original orbital, but with flipped spin. In an ordered spin lattice the reversal of a single spin at one site is not an eigenstate of the magnetic Hamiltonian, therefore this perturbation of the magnetic equilibrium can cause the excitation of a magnon a.k.a. of a spin wave: a linear

combination of local spin flip excitations with a site-to-site constant relative phase shift, which can be visualized as the precession around the ground state alignment direction as displayed in Fig. 2.8.

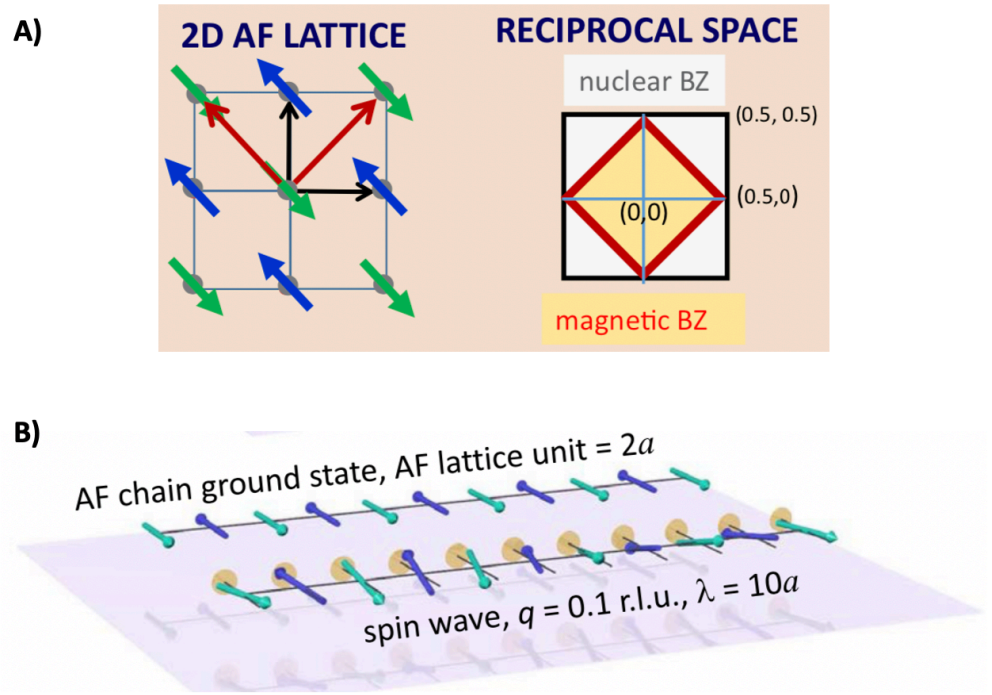

Figure 2.8: Magnetic Excitations. **A)** Representation of a 2D antiferromagnetic lattice and its Brillouin zone. **B)** Simple depiction of the excitation of a magnon in an AF-arranged system. Readapted from [20].

Magnetic excitations in cuprates are found in the proximity of 0.4 eV. It is notable that the periodicity of the spin lattice is double that of the crystal lattice, and thus the magnetic Brillouin zone will be half the size of the canonical one as displayed in Fig. 2.8 A) [19].

RIXS can therefore be used to determine the dispersion relation of magnons in antiferromagnetic (AF) cuprates (Fig. 2.9), whereas this was only possible with INS until a decade ago. Measuring spin-wave dispersion relations in cuprates is of great interest given that magnetic excitations in these materials are believed to play a central role in the generation of cooper pairs, similarly to what is done by phonons in conventional BCS superconductors [20].

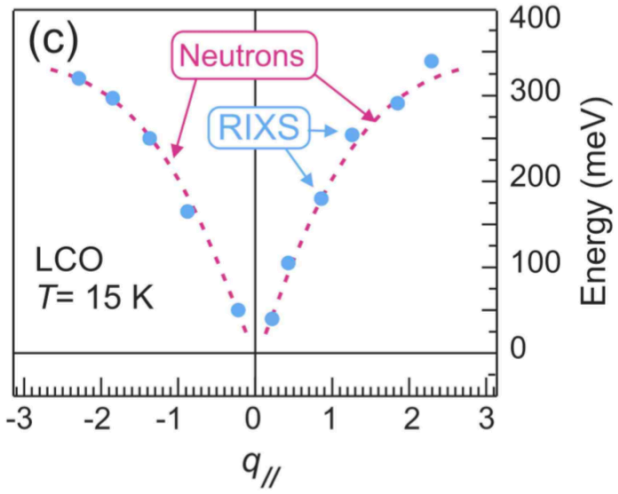

Figure 2.9: Magnonic dispersion relation. Comparing single magnon neutron data and RIXS measurements at the copper L_3 edge of La_2CuO_4; figure from [44].

2.5.2 Ligand field excitations

Ligand field excitations, or orbital excitations, take place when the RIXS process causes an electron's initial state's *orbital* to be different from its final one. In cuprates, where the resonant transition happens at the L_3 absorption edge, these are called *dd* excitations since they involve electrons belonging to *d* shells. As discussed in the first chapter, in cuprates, the lower symmetry of the potential felt by the $3d$ transition metal lifts degeneracy among *d* orbitals $x^2 - y^2, z^2, yz, xz, xy$. Therefore, the excitation spectrum of *dd* transitions becomes more varied and the energy of each peak can be directly associated to the parameters describing the ligand field that lowers the spherical symmetry in the first place [45], thus allowing us to measure the orbital symmetry of the $3d$ states, which is linked to the crystalline structure [46]. For example, in the simplest case, we have Cu^{2+} ions with a $3d^9$ configuration, therefore the (intermediate) $3d^{10}$ excited state is unique (as can be observed with XAS) and, if the $3d$ electron that decays into the $2p$ level (final state) belonged to a different-symmetry $3d$ orbital, then we have a *dd* excitation. When the cation ground state has multiple holes as it occurs for example in Ni^{2+} ($3d^8$) and Mn^{2+} ($3d^5$) the set of *dd* excitations is wider and spectra are richer and more complex, but still relatively straight forward to interpret in terms of the local symmetry of each specific material [20].

Figure 2.10 shows the RIXS spectrum of a series of cuprates, where charge transfer, magnetic and *dd* transitions are clearly visible and easy to tell apart.

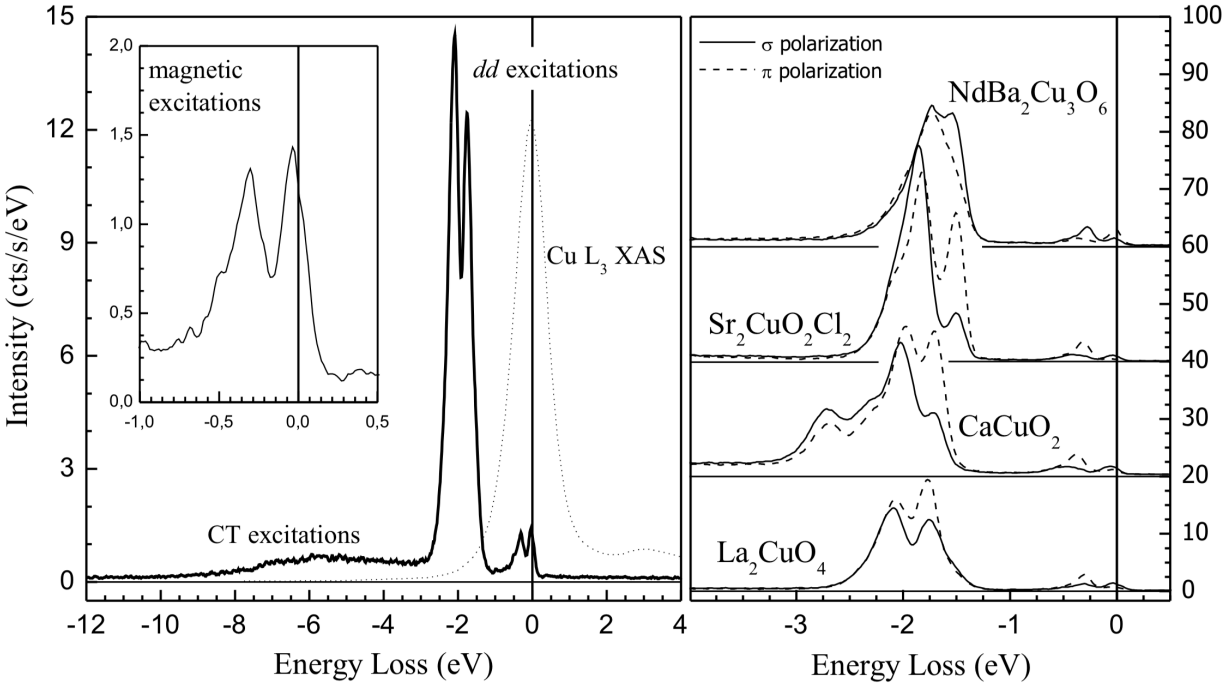

Figure 2.10: RIXS in various cuprates showing *dd* excitations spectra.
Left. Example of Cu L_3 absorption (dashed) and RIXS (solid) spectra of La_2CuO_4 (LCO) with σ polarization. One can recognize charge transfer (CT), *dd* and magnetic excitations at different energies. A closer look of the mid-infrared energy region is given in the inset. **Right.** RIXS spectra for LCO, SCOC, CCO and NdBCO in the same experimental geometry as left panel for σ and π polarization, displaying how *dd* spectra constitute a signature for each material. Figure from [43]

Beyond these noteworthy two, there are many more excitations accessible through a RIXS measurement. Among them we find *phonons* (two publications on phonons which our group recently worked on can be found in Ref.s [47] [48]) , *charge transfer excitations, bimagnons, orbitons, ff transitions, charge order excitations* (for an overview on charge order see Chapter 1) and so on, as thoroughly explained in [18]. This makes RIXS an extremely versatile experimental technique for the investigation of the intertwined properties of quantum materials.

3 Data and model

As anticipated, the project at the core of this thesis arises as a follow-up and further development of the exciting and possibly revolutionary findings on charge density modulations in cuprates, discussed in recent publications such as [1], [2]. In particular, the hope is that the joint efforts of our research team and the group of theorists from La Sapienza University lead by Carlo Di Castro, will provide a significant breakthrough in the understanding of the physics behind charge order and its relation with high-T_c superconductors' exotic phases. More specifically, as introduced in Sect. 1.4, up to this day, scientific literature has broadly reported that charge modulations in cuprates manifest themselves with the presence of a quite narrow peak (in reciprocal space, NP), highly temperature-dependent and of static nature, having null energy loss (as shown in Fig. 3.4). Furthermore this charge order phenomenon has been reliably proven to compete with superconductivity ([31] [33] [29]). Interestingly, recent RIXS findings brought to light the existence of a broader peak (BP), which permeates a much wider portion of cuprates' phase diagrams, thus existing at much higher temperatures with respect to previously considered CDW, and for a larger interval of doping levels [1] [2] [34] [26]. This peak shows conspicuous signs of being related to a non-static charge order excitation which has been called charge density fluctuation (CDF). A CDF broad peak is observed in a wide range of different cuprates and might as well be central in triggering many of these material's peculiar properties.

Early theories, which take in the experimental evidence on these excitations and try to formulate models able to bring about results and predict further characteristics, are currently being formulated. In particular, the mentioned team of theoretical solid-state physicists lead by Carlo Di Castro has produced a mathematical expression for the narrow and broad peaks related to charge density modulations. This model relies on the knowledge of a series of physically relevant parameters to reconstruct the behavior of CDW/CDF as a function of energy and momentum (coordinates of reciprocal space of cuprates, as discussed in Chapt. 1).

The following work will concentrate on providing a computational analysis of this model, resorting to a reasonable set of a parameters to produce simulations. I will then move on with a proper fit of the data in Chapt. 4.

I will hereby present the experimental data and describe the model itself from a theoretical standpoint. Throughout all analyses the focus will be kept on attempting to reproduce as faithfully as possible the experimental evidence, which has been collected by Giacomo Ghiringhelli's group through state-of-the-art RIXS technology on various high quality cuprate samples.

3.1 Experimental data

Experimental data hereby described and utilized has been collected in the period between January 30^{th} and February 4^{th} at Diamond Light Source (UK) on slightly overdoped (i.e. p $\approx$ 0.19) YBCO and BSCCO samples, for more information on samples used, the reader can go back to Sect.s 1.3.1 and 1.3.2, while the RIXS process in general terms is described in Chapt. 2. In this specific case the L_3 absorption edge of Cu was chosen for the tuning of the incoming photon energy ($2p_{3/2}$ - $3d$ at $\approx$ 931 eV). In order to generate the data, spectra were acquired on 8 and 16 different points along respectively (H,H) and (H,0) directions in the reciprocal lattice of CuO_2 planes (for simplicity we will only refer to them as HH and H0). In our case spectra were acquired with a resolution of $\sim$ 60 meV which is approximately twice the best achievable, but it allows us to collect data faster, and therefore to fetch more of it. Additionally, few ultra-high resolution (HR) ($\sim$ 35 meV) spectra were acquired at the momentum value where the CDF intensity is maximum (namely Q_c), this gave us a first approximated estimation of the CDF energy. The result of this last measurement is shown in Fig. 3.9.

3.1.1 Self absorption correction

During the RIXS scattering process core-level excitations lead to the absorption of photons and therefore to the attenuation of the signal intensity, as outgoing photons propagate through the sample. This attenuation is called *self absorption* and strongly depends on the scattering geometry. Clearly, correcting spectra for this extrinsic effect is fundamental in order to make them comparable with each other when acquired at different angles [18]. For example, if the chosen geometry relies on a small scattering angle with respect to the parallel to the sample, and a big (ideally 90°) incidence angle (i.e. a normal-in grazing-out geometry), this effect is maximum because outgoing photons have to travel a longer path within the sample

before being emitted. Vice versa, given a grazing-in normal-out geometry, this effect is minimized. Self absorption is certainly an issue in our case, considering that our intensity signals map reciprocal space in 16 and 8 different points along H0 and HH directions.

Additionally, we have to consider that incoming photons are tuned purposefully to match the central frequency of an absorption line of the material, let's say $\omega_{central}$. Hence, the elastically scattered photons will see a much larger absorption cross section σ_{abs} with respect to those scattered at a lower or higher frequency with respect to the central one, i.e. $\omega = \omega_{central} \pm \Delta\omega$ (see Fig. 3.1), this is the case for any non-elastic scattering process such as, for example, ligand field excitations [49]. This means that we also have to use a different self absorption correction for different spectral regions, which can be done with the aid of XAS spectra providing the necessary information regarding absorption cross sections as a function of photon energy.

Moreover, due to the anisotropy of cuprates (i.e. their quasi-bi-dimensional nature), their absorption is also polarization sensitive. In particular, it is much stronger for in-plane polarized scattered photons ((a,b) plane) with respect to those polarized along the so-called c direction: perpendicular to CuO_2 planes. Certain phenomena can indeed rotate the polarization of photons upon scattering, among them we find all those involving single spin-flips.

To sum up, self absorption coefficients C must be calculated for each point of reciprocal space, taking into account geometry, energy and polarization; and then used to normalize spectra before proceeding to make analyses so that $I_{effective} = I_{measured}/C$ (Fig. 3.2 shows the polarization and momentum dependence of C). Quantitative calculations of self absorption corrections can be found in [49] and [51] where, notably, using the fluorescence signal of a known emission line (measured in the same scattering geometry), attenuations as high as 20%-25% were found.

3.1.2 *dd* normalization

Performing a RIXS experiment can take hours, this makes sense when we consider that we have to collect spectra over hundreds of points for each coordinate of reciprocal space, and then again for several temperature values. During this time the photon flux reaching the sample can undergo mild oscillations, implying slight changes in the intensity of the impinging beam. As a consequence, also the scattered (and detected) intensity will fluctuate.

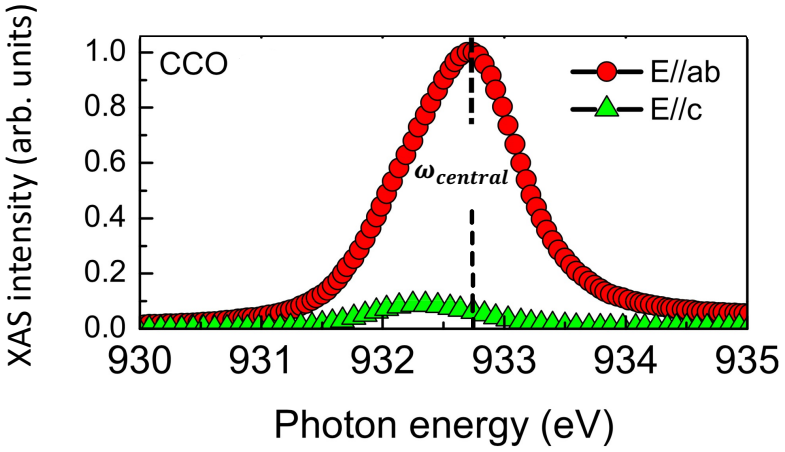

Figure 3.1: XAS spectrum at Cu L_3 edge in CCO.
Normalized XAS spectra taken at the Cu L_3-edge in a CCO film, spectra are recorded both with the electric field perpendicular (triangles) and parallel (circles) to the CuO_2 plane showing the polarization dependence of absorption. The central frequency $\omega_{central}$ associated to the highest absorption cross section is indicated by the dashed line, any other frequency around it will be absorbed less. Figure from [50]

Additionally, we want to be able to compare spectra acquired at different facilities, during different experimental sessions, on different samples (made of the same material clearly).

These issues call for a normalization standard to bring some degree of universality to RIXS measurements. A possible approach which is currently being widely used is that of normalizing spectra with respect to the area underlying the *dd* transition related bandwidth. This is reasonable in light of the fact that a predominant portion of the scattered intensity can indeed be traced back to ligand field excitations, and therefore constitutes a rather stable value to be used for a normalization procedure (see Fig. 3.3). The overall area below all *dd* transitions occurring during an experiment has been proven to be constant with respect to q, even if the intensity associated to each one single ligand field excitation changes [43].

3.1.3 Energy integration

In the following development of this work, I will choose to perform the fitting of the CDF peak using intensity-over-momentum signals, namely I($\mathbf{q}$) curves, and not full I($\mathbf{q}$,ω) maps, therefore discarding the information related to the energy dependence of the charge modulation features. The reasons behind this decision will be detailed

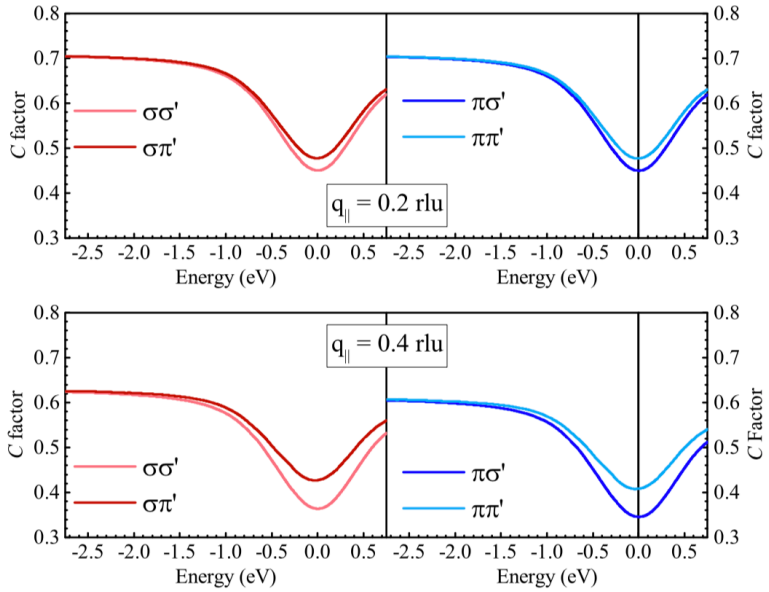

Figure 3.2: Self-absorption correction factors.
Self-absorption correction factors at $q_{||}$ = 0.2 r.l.u. (top panels) and at $q_{||}$ = 0.4 r.l.u. (bottom panels) for both σ and π polarization of the incident and scattered light calculated from the XAS spectra measured by total electron yield on an AF NBCO sample. Figure from [49].

in Chapter 4, but this is enough to say that our spectra will need to be integrated over a given energy range for each point in momentum space, so that:

$$\int_{\omega^{min}}^{\omega^{max}} I^{exp}(\mathbf{q},\omega)\, d\omega = I^{exp}(\mathbf{q})$$

Overall spectra are collected on a few eV range, whereas the CDF peak is found at close-to-elastic energies (namely $\omega_0 \approx 10$ meV with few meV FWHM). This means that it would be enough to integrate the measured intensity signal in $\sim$ (-25,+25) meV to capture the most relevant portion of the charge modulation peak. In Fig. 3.4 one can visualize a similar situation, with the difference of it being represented for static (hence nearly-elastic) CDW instead of CDF. Our HR measurement of a CDF spectrum is shown in Fig. 3.9. Nevertheless, the spectral region comprised between -100 meV and -25 meV is quite featureless, thus, keeping in mind that performing an integration increases noise rejection, we chose to extend the overall integration window to (-100,+35) meV. This allows us to produce I($\mathbf{q}$) curves which truly capture all of the CDF spectral intensity, while at the same time increasing significantly signal to noise ratio.

After all this processing, data can be imported as tables representing intensity values for each point in reciprocal space along the chosen direction for the measurement.

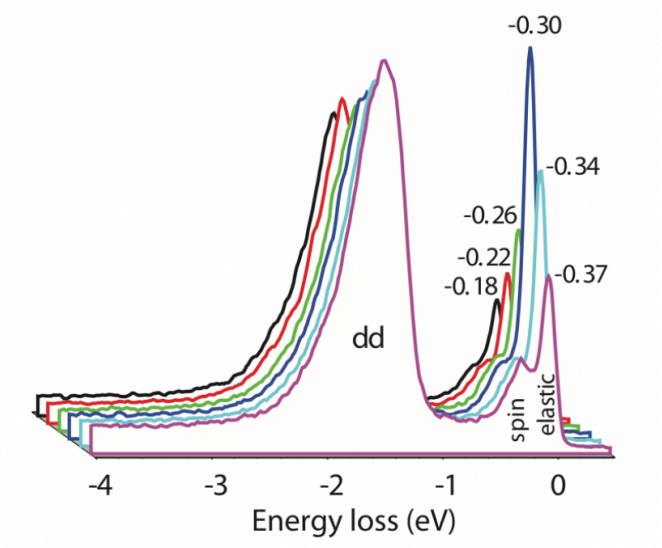

Figure 3.3: *dd* **excitations.**
RIXS spectrum of underdoped $Nd_{1.2}Ba_{1.8}Cu_3O_7$ as a function of momentum along H0, comparing the fairly dispersionless *dd* excitation peaks to the emergence of a quasi-elastic peak around H ~ -0.31 r.l.u. (which in this case is attributable to charge order). The area underlying *dd* excitations is evidently predominant. Figure from [12].

If the experiment is run for many temperature values, then data is presented in the form indicated in Fig. 3.5, which is the actual data collected on YBCO (and Bi2212 in Fig. 3.6) used for the fitting in this thesis. Then, such tables can be imported into a program such as MATLAB®, and plotted as a function of momentum, having a parametric dependence on temperature, as shown in Fig.s 3.7 and 3.8.

Clearly, Fig.s 3.7 and 3.8 reinforce the fact that the existence of the CDF peak at incommensurate wave vector $Q_c \sim 0.3$ r.l.u. is indisputable in both classes of cuprates. In fact, we can exclude any CDW contribution (NP) thanks to our doping choice p ~ 0.19, which is incompatible with the existence of intermediate-range static density-wave order excitations (as observed in Fig. 1.10) and, in the studied materials, corresponds to a putative QCP (at zero T) [26] [32]. Also, we notice that the absolute value of the RIXS measured intensity increases with temperature, even though this is observed almost solely for the three highest T-values and is a quite weak effect all along (on both samples). Similarly, the curves FWHM is not heavily affected by T, being slightly larger at higher temperatures, but again, this is a mild effect occurring only for the three-four upmost curves. Additionally, we see a sharp rise in data for approximately q ≤ 0.17 r.l.u. for YBCO and q ≤ 0.15 r.l.u. for Bi2212, which has nontrivial explanation and will be further discussed in Chapt. 4. Peaks become less sharp with the increase in T, meaning that the curves' sweep

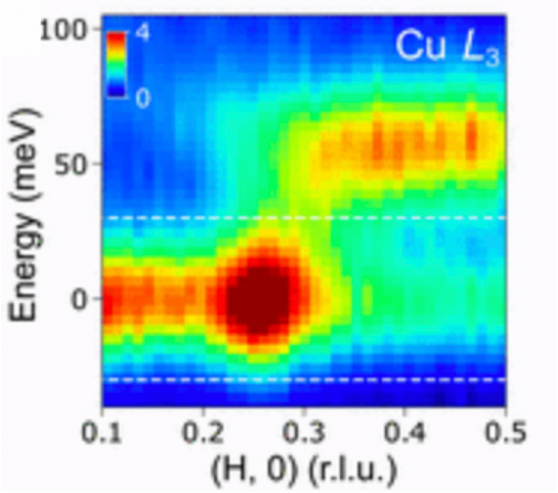

Figure 3.4: CDW spectrum.
CDW spectrum as a function of H0 in $Bi_2Sr_2LaCuO_{6+\delta}$, white dashed lines delineate the (-30,+30) meV range. Figure from [52].

between their maximum and minimum becomes quantitatively smaller, this could suggest the presence of a variable background which, again, is not straightforward to justify and/or model, and of a relevant T-dependence of CDF. This brief overview allows us to take a first interpretative look at measurements, but will be further developed in the following work, along with the results of the model analysis.

3.2 The model

The equation that will be implemented for the simulation of the broad peak (BP) associated to charge density modulations, and in particular of CDF, was developed in the assumption that RIXS experiments can directly access the charge susceptibility $\chi(\mathbf{q},\omega)$. In this context, the BP contribution to RIXS spectra is proportional to the absorptive part of the (retarded) dynamical density fluctuation propagator [34]. This approach should actually describe both CDW and CDF, but we're now mostly interested in the fluctuating modulations, which are the newly discovered phenomenon at the core of our study. In light of these considerations, the CDF contribution to the low-energy RIXS spectrum is (all following expressions are taken from [34]):

A)

	20	35	50	65	80	95	110	140	170	200	230	260	290
0,15	0,040834	0,043491	0,043281	0,043095	0,043634	0,045311	0,049363	0,056477	0,052342	0,055046	0,059201	0,059879	0,06769
0,17	0,036038	0,039128	0,038224	0,0394	0,040558	0,043087	0,04567	0,053619	0,050312	0,051786	0,053373	0,05635	0,060292
0,19	0,037217	0,039204	0,038352	0,040025	0,040729	0,042679	0,045429	0,051318	0,047795	0,050625	0,051094	0,054875	0,060571
0,21	0,038547	0,040022	0,039146	0,041282	0,040721	0,043425	0,045457	0,050137	0,050257	0,051146	0,053616	0,055214	0,058732
0,23	0,041994	0,043586	0,042358	0,044845	0,04367	0,046009	0,049826	0,050021	0,051664	0,05497	0,056091	0,056721	0,059985
0,25	0,050395	0,051349	0,051371	0,052362	0,052069	0,052367	0,055318	0,055972	0,056151	0,058904	0,061246	0,062113	0,066546
0,27	0,05712	0,059024	0,056485	0,058468	0,057564	0,057097	0,05942	0,059714	0,059779	0,061824	0,066238	0,065384	0,068082
0,29	0,064861	0,064785	0,06454	0,066177	0,064438	0,064355	0,066267	0,064776	0,066411	0,067585	0,06914	0,06977	0,073383
0,31	0,063384	0,064243	0,064574	0,066524	0,062812	0,063642	0,064236	0,063187	0,065943	0,065787	0,070685	0,070691	0,072972
0,33	0,05917	0,059841	0,057898	0,060164	0,057607	0,058402	0,060878	0,059958	0,062286	0,061285	0,06729	0,06664	0,067969
0,35	0,052808	0,053774	0,053294	0,054447	0,053428	0,054177	0,057676	0,056314	0,057794	0,060775	0,063866	0,067147	0,070206
0,37	0,048752	0,048505	0,048625	0,049541	0,04713	0,048053	0,050621	0,050485	0,053505	0,054843	0,060064	0,061033	0,061592
0,39	0,045364	0,045431	0,044931	0,045675	0,043339	0,045906	0,047026	0,049174	0,051649	0,052024	0,056646	0,0565	0,060366
0,41	0,043147	0,046092	0,04317	0,044492	0,041934	0,045933	0,047118	0,049092	0,050777	0,052189	0,057564	0,057556	0,062207
0,43	0,039877	0,040581	0,039592	0,040974	0,039196	0,040402	0,043079	0,04473	0,048572	0,049528	0,055459	0,056228	0,059071
0,45	0,037566	0,038561	0,039065	0,040413	0,039783	0,040118	0,04338	0,043996	0,044772	0,048712	0,051438	0,054278	0,056945

B)

	20	35	50	65	80	95	110	140	170	200	230	260	290
0,141421	0,033987	0,034251	0,034824	0,037602	0,038561	0,040695	0,050604	0,042448	0,043304	0,047577	0,051341	0,052291	0,054308
0,183848	0,030338	0,029383	0,030396	0,031393	0,032896	0,034771	0,039542	0,037823	0,040252	0,040641	0,046326	0,047808	0,050399
0,226274	0,028818	0,02937	0,029744	0,03155	0,032893	0,033013	0,036711	0,034147	0,038084	0,039916	0,043607	0,043951	0,045752
0,268701	0,030496	0,029635	0,029491	0,031419	0,031243	0,032411	0,036836	0,034917	0,039236	0,039853	0,042439	0,043977	0,046426
0,311127	0,030154	0,029223	0,029087	0,031697	0,031553	0,033417	0,035423	0,033867	0,036419	0,037531	0,042688	0,044161	0,046146
0,353553	0,029096	0,028503	0,027329	0,029948	0,031005	0,031188	0,034396	0,032928	0,035483	0,037714	0,040717	0,042622	0,043876
0,39598	0,028986	0,027537	0,02884	0,030482	0,030016	0,030264	0,03267	0,031542	0,034378	0,036384	0,039846	0,041471	0,044701
0,438406	0,028806	0,028161	0,027934	0,029361	0,029398	0,030662	0,032663	0,032115	0,034706	0,037074	0,041731	0,042306	0,045217

Figure 3.5: Data tables YBCO.

A) Data as a function of temperature [K] along H0; 16 points in 0.15 - 0.45 r.l.u.

B) Data as a function of temperature [K] along HH; 8 points in 0.14 - 0.44 r.l.u.

$$I^{sim}(\mathbf{q},\omega) = I^{sim}(q_x, q_y, \omega) = A \cdot b(\omega) \cdot \mathbb{I}mD(q_x, q_y, \omega) \tag{3.1}$$

where

$$b(\omega) = \frac{1}{e^{\omega/k_B \cdot T} - 1}$$

is the Bose distribution, governing the thermal excitation of CDF. A is a constant regulating the intricate interaction between incoming photons and conduction electrons involved in scattering events. D($\mathbf{q}$,ω) is taken in the standard Ginzburg-Landau form of the dynamical density fluctuation propagator, typical of overdamped quantum critical Gaussian fluctuations [26] [34] :

$$D(\mathbf{q},\omega) = \sum_{n=1}^{4} [\omega_0 + \nu \cdot \eta_n(\mathbf{q}) - i\omega \cdot \gamma - \frac{\omega^2}{\Omega}]^{-1}$$

where $\omega_0 = \frac{\nu}{\xi^2}$ [eV] is the characteristic energy of the fluctuations, and ξ is the correlation length of the excitation. Notably, in this model, ω_0 is bound to the FWHM of intensity profiles through the correlation length, giving $\omega_0 = \nu \cdot (\text{HWHM})^2$ [26]. In light of the quasi-saturation of FWHM shown by experimental data represented in Fig.s 3.8 and 3.7, we are lead to believe that ω_0 might have slightly growing character

A)

	20	35	50	65	80	95	110	140	170	200	230	260
0,08	0,033414	0,032889	0,033893	0,035131	0,037087	0,037347	0,037668	0,040615	0,038122	0,04286	0,045326	0,046176
0,1	0,029719	0,028593	0,02922	0,030661	0,031943	0,030694	0,032617	0,03563	0,035346	0,038251	0,039325	0,040487
0,12	0,027378	0,027376	0,027761	0,027829	0,03191	0,03107	0,032486	0,032577	0,032863	0,035495	0,036891	0,038311
0,14	0,027469	0,026183	0,027211	0,028355	0,03136	0,028629	0,031982	0,032876	0,033843	0,036589	0,035961	0,038936
0,16	0,026266	0,025671	0,026162	0,027614	0,030588	0,028141	0,030799	0,032147	0,033878	0,034938	0,036282	0,037876
0,18	0,027554	0,024774	0,027103	0,027365	0,029436	0,028714	0,030684	0,031615	0,033614	0,034238	0,03492	0,037847
0,2	0,030062	0,029077	0,030677	0,030694	0,03237	0,031399	0,033069	0,033169	0,034989	0,037504	0,036573	0,03886
0,22	0,031801	0,032122	0,032	0,031801	0,033883	0,032273	0,034991	0,035492	0,036205	0,037722	0,038359	0,039566
0,24	0,036317	0,03636	0,035602	0,035412	0,036392	0,035787	0,037172	0,03705	0,037917	0,042079	0,042053	0,041611
0,26	0,037476	0,037398	0,037657	0,037272	0,037952	0,037221	0,036874	0,037309	0,038361	0,042276	0,041358	0,042502
0,28	0,035919	0,035758	0,035099	0,033456	0,034749	0,033904	0,035378	0,037285	0,036542	0,041255	0,041394	0,041932
0,3	0,032856	0,032012	0,032744	0,032713	0,032526	0,03236	0,034802	0,037493	0,03799	0,041901	0,040844	0,042329
0,32	0,033527	0,032714	0,032651	0,031699	0,033232	0,032146	0,034017	0,034746	0,03632	0,040638	0,041297	0,043282
0,34	0,030762	0,031076	0,030145	0,029045	0,030183	0,028676	0,030644	0,032319	0,031521	0,037397	0,036624	0,039498
0,36	0,028171	0,027957	0,02744	0,02656	0,027875	0,02739	0,028338	0,031367	0,03074	0,036783	0,036165	0,03736
0,38	0,029539	0,027917	0,028566	0,028226	0,029288	0,028871	0,028502	0,030931	0,033198	0,035507	0,036223	0,03757

B)

	20	35	50	65	80	95	110	140	170	200	230	260
0,084853	0,029662	0,030491	0,029949	0,031283	0,032019	0,028044	0,03068	0,034251	0,035187	0,037618	0,040758	0,042424
0,127279	0,025279	0,025085	0,025052	0,024831	0,02658	0,025751	0,027387	0,028586	0,030246	0,031997	0,034492	0,035776
0,169706	0,023878	0,024033	0,023492	0,023841	0,02671	0,025663	0,027956	0,029436	0,029108	0,03212	0,03349	0,035415
0,212132	0,023979	0,023921	0,022877	0,023174	0,025667	0,026294	0,027815	0,028031	0,027873	0,029805	0,03326	0,033383
0,254558	0,023867	0,023744	0,023655	0,023966	0,025232	0,025002	0,026096	0,027642	0,027388	0,029035	0,033121	0,033089
0,296985	0,021789	0,020754	0,021826	0,021406	0,022646	0,022711	0,022999	0,02446	0,024422	0,025135	0,029241	0,030345
0,339411	0,020249	0,019828	0,019779	0,019969	0,021438	0,021394	0,021726	0,021601	0,023693	0,025327	0,028016	0,028906
0,381838	0,02114	0,021515	0,021145	0,019081	0,02246	0,022039	0,023343	0,022981	0,02225	0,023845	0,028697	0,028668

Figure 3.6: Data tables Bi2212.

A) Data as a function of temperature [K] along H0; 16 points in 0.08 - 0.38 r.l.u.

B) Data as a function of temperature [K] along HH; 8 points in 0.085 - 0.38 r.l.u.

with respect to temperature, saturating below a certain threshold. Nevertheless, the relation $\omega_0 = \nu \cdot (\mathrm{HWHM})^2$ is only valid in the so-called "classical regime", defined by $\frac{\omega_0}{\gamma} \leq \mathrm{T}$, while at very low temperatures, in the "quantum regime" identified by $\frac{\omega_0}{\gamma} \geq \mathrm{T}$, the defining relation of FWHM yields a different condition which is not straightforward to derive. This means that this reasoning is not rigorous, and while it can be used to develop a general understanding of the connection between certain parameters and experimental data, it can not be straightforwardly used to extract $\omega_0(\mathrm{T})$ in the whole temperature range under scrutiny.

The value of ν regulates the width of the dispersion relations given that:

$$\eta_n(q_x, q_y) = \frac{1}{(2\pi)^2}(4 - 2\cos(q_x - Q_x^c) - 2\cos(q_y - Q_y^c))$$

is periodic in reciprocal space, thus producing peaks in all Brillouin zones at well defined coordinates given by incommensurate wave vectors ($\pm Q_c$,0), (0,$\pm Q_c$) defined in the (q_x,q_y) plane, which is the reciprocal lattice of the CuO_2 planes of cuprates. This periodicity is shown in Fig. 3.15.

Ω is a frequency cutoff and γ is a Landau-damping factor, only relevant at low tem-

peratures, influenced by the superconductive transition. γ is believed to model the time correlation of CDF and is expected to diverge in absence of superconductivity for T $\rightarrow$ 0, defining a putative anomalous QCP, being it linked to the divergence of a time-related correlation parameter, instead of a spatial one.

As described in Sect. 3.1.3, RIXS measurements are occasionally used solely as a function of momentum, i.e. the quasi-elastic energy integration of inelastic spectra in a given energy range, so we will need to perform an energy integration. Additionally, before integrating we should also take into consideration the finite experimental resolution through a convolution:

$$R(\omega) = \frac{1}{\sigma\sqrt{2\pi}} \cdot e^{\frac{-\omega^2}{2\sigma^2}}$$

such that $\mathrm{FWHM}^{R(\omega)}$ [meV] $= 2\sqrt{2\log(2)} \cdot \sigma$.

The expression to be implemented will then be:

$$I^{sim}(\mathbf{q}) = \int_{\omega_{min}}^{\omega_{max}} [A \cdot b(\omega) \cdot \mathbb{I}mD(\mathbf{q},\omega)] * R(\omega)\, d\omega =$$

$$= \int_{\omega_{min}}^{\omega_{max}} [\frac{A}{e^{\omega/k_B \cdot T} - 1} \cdot \mathbb{I}m(\sum_{n=1}^{4} [\omega_0 + \nu \cdot \eta_n(\mathbf{q}) - i\omega \cdot \gamma - \frac{\omega^2}{\Omega}]^{-1})] * [\frac{1}{\sigma\sqrt{2\pi}} \cdot e^{\frac{-\omega^2}{2\sigma^2}}]\, d\omega$$

This leaves us with an analytical expression that can well be implemented with mathematical analysis tools. The physically relevant parameters that we can thus play with to act on I($\mathbf{q}$) are ω_0, ν, Ω, γ and A.

A theoretical review on quantum critical phenomena can be found in Ref. [53] and [54].

3.3 Reference parameters

The upcoming work has the purpose of illustrating what the model described in the previous Section produces by using a mathematical analysis program, which in our case will be MATLAB®. The following study will therefore give us a description of the functional shape of the RIXS intensity relative to the CDF broad peak (BP), both in energy (dispersion) and momentum space. This is an interesting and compelling task in light of the ultimate goal of fitting actual experimental curves. We must indeed grasp what features the model is capable of producing, how the

objective function behaves with respect to its variables and, most importantly, how it responds to changes of physically relevant parameters such as ω_0, ν, γ and Ω.

Evidently, if we want to be able to get started, we need a reasonable set of parameters to begin with: a reference. In these regards, as underlined many times, we should go back to experimental measurements and try to extract as much information as possible. This task has indeed already been carried out by the creators of the model, in collaboration with our research group in Ref.s [34] [55].

Nevertheless, it is quite interesting to understand how a first-approximation estimation of the value of ω_0 can be obtained from high resolution (HR) RIXS spectra. Indeed, ω_0 represents the characteristic energy of charge density fluctuations and can be identified by seeking the energy associated to the signal's maximum within the spectrum. As shown in Fig. 3.9, the peak seems to fall around $\sim$ 10 - 15 meV. Another quite insightful approach which we decided to use to provide a first evaluation of ω_0 is the following:

1. Plot the experimental intensity curves along the direction HH as a function of temperature, parametrically indexed by momenta values: I^{exp}(T;HH).

2. In accordance to the assumption that the temperature dependence of the supposed background is ruled by the Bose-Einstein distribution develop the following equation, where $n = \frac{1}{e^{\omega_0/k_B \cdot T} - 1}$:

   (a) Probability of a Stokes process: $B_1 \cdot$ (n+1)

   (b) Probability of an Antistokes process: $B_2 \cdot$ n

   (c) We can safely assume to have $B_1 = B_2 \equiv B$, so that the total probability is B $\cdot$ (2n+1)

   (d) Consider a T-independent, q-dependent offset A(q) so that you can model I^{sim}(T;HH) = A(q) + B $\cdot$ (2n+1) (where *sim* stands for simulated).

3. Fit I^{exp} with I^{sim} and extract a fixed value of ω_0.

This procedure is displayed in Fig. 3.10 and produced a value $\omega_0 \sim 13$ meV, absolutely consistent with the amount observed from HR spectra.

Arguably, the A(q) curve in momentum space extracted using this method could be interpreted as a background which ought to be subtracted from the signal along both HH and H0 to isolate the CDF-related intensity and provide a better fit; this will be further discussed in Chapt. 4.

Regarding ν, we know from the role it plays in the equations, that it acts as a coefficient regulating the width of the dispersion curves where, in a parabolic approximation developed in proximity of the CDF peak: $\omega(\mathbf{q}) = \nu \cdot (\mathbf{q} - \mathrm{Q}_c)^2$, hence $[\nu] = \frac{eV}{r.l.u.^2}$. Previous observations have found an approximated value of $\nu \approx 1.4 \frac{eV}{r.l.u.^2}$, which seemed to produce reasonable dispersions [34].

Ω acts as a frequency cut-off for CDF, and quantitative estimations of its value have found it around $\sim$ 30 - 60 meV [55], we will start with 30 meV. Parameter γ is a damping factor and, in our initial analyses, will be kept equal to 1 (ineffective).

The equation to be implemented, as presented in Sect. 3.2 is Eq. 3.1 which, in this analysis, will be used without the convolution with the experimental resolution in order to describe exactly what the model results in, the convolution will be added for the fitting itself in the following chapter.

In order to be able to reproduce the four peaks in two-dimensional reciprocal space (q_x,q_y) which are experimentally observed at ($\pm\mathrm{Q}_c$,0), (0,$\pm\mathrm{Q}_c$), and also account for the energy dependence, we need to simulate I as a three dimensional array: a cubic matrix. This way, by fixing ourselves at arbitrary values along one of the two q axes (let's say $\mathrm{q}_y = 0$ r.l.u.), we can visualize the dispersion relation of the CDF peaks, namely I(q_x,ω). Otherwise, by keeping both q_x and q_y variable and performing a numerical integration along the third dimension of the array (i.e. the energy dimension), we obtain $\int_{\omega^{min}}^{\omega^{max}} I^{sim}(q_x, q_y, \omega)\, d\omega = I^{sim}(q_x, q_y)$ (the numerical integration in MATLAB®, will be carried out using the trapezoidal method). If then also in this case we fix $\mathrm{q}_y = 0$ r.l.u. we obtain the equivalent to experimental measurements along H0. It should be noted that in doing so we are keeping temperature constant. If the temperature dependence were to be added as well, the array representing CDF intensity values would become four dimensional. For the time being we will keep it fixed and then, when our interest will be in the temperature dependence, we will iteratively generate the 3D array for different T values, thus using a loop (as done to generate Fig.s 3.25 and 3.24).

A brief discussion on how different methods used to generate $\mathrm{I}^{sim}(\mathbf{q})$ are reflected on computation times is attached in Appendix A. Clearly, producing these simulations is quite fast a process, but we must keep in mind that this procedure, or something similar to it, will later be called recursively by the fitting algorithm, so we should try to keep it as quick as possible to begin with.

Finally, by fixing the peak position to $\mathrm{Q}_c^{x,y} = 0.3$ r.l.u., and using $\omega_0 = 12.5$ meV, $\nu = 1.4 \frac{eV}{r.l.u.^2}$, $\Omega = 30$ meV, $\mathrm{A} = 10^{-3}$, T = 150 K, $\gamma = 1$ we obtain the plots shown

in figures 3.11 and 3.12. In all following images I indicate the energy loss axis with "Energy" which corresponds to ω in all equations, and I label "Intensity" the values taken by I^{sim} in arbitrary units.

3.4 Dependencies

In Fig.s 3.14 and 3.15, I fixed coordinate q_y to 0 and plotted the dispersion relation produced by Equation 3.1, i.e. intensity values versus q_x and ω. We see the curves disperse in a non-trivial way, generating two main peaks in ($\pm Q_c$,0) with ω_0 in the neighborhood of 10 meV, and several other features for variable q_x positions. In Fig. 3.15, dispersions are shown to be periodic in reciprocal space (in this case along q_x, but the behavior is analogous along q_y). In Fig. 3.13 I sectioned the CDF dispersion in (Q_c,0), thus producing a spectrum in correspondence of the main peak and I furthermore introduced how experimental resolution affects measurements by smearing out spectral features which are too small to be resolved, this will lead us (in Sect. 4.1) to an interesting discussion on how the fitting should be structured.

In the series of figures that follow, from 3.16 to 3.23, I show how deviations from reference values of parameters ν, ω_0, Ω, γ reflect on the correspondent intensity profile, both in terms of dispersions evaluated along the (q_x,0) direction and in terms of energy-integrated $I(q_x,q_y)$ curves. In order to isolate the effect of each parameter, all others are kept constant to reference values indicated shortly above.

Concerning a comparison between the temperature dependence of simulated curves and that of experimental ones, figures 3.24 and 3.25 show that the match is quite acceptable as long as we remain far from the peak position (i.e. about a HWHM away from it). On the other hand, in ($\pm Q_c$,0), (0,$\pm Q_c$) the simulation fails to reproduce the confinement of the intensity maxima upon a rise in T, and generates a wide excursion which is evidently non-physical. Keeping in mind the effect of ω_0 on the amplitude of CDF peaks, as shown in Fig. 3.19, we could expect that the approximation of keeping this parameter fixed could be misleading. Indeed, from these results, we might anticipate ω_0 to have a growing character with respect to temperature. In this framework, the T increase would lead to an increase in peak amplitude, but at the same time the value of ω_0 would also rise, thus producing the opposite effect. The combination of these two is supposedly causing the experimentally observed "squeeze" of intensity maxima in correspondence of CDF positions in

reciprocal space. This is also in line with the reasoning developed in Sect. 3.2 while discussing the temperature dependence of the FWHM of $I^{exp}(\mathbf{q})$. In these regards, we shall prepare to fit experimental curves with simulations having variable-in-T parameters.

This analysis proves that dispersion relations (hence also spectra), and energy-integrated $I^{sim}(q_x,q_y)$ curves, show a strong dependence on the studied parameters in a non-trivial manner. Nevertheless, intensity curves display reasonably realistic functional shapes if qualitatively compared to experimental observations. We are thus motivated to move on with the implementation of a fitting routine in the hope of succeeding in reproducing experimental data quantitatively, while extracting values of ω_0, ν, Ω, γ.

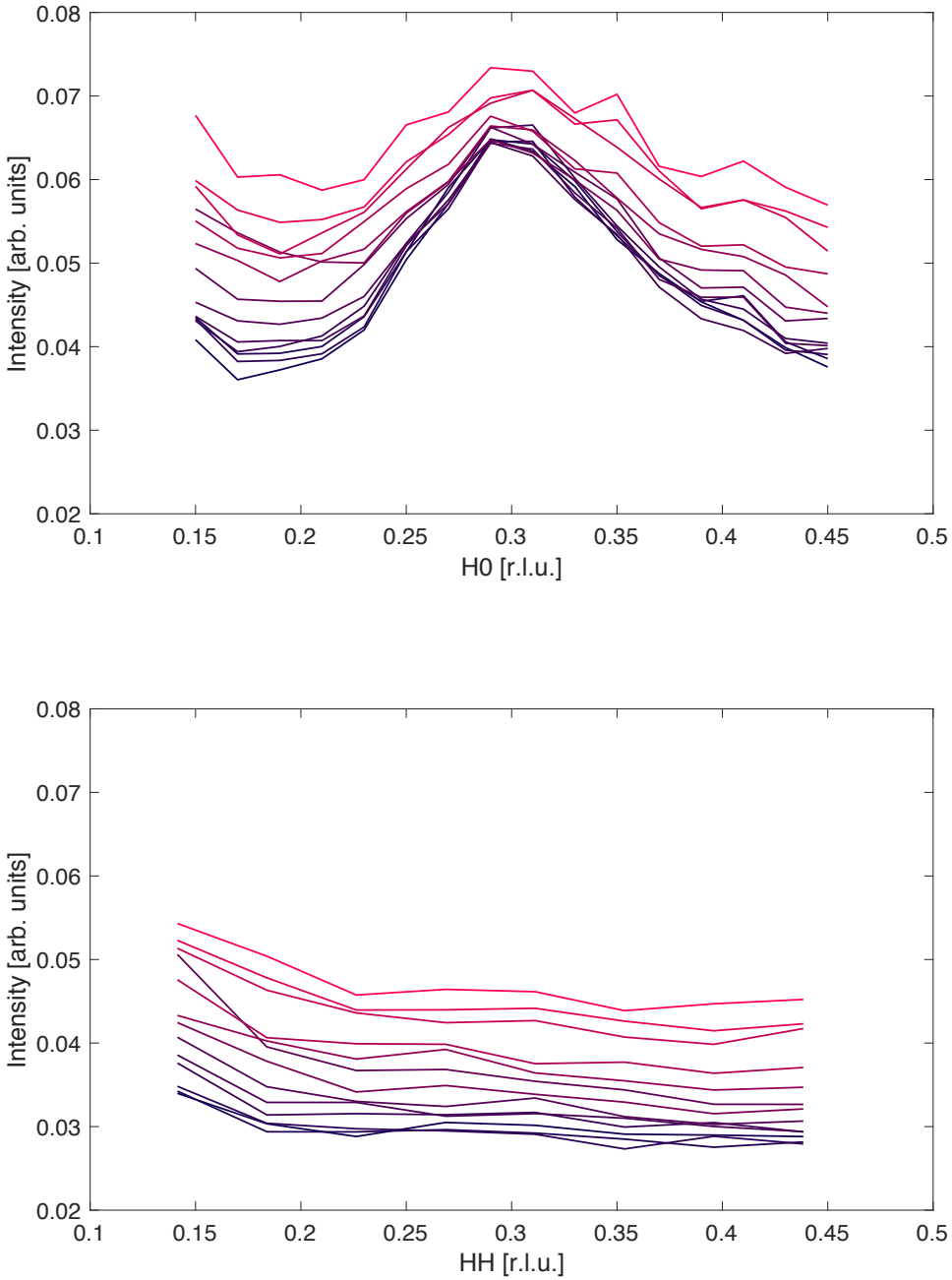

Figure 3.7: Data plots YBCO.

I(q;T) curves plotted as a function of momentum along H0 (above) and HH (below), ranging from T_{min} = 20 K to T_{max} = 290 K. These curves are obtained by integrating (for each fixed q and T) the quasi-elastic region of RIXS spectra. This region has been defined as the range [-100 meV, 35 meV], so as to minimize the contribution coming from the rather strong high-energy phonons (which appear clear in Fig. 3.9). Darker curves represent data relative to lower temperatures and, vice versa, lighter red curves show higher-T intensity profiles (relative data in Tab. 3.5).

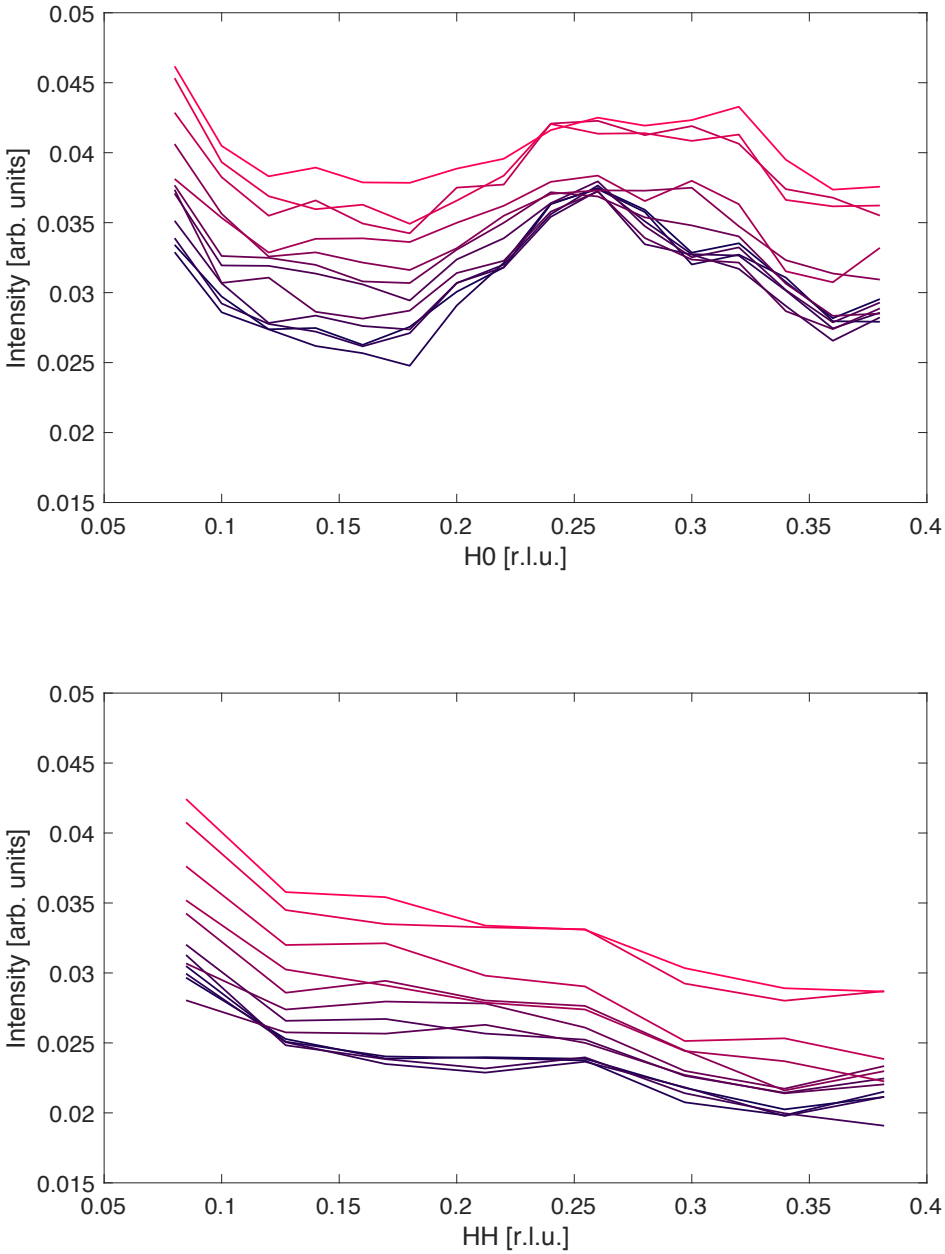

Figure 3.8: Data plots Bi2212.

I(q;T) curves plotted as a function of momentum along H0 (above) and HH (below), ranging from T_{min} = 20 K to T_{max} = 260 K. These curves are obtained by integrating (for each fixed q and T) the quasi-elastic region of RIXS spectra. This region has been defined as the range [-100 meV, 35 meV], so as to minimize the contribution coming from the rather strong high-energy phonons. Darker curves represent data relative to lower temperatures and, vice versa, lighter red curves show higher-T intensity profiles (relative data in Tab. 3.6).

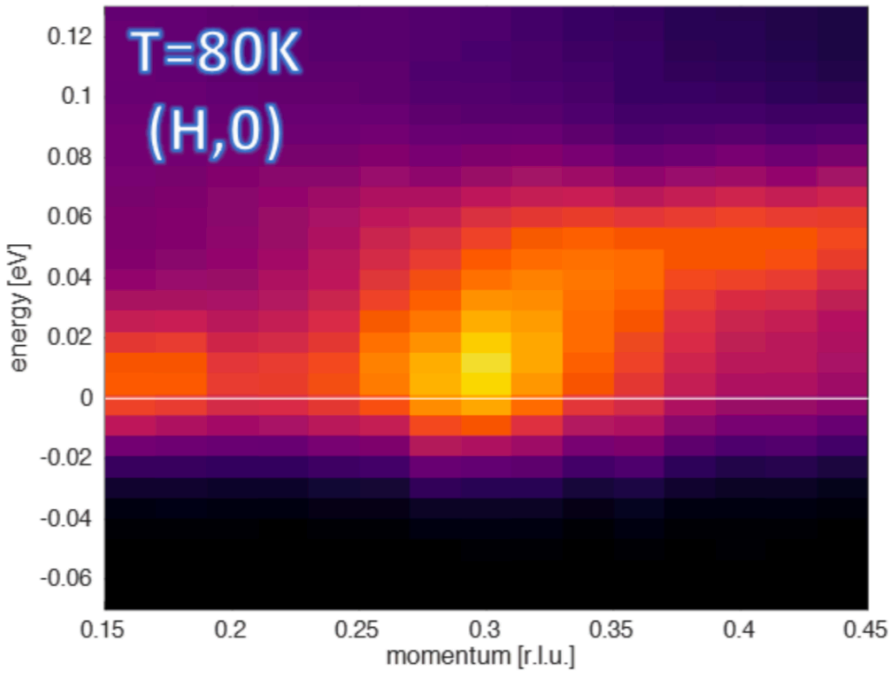

Figure 3.9: CDF spectrum: High resolution (i.e. $\sim$ 35 meV) energy-vs-q RIXS maps measured on the slightly overdoped YBCO thin film. The white horizontal line indicates the zero energy-loss locus of points, thus highlighting how the charge density fluctuation peak is found at finite energies ($\omega_0 \approx 10$ meV), suggesting its dynamical character. At higher energies (i.e. $\sim$ 50 - 60 meV) especially at high q, we see the breathing-phonons branch, which we're currently not interested in.

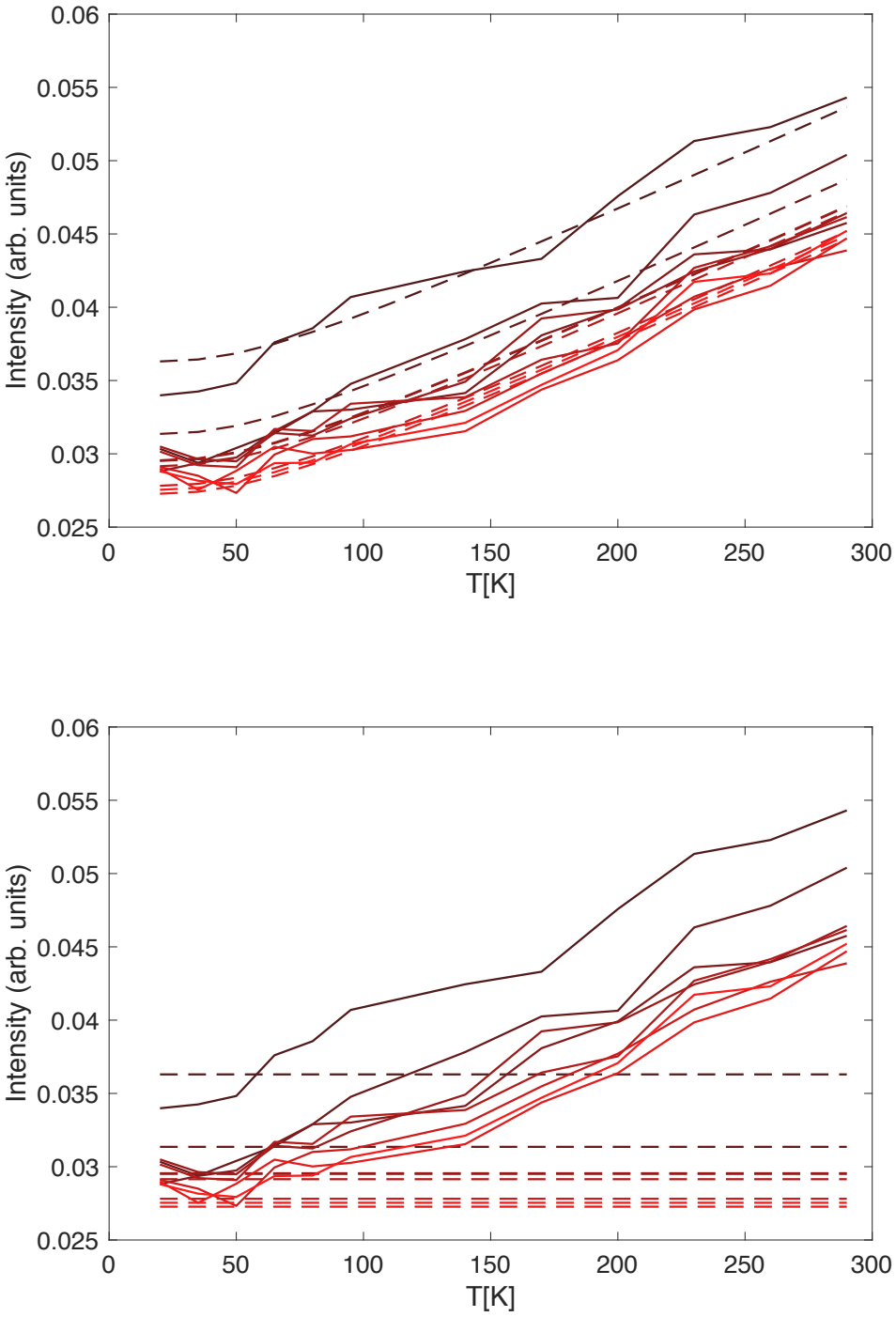

Figure 3.10: Bose-like fitting along HH on YBCO sample.

Top panel. I^{exp}(T;HH) (full lines) vs I^{sim}(T;HH) (dashed lines) parametrized on momenta (lighter red corresponds to higher q along HH).

Bottom panel. I^{exp}(T;HH) (full lines) vs A(q = HH) (dashed lines) which is set to be constant in temperature.

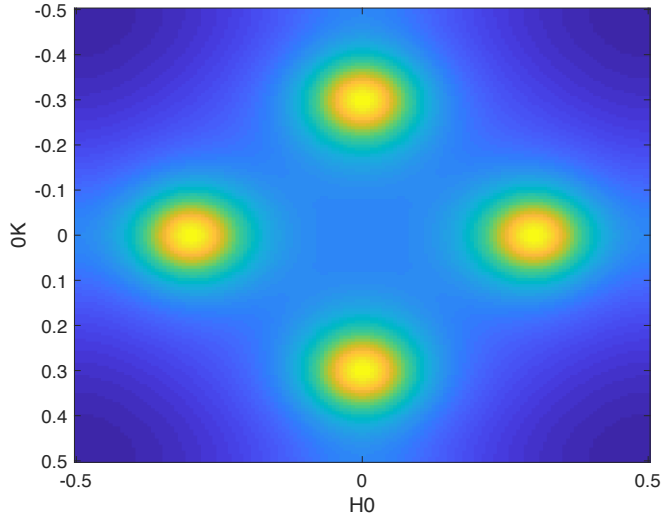

Figure 3.11: Top view: intensity peaks in 2D reciprocal space

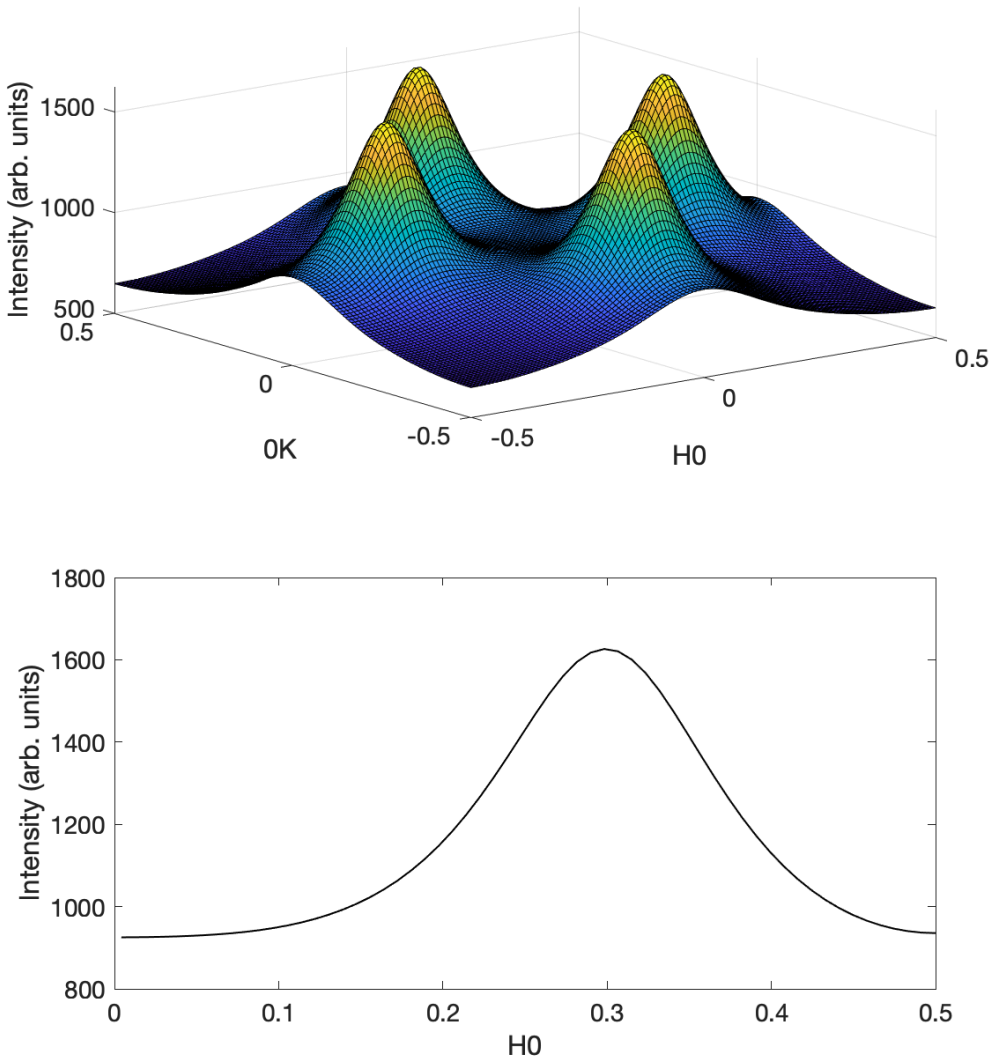

Figure 3.12: Top panel. Intensity peaks in 2D reciprocal space.
Bottom panel. Intensity peak section along q_x, i.e. the H0 direction.

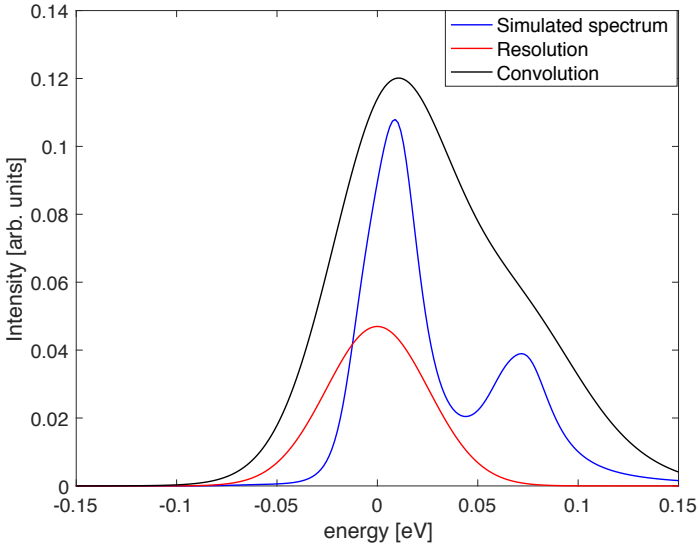

Figure 3.13: CDF spectrum in (Q_c,0). Simulated spectrum in (Q_c,0), hypothetical experimental resolution of 60 meV, and convolution between the two curves showing significant smearing out of spectral features.

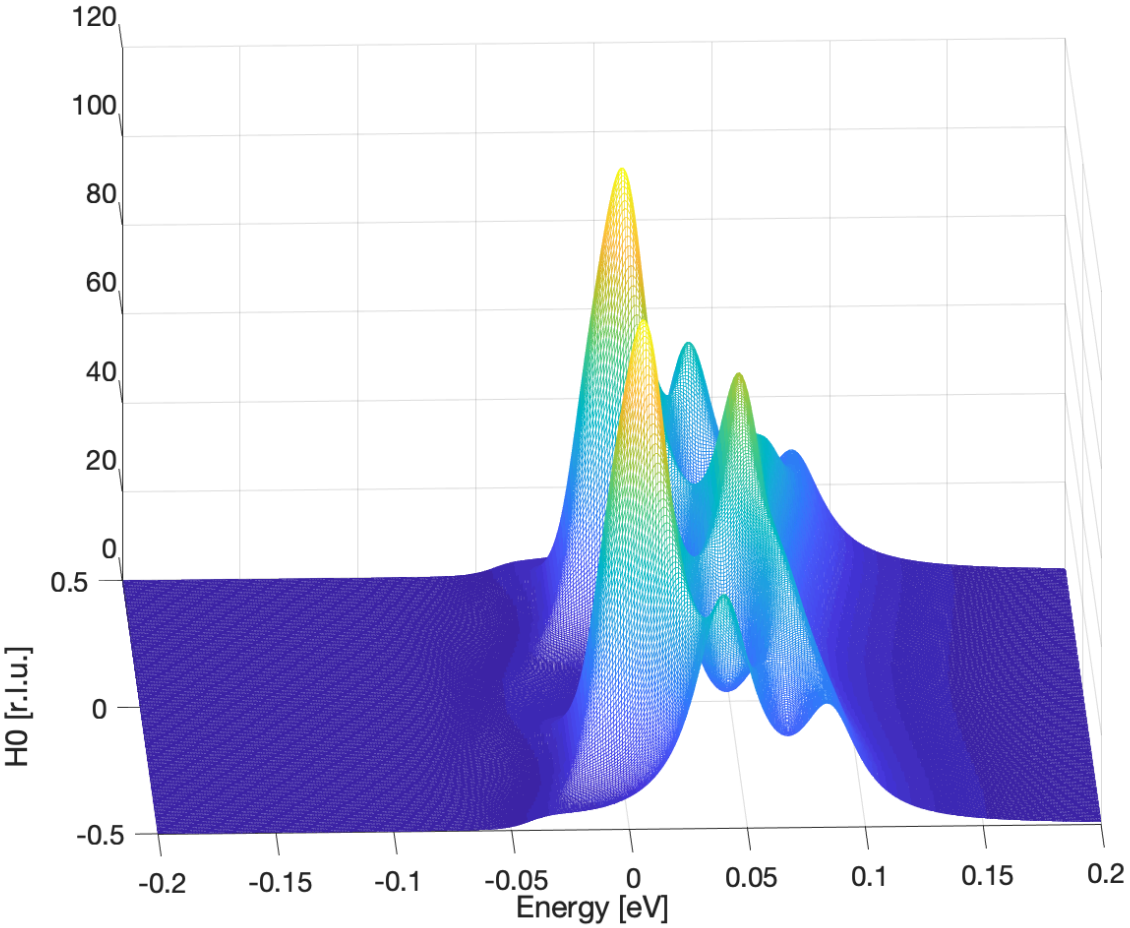

Figure 3.14: CDF dispersion. Intensity plot in the (q_x,ω) plane showing non-trivial dispersion.

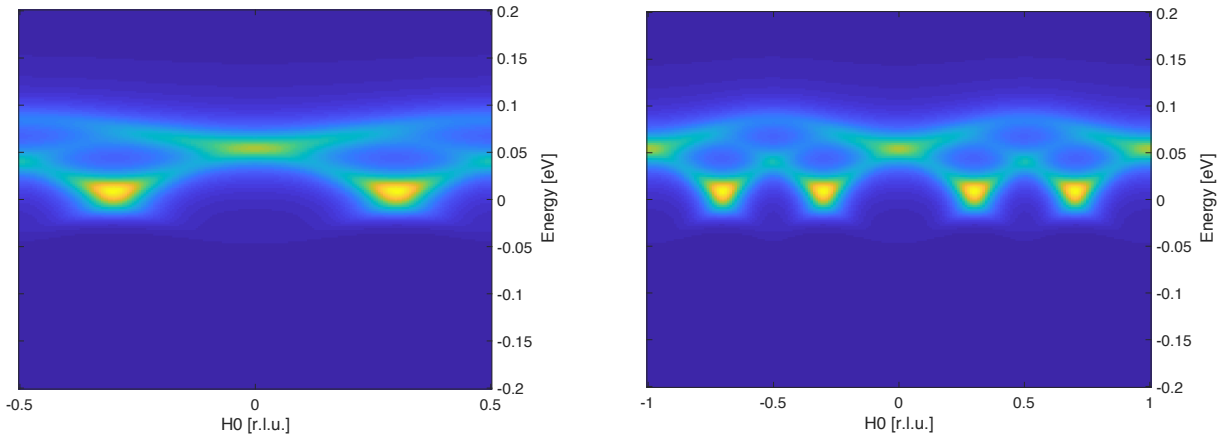

Figure 3.15: CDF dispersion, top view.

Left panel: Top view, intensity plot in the (q_x,ω) plane.

Right panel: Same but plotted on a larger q_x interval to show periodicity.

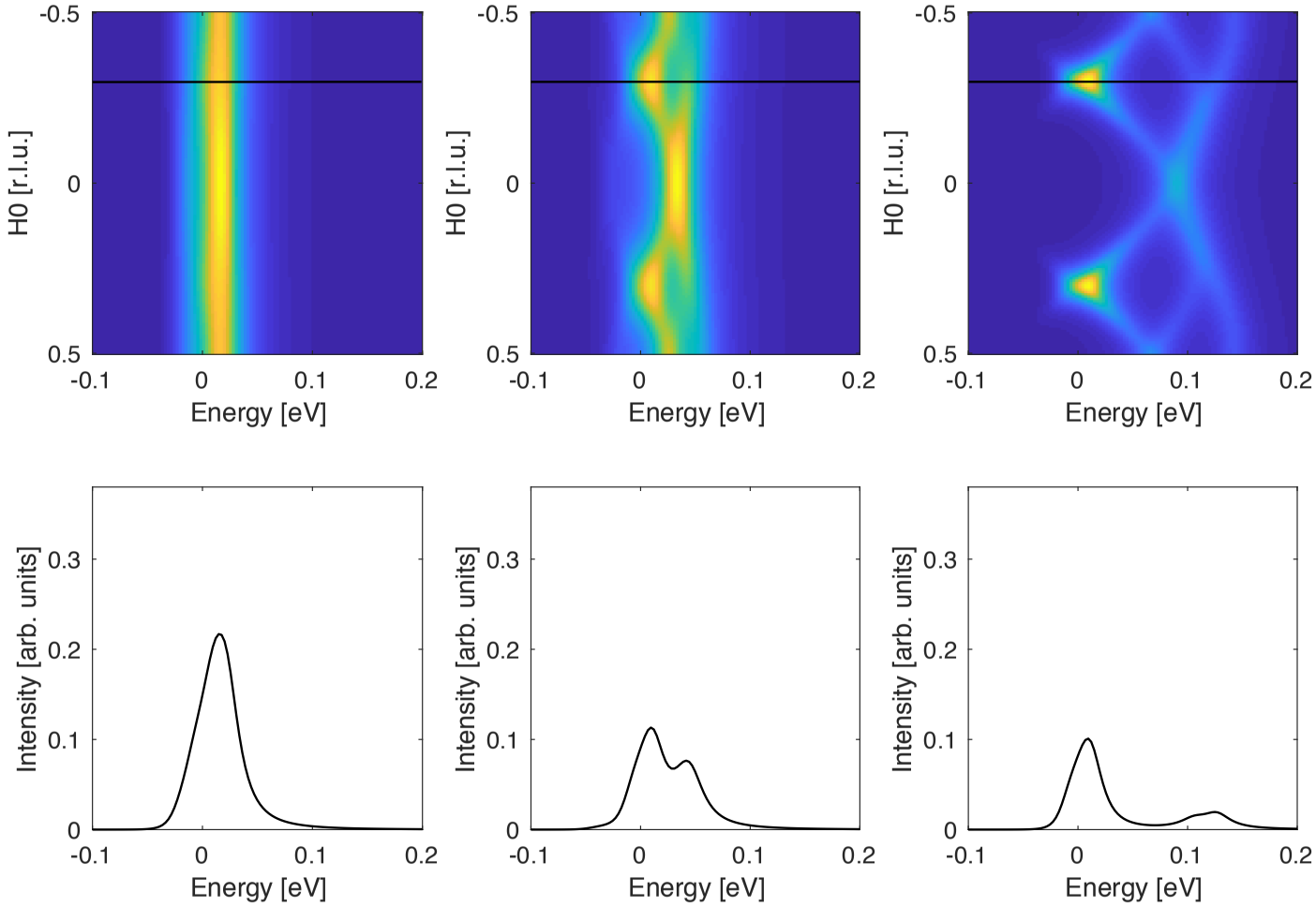

Figure 3.16: Effect of ν on dispersion.

Effect of ν ranging from 100 - 500 - 4000 $\frac{meV}{r.l.u.^2}$ (left to right). Bottom panels show the above ones sectioned along black lines corresponding to (-Q_c,0) r.l.u. (identical to (+Q_c,0) r.l.u.). This parameter has the expected role of regulating the width of dispersions, a low ν renders CDF nearly dispersionless whereas a higher value implies a sharper ω(q) profile with tighter branching.

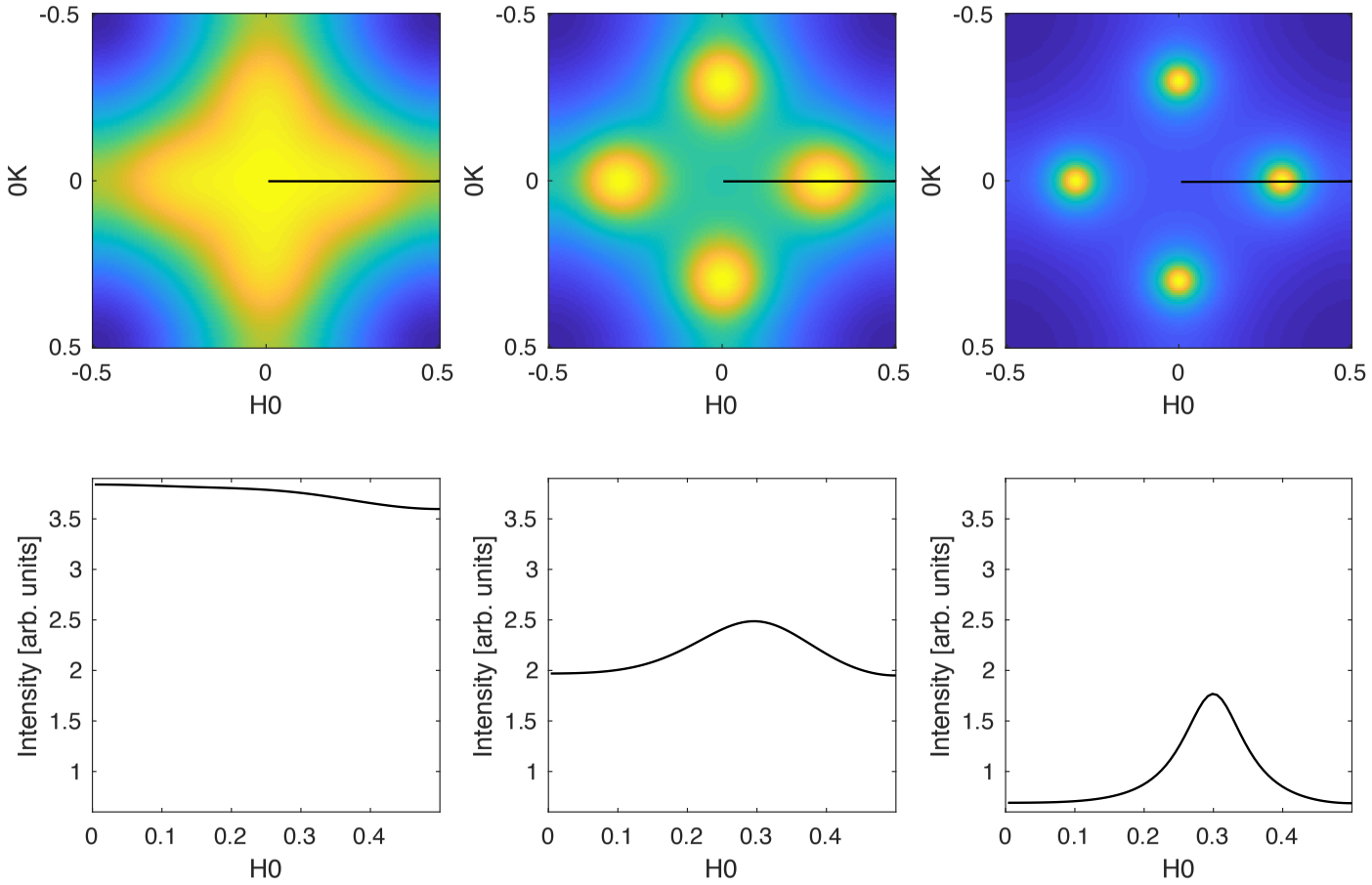

Figure 3.17: Effect of ν on $\mathbf{I(q_x,q_y)}$.

Effect of ν ranging from 100 - 500 - 4000 $\frac{meV}{r.l.u.^2}$ (left to right). Bottom panels show the above ones sectioned along black lines corresponding to the H0 direction. The variation is extremely wide, low ν values imply a complete deviation from the experimentally observed CDF profile, leading to a strong intensity rise in (0,0) r.l.u.

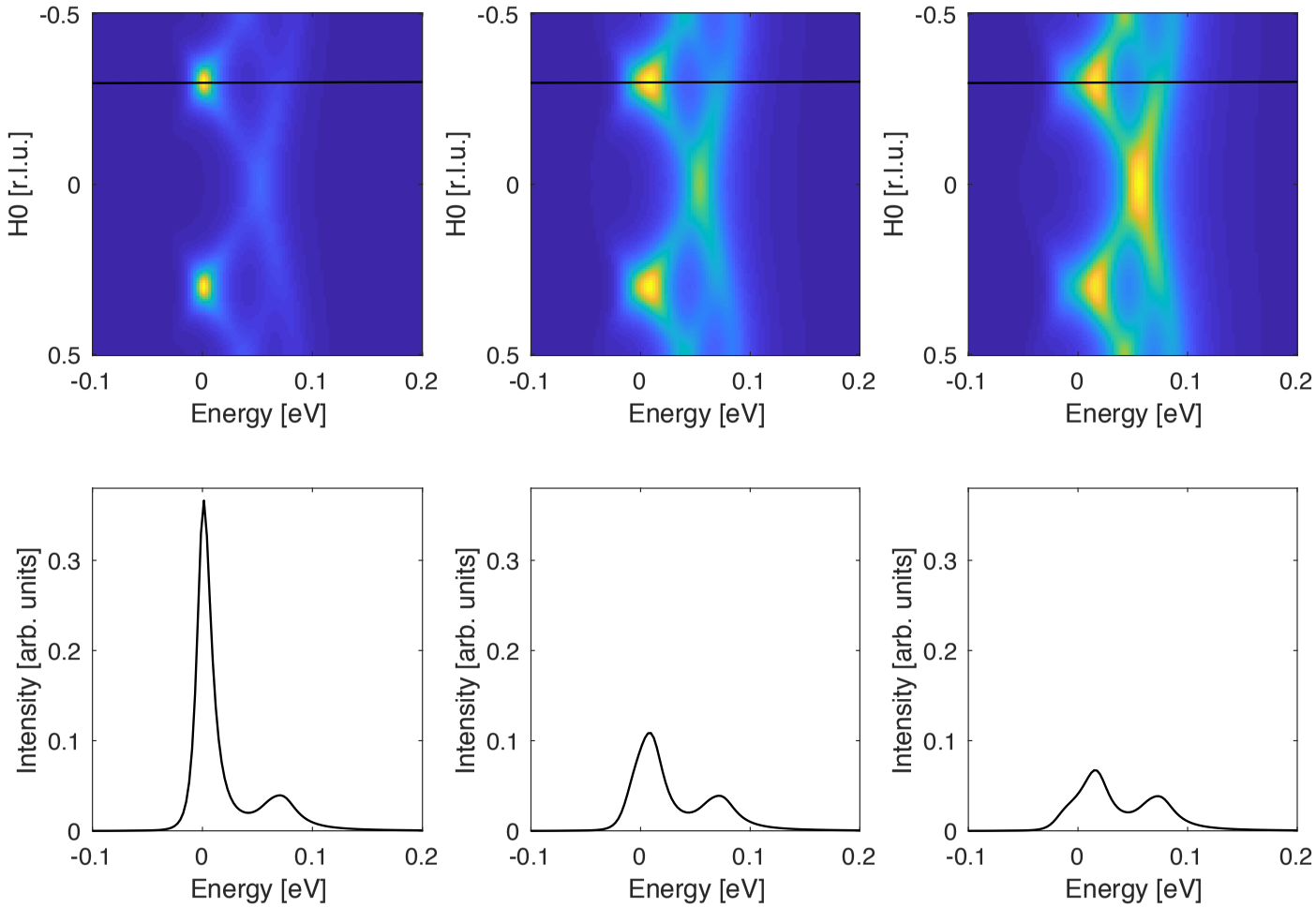

Figure 3.18: Effect of ω_0 on dispersion.

Effect of ω_0 ranging from 6 - 12 - 18 meV (left to right). Bottom panels show the above ones sectioned along black lines corresponding to (-Q_c,0) r.l.u. (identical to (+Q_c,0) r.l.u.). Lower values of ω_0 produce higher peaks concentrating most states in correspondence of Q_c, whereas for higher values we see that modes are more dispersed and another peak becomes relevant in (0,0) r.l.u. due to the superposition of states leaking from ($\pm Q_c$,0) r.l.u.

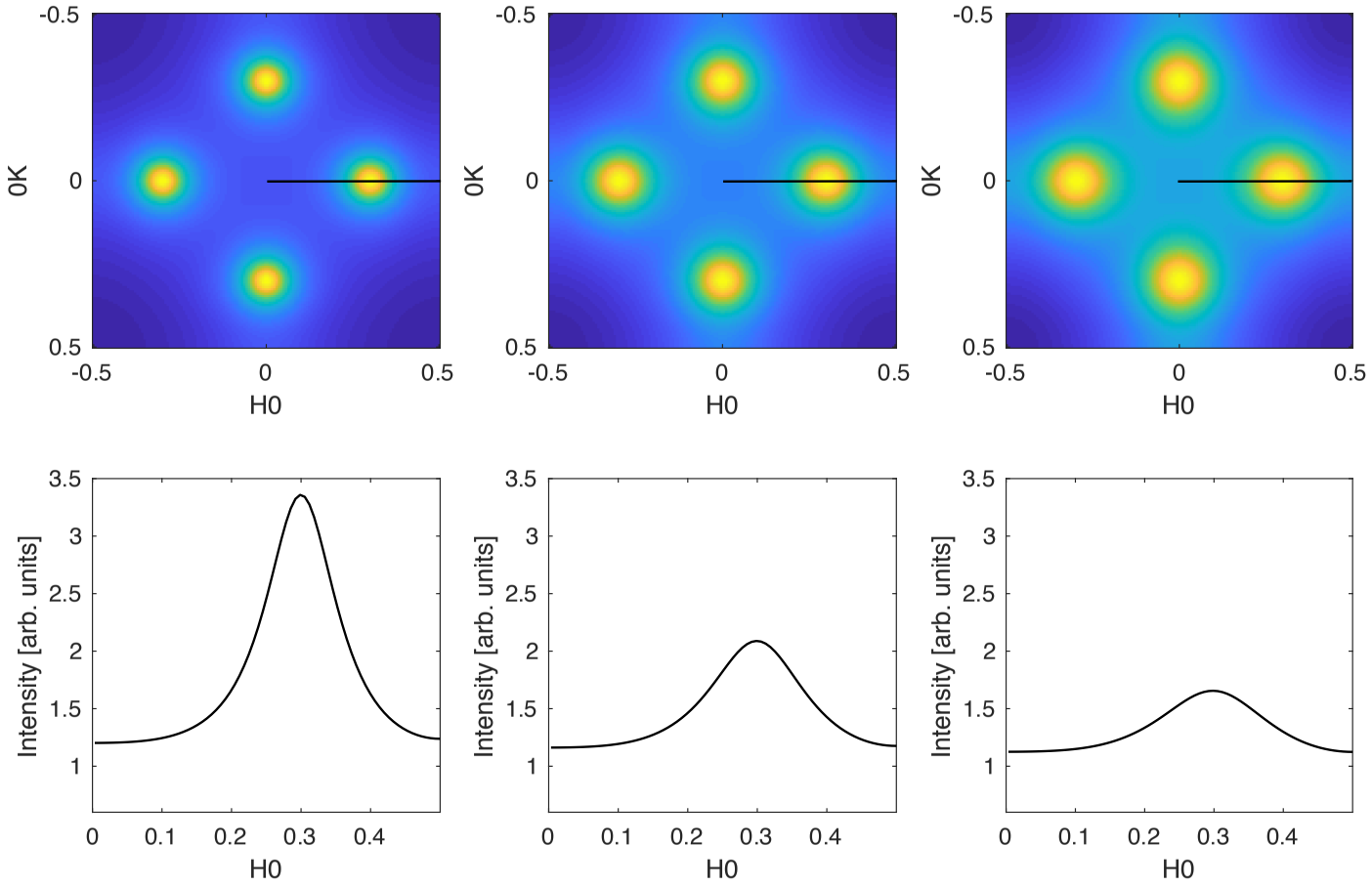

Figure 3.19: Effect of ω_0 on I(q_x,q_y).

Effect of ω_0 ranging from 6 - 12 - 18 meV (left to right). Bottom panels show the above ones sectioned along black lines corresponding to the H0 direction. I(q_x,q_y) peak amplitude shows a marked increase when ω_0 decreases, and at the same time also its FWHM grows, consistently with our knowledge that $\omega_0 = \nu \cdot (\text{HWHM})^2$.

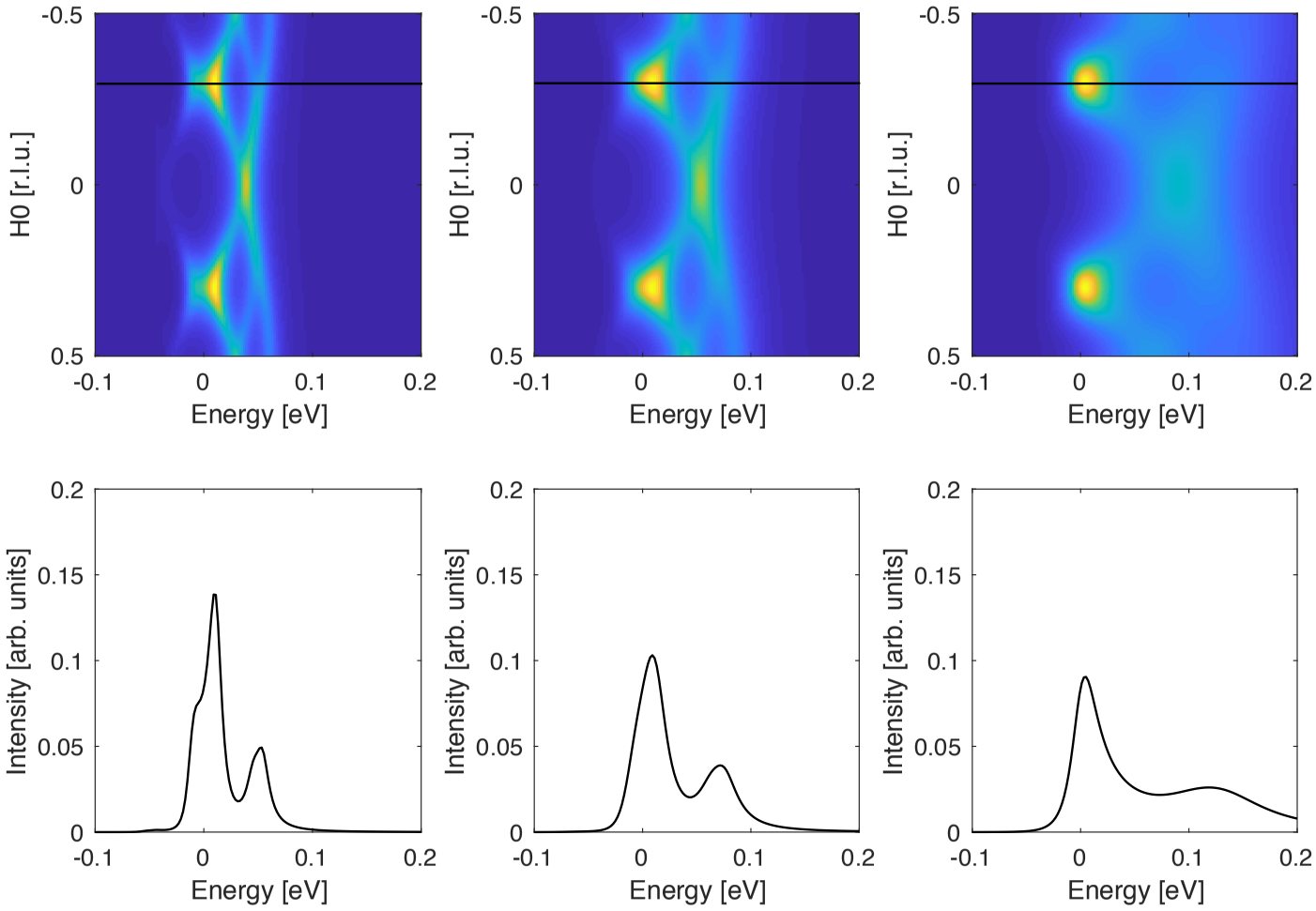

Figure 3.20: Effect of Ω on dispersion.

Effect of Ω ranging from 15 - 30 - 100 meV (left to right). Bottom panels show the above ones sectioned along black lines corresponding to (-Q_c,0) r.l.u. (choice identical to (+Q_c,0) r.l.u. due to symmetry). An increase in Ω is reflected onto CDF dispersion relations as a fading-out of the sharp edges which characterize dispersions at lower Ω's.

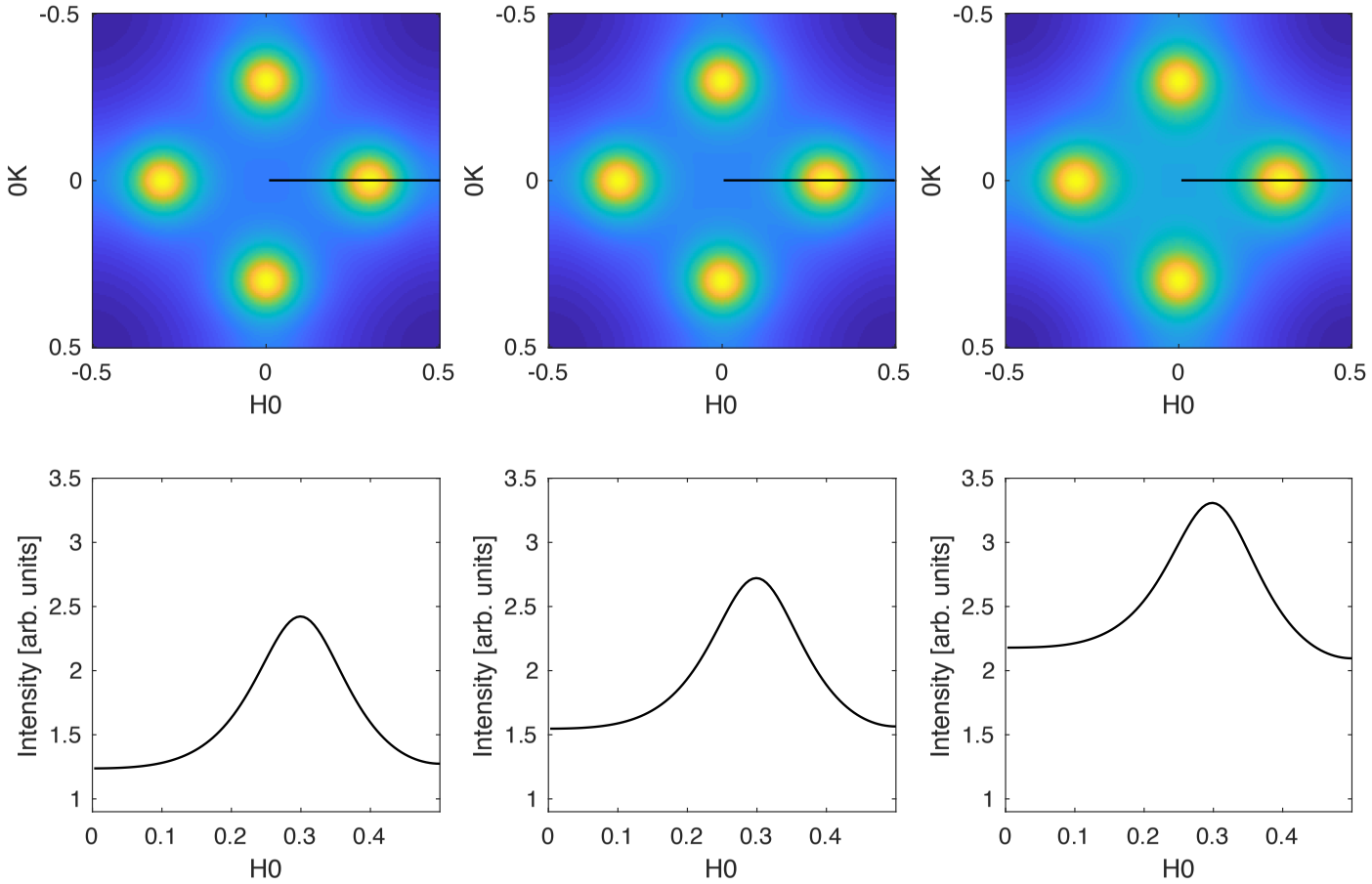

Figure 3.21: Effect of Ω on I(q_x,q_y).

Effect of Ω ranging from 15 - 30 - 100 meV (left to right). Bottom panels show the above ones sectioned along black lines corresponding to the H0 direction. Ω evidently provides a rigid vertical shift of I(q_x,q_y), and has no effect on the peak shape. This is likely due to an isotropic increase in spectral density, which gets integrated producing the insurgence of this baseline in momentum space.

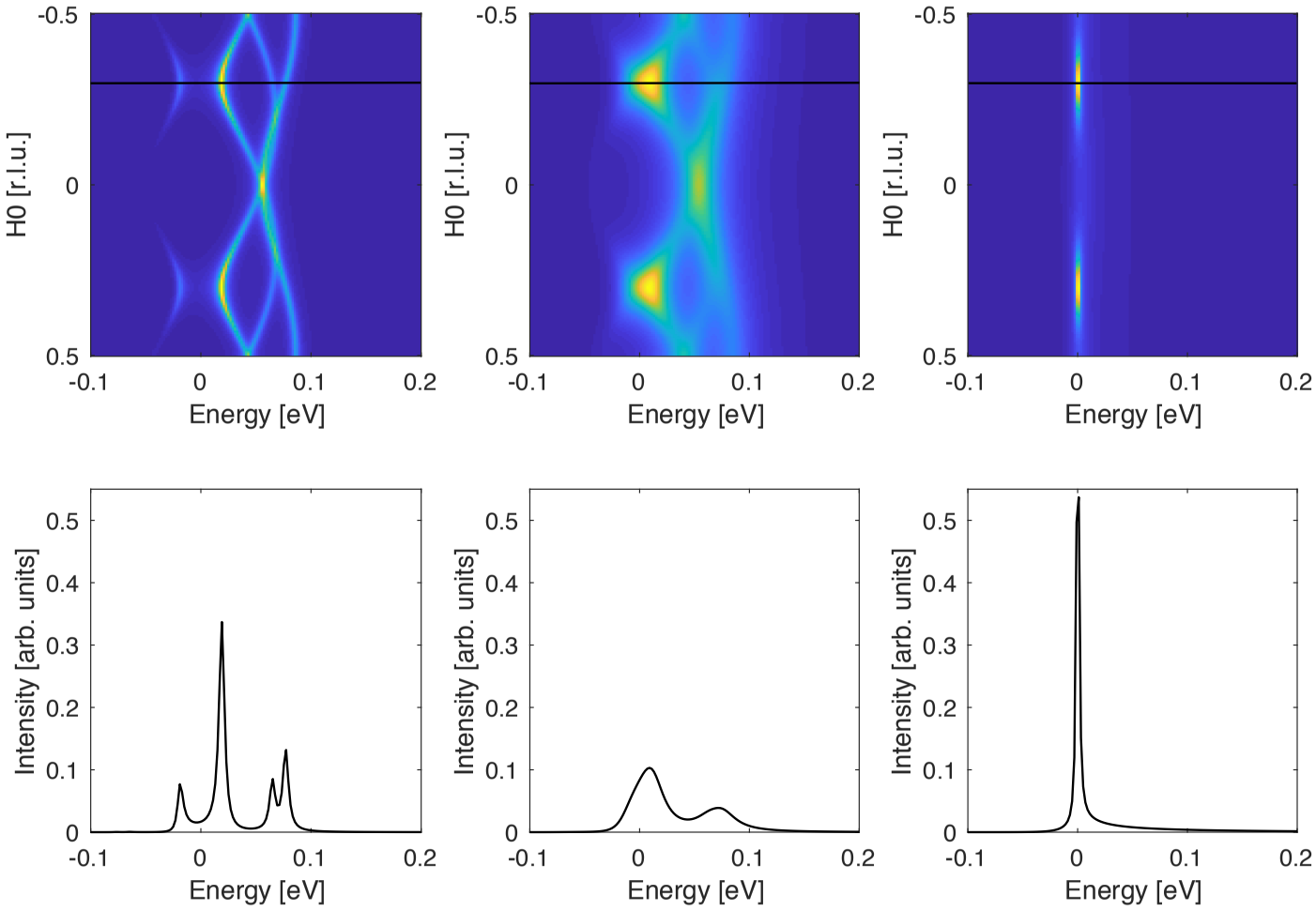

Figure 3.22: Effect of γ on dispersion.

Effect of γ ranging from 0.1 - 1 - 10 (left to right). Bottom panels show the above ones sectioned along black lines corresponding to (-Q_c,0) r.l.u. (identical to (+Q_c,0) r.l.u.). γ leads to a strong change of dispersion curves. The meaning and role of γ is rather tricky and still not fully understood, as further explained in Chapt. 4.

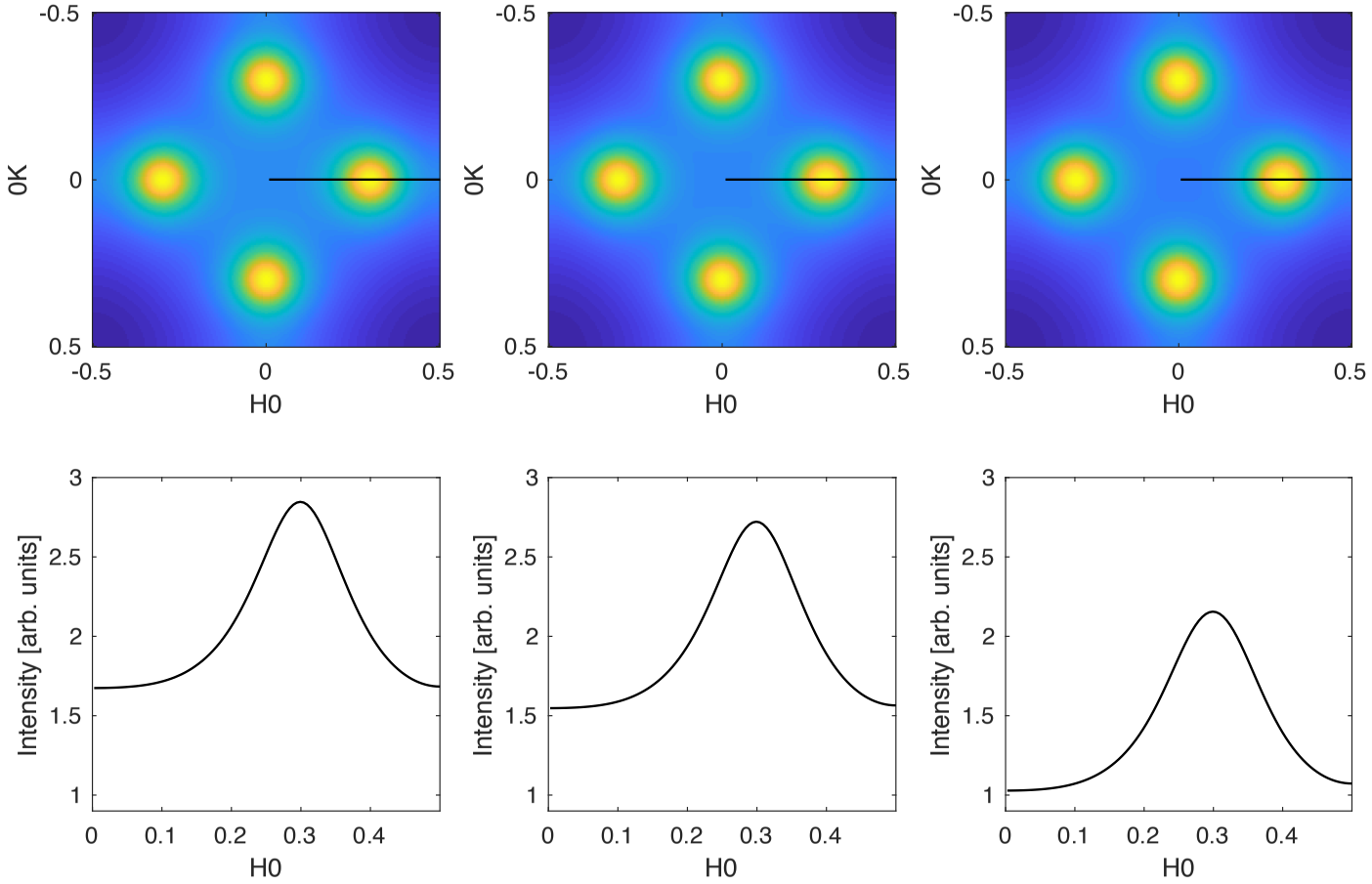

Figure 3.23: Effect of γ on $\mathbf{I(q_x,q_y)}$.

Effect of γ ranging from 0.1 - 1 - 10 (left to right). Bottom panels show the above ones sectioned along black lines corresponding to the H0 direction. A mild effect is visible for small values of γ, whereas above the value $\gamma = 1$ it does not affect the signal much. Apparently even if dispersion relations are heavily shaped by this parameter, their integral does not change significantly overall.

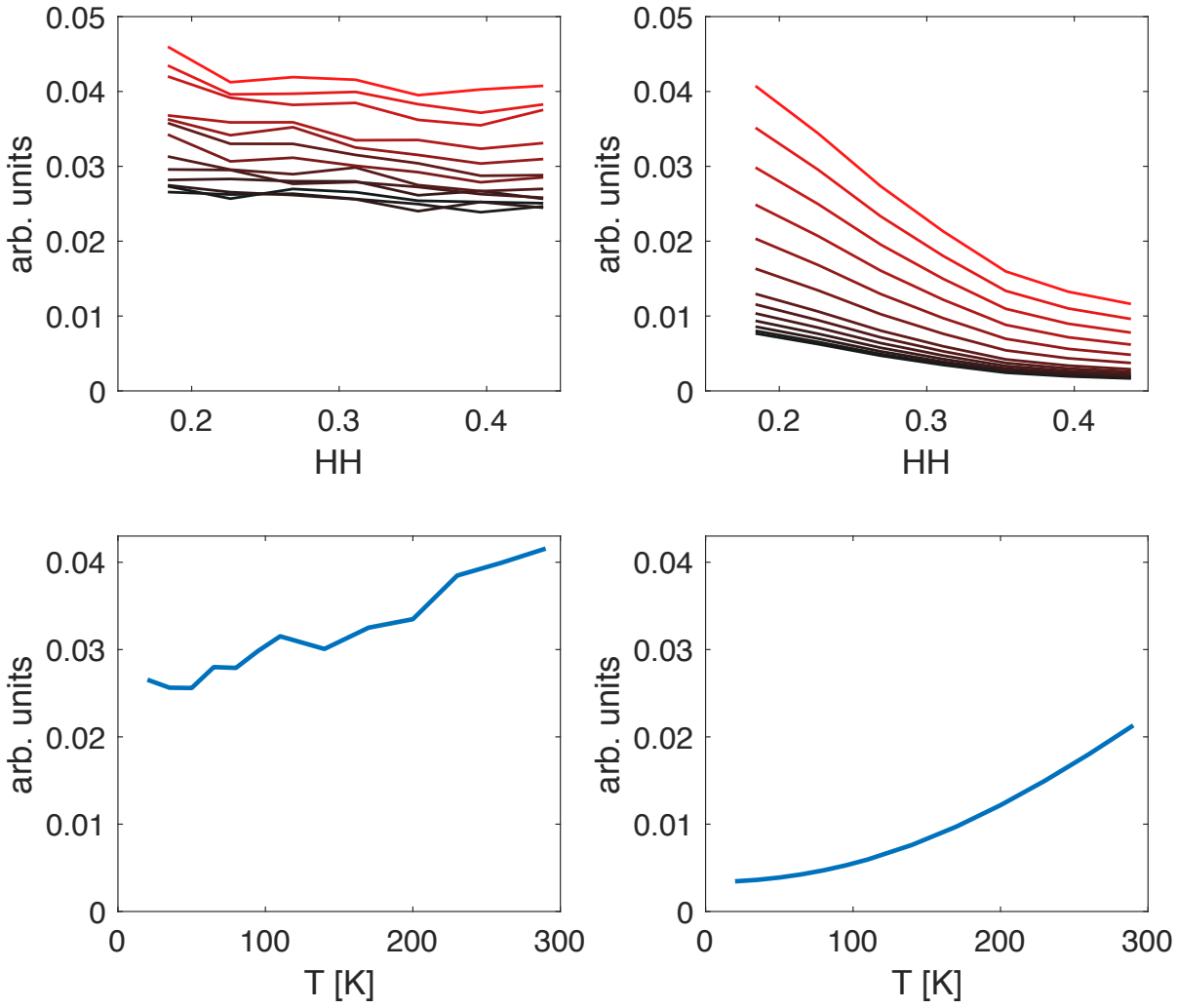

Figure 3.24: T dependence along HH.

T dependence of I(q_x,q_y) along HH experimental (left) vs simulated (right). Top panels show the increase in T through lighter red curves, whereas bottom panels are plots of I(T) in (0.3,0.3) r.l.u. The temperature dependence (increase) is quite similar among experiment and simulation given that multiplying constants and backgrounds are still arbitrarily set: the two sets of curves have a similar excursion between maximum and minimum.

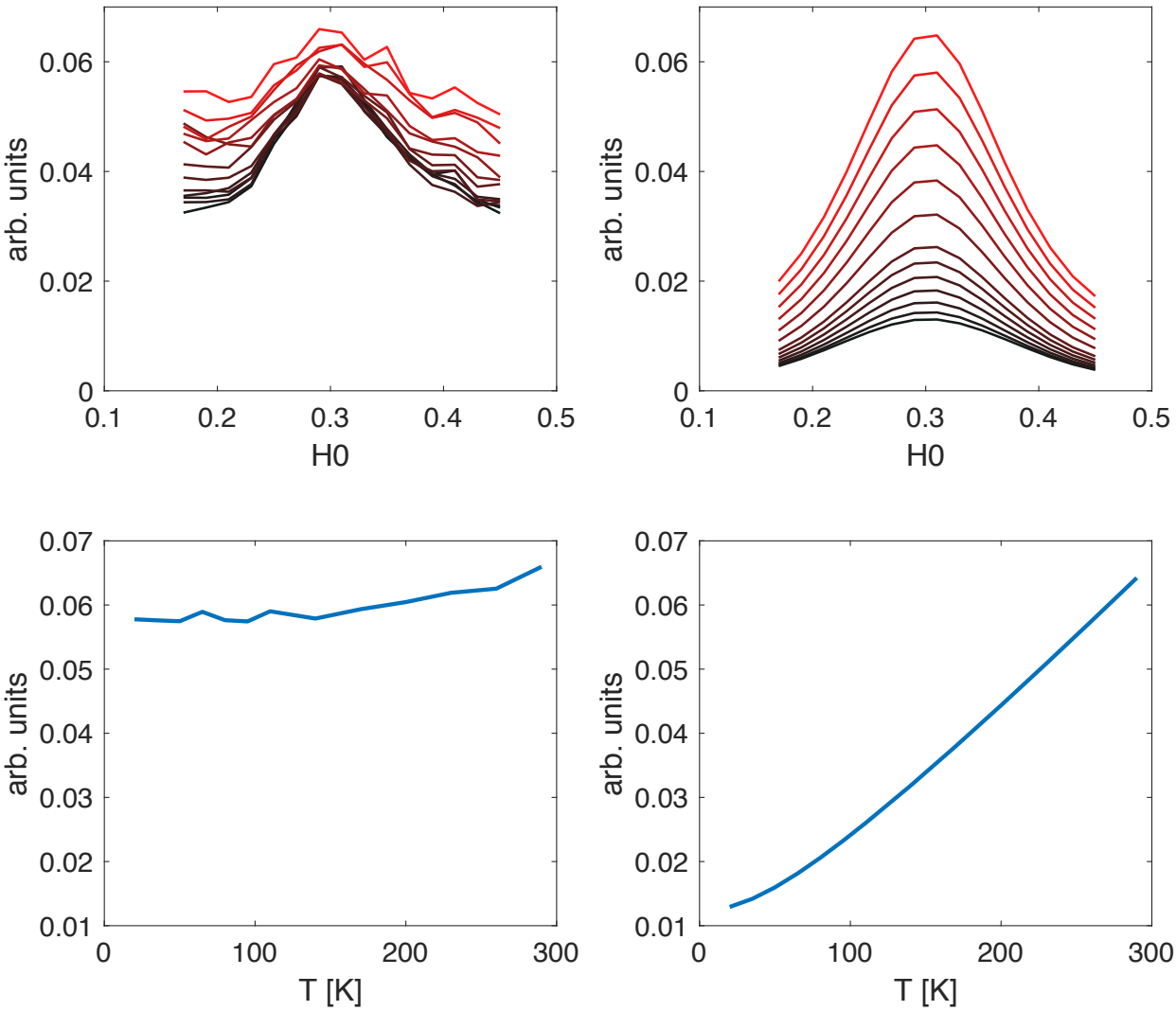

Figure 3.25: T dependence along H0.

T dependence of I(q_x,q_y) along H0 experimental (left) vs simulated (right). Top panels show the increase in T through lighter red curves, whereas bottom panels are plots of I(T) in (0.3,0) r.l.u. The temperature dependence (increase) is markedly different among experiment and simulation since the simulated set of curves has a much wider excursion between T_{min} and T_{max}.

4 The global fit

This chapter constitutes the core of the project that was carried out throughout the past months, laying roots in the analyses as yet detailed.

As we saw in Chapt. 3, the equations we are using to model charge order excitations in high-T_c superconducting cuprates produce encouraging simulated RIXS intensity profiles, characterized by a wealth of effects related to the dependencies to the many parameters at play. At this point of the analysis, our concern is whether the qualitative resemblance between simulated signals and experimental data will actually materialize into a quantitative match, for a given set of parameters. Moreover, if that were the case, we would need to discuss the implications of those findings: will they be physically meaningful? Will they match any expectation and/or previously known effect? Will they provide new insights, encouraging and directing further research and developments?

From Sect. 3.1 we know that experimental data is available in the form of a set of spectra collected for a series of 8 and 16 points in reciprocal space (respectively) along the HH and H0 directions, measured in the same way for 12 (in Bi2212) and 13 (in YBCO) different temperature values. In such a way, the full set of intensity values generates a three dimensional collection, i.e. with respect to (ω, T, q = H0) and (ω, T, q = HH). If we then proceed integrating spectra in a given energy range, we obtain the RIXS intensity only as a function of momentum, parametrized by temperature. As we have seen, actual data in this form was presented in tables 3.5 and 3.6.

A fundamental characteristic of our fitting scheme, is that we decided to implement it in such a way to simultaneously compare data and simulations relative to *all* temperatures and momenta. This means that we generate the simulation as an *intensity matrix* taking values for all (q,T) combinations, and the fitting function takes it as a whole and juxtaposes it to experimental data, which is saved in an analogous manner, and iteratively tries to minimize their difference acting on free parameters ω_0, ν, γ, Ω and a few more I will introduce shortly.

4.1 The energy dimension

At this point one could argue that, given that we are provided with an equation (3.1) which is also capable of modeling the energy dependence of the CDF peak, and given that, before integrating, we have experimental spectra, it could be wiser not to integrate at all, and instead implement the fitting routine taking into consideration all three dimensions: ω, T, q. In these regards our main concern is related to the experimental resolution since, as mentioned, our spectra were acquired with an energy-resolution of about 60 meV, simply dictated by the trade-off between the need for a large amount of data (for example on a wider T range) at the highest (i.e. best) possible resolution, and the limited available beam-time. As unmistakably shown in Fig. 3.13, the convolution between an experimental resolution of 60 meV and the CDF spectrum (simulated with reference parameters) leads to a quasi-total smearing of its spectral features. On the other hand, the integral operation which we perform over energy has the effect of increasing the noise rejection, so it helps us generating more reliable q-scans. Also, the energy-integrated measurement in most cases yields a more reliable representation of the momentum structure of the charge ordered state, due to fact that the unrelated inelastic part of the spectra usually evolves very smoothly and can be discarded as background [12]. The question is then the following: would performing a fit also on the energy dimension, which can not be fully resolved, add enough information to outweigh the noise-rejection effect which we get from the integration? This issue has no obvious answer, but one more thing should be kept in mind: computational cost. Carrying out the fitting simultaneously over temperature, momentum and energy would imply having a three-dimensional array of fitting parameters, and it is not straightforward to say that adding a whole dimension to parameters' space would result in a solvable problem with a regular pc. The energy dimension could potentially carry with it a large amount of experimental points which would need to be simulated, and being the computational cost a fast growing function of the size of the problem (cfr. Appendix A), the routine could supposedly either not converge at all or take too long a time. Nevertheless, when ultra-high resolution spectra will be available in a broad temperature range, it could be interesting to further develop this work moving on with a fitting along the energy dimension as well. Furthermore, we should note to our advantage that some of the energy-related parameters (namely ω_0 and γ) have a significant temperature dependence, so we hope that we will be able to discern their value through the use of our global fit which acts simultaneously on scans in the 20 - 290 K range.

4.2 Background

In Sect. 3.1 I highlighted how figures 3.7 and 3.8 show a rise along both H0 and HH, occurring for approximately q $\leq$ 0.17 r.l.u. in YBCO and q $\leq$ 0.12 r.l.u. in BSCCO. This behavior is not predicted by simulations, as described in Chapt. 3, and is not expected to be related to charge order phenomena. Evidently, while our model has been strictly built to reproduce the effect of charge density modulations, during a RIXS experiment we can not isolate a single phenomenon, and we end up with features ascribable to unrelated physics as well. Experimental evidence therefore highlights the presence of this ascent in the proximity of the Γ point in reciprocal space (center of the Brillouin zone), which is related to the geometry of the CuO_2 planes in the sample, but has no straightforward quantitative interpretation. Some of the hypotheses proposed to account for this rise in the measured intensity are phenomena such as intra-band fermionic (electronic) transitions, inter-band fermionic transitions allowed by the opening of the superconductive gap, phononic excitations, bosonic contributions and surface effects. Some of these, and probably more, conspire in the generation of the observed background, which is surely q-dependent, but we do not know if also temperature-related. As mentioned in Sect. 3.3, the illustrated procedure which makes use of a Bose-like dependence of $I(T)$ along HH to derive an approximated value of ω_0, can also be applied to produce a q-dependent, T-independent background, which we referred to as A(q). The result emerging from this approach is shown in Fig. 4.1.

In light of all this, we can move on picking one of the following two approaches:

- Extract a background from experimental data (e.g. A(q), as indicated), subtract it and fit this "corrected" set of curves with the simulated CDF signal.
- Add "artificially" a peak to the simulations and fit the "untouched" data with the function containing both CDF and background intensity.

There is no explicit way to discern between a correct decision and a wrong one. Certainly, subtracting some background signal from data requires us to assume that the amount which we are subtracting is reasonably close to (and not *more than*) the unwanted intensity (i.e. the portion related to other phenomena). Conversely, if we add a peak to the simulation, we can leave its amplitude and width free as fitting parameters and let the routine adjust their values to match the actual difference from experimental curves. For this reason, not being confident enough in our quantitative estimations of the background, we decided to move on with the second method, thus

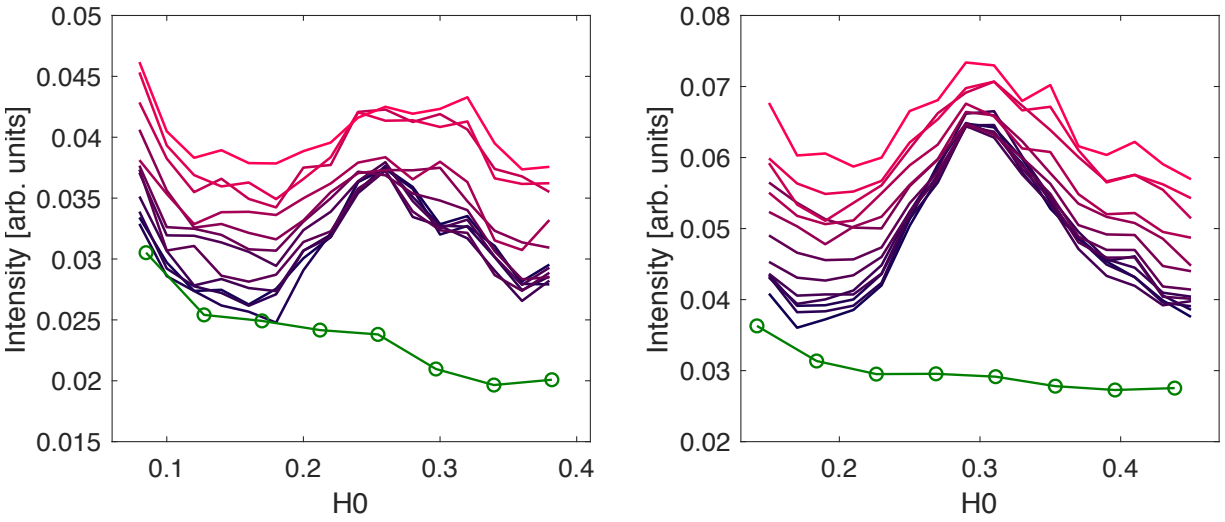

Figure 4.1: A(q) vs data along H0.
A(q) background shown as lower dotted line. From left to right: BSCCO and YBCO samples.

adding a variable peak to the simulated signal and letting the solver compute its value.

The functional shape of the "artificial peak" accounting for the background, which we will refer to as Γ-*peak* or *elastic peak*, was chosen with a comparative analysis between Gaussian, Lorentzian and power-law curves, all centered in (0,0) r.l.u., performed on a set of points which were obtained on a different sample, but reach very low momentum values ($q_{min} \approx 0.01$ r.l.u.). For this reason such a measurement provided more details about this phenomenon, which clearly becomes more intense close to Γ. The residual norms extracted setting side by side fitted curves and experimental data were then compared and it appeared that the best choice would either be that of a power-law or a Lorentzian, where the Lorentzian best fits experimental points for lower q's, and the power-law curve becomes more accurate when considering also higher values. This proceeding is illustrated in Fig. 4.2. Such arguments lead to the choice of the Lorentzian profile as the best candidate to model the Γ-peak.

This way, not only we decide which functional shape the Γ-peak has with respect to q, but we also extract a reasonable initial guess for its amplitude and width. As anticipated, we will then leave these two parameters free to change in following applications, in order to be able to account for differences in sample, experimental setup, ecc. Additionally, under the assumption that this background physically originates from an elastic scattering process, I added an energy-dependent compo-

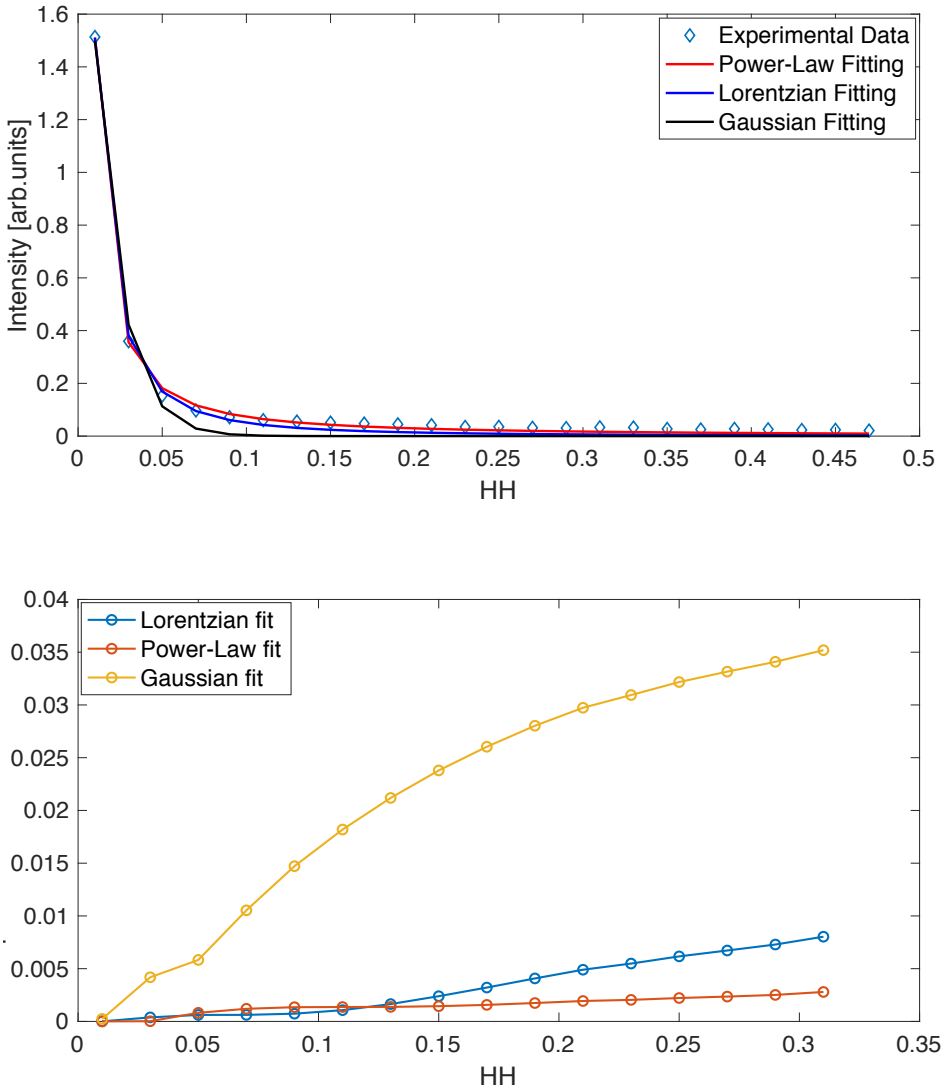

Figure 4.2: Top panel. Experimental data vs three different fitting curves, as indicated in the label. **Bottom panel.** Squared 2-norm of the residual after the fitting. Below q ≈ 0.13 r.l.u. the Lorentzian curve has the smallest residual.

nent to its expression, with Gaussian shape, and width set by the experimental resolution. Due to this variable-in-energy component the background elastic peak will need to be added to the CDF simulated intensity before proceeding with the numerical integration in the energy domain.

Moreover, besides adding a peak centered in Γ (fixed) with variable amplitude and width, I also added a rigid shift: an offset, constant both in temperature and momentum, equal for H0 and HH. The presence of this baseline is observed in q-scans from the measured signal at high q values (i.e. q ≈ 0.44 r.l.u.), which is still significant while both CDF-related intensity and lorentzian peak in Γ have vanished. This new element can be justified by taking into account all other phenomena, unrelated to

charge order excitations, which are still present in spectra and get integrated along with everything else when we perform the energy integration. This rigid up-shift allowed the routine to get much more accurate fitting results (the residual norm decreased by a factor $\sim 10^3$).

4.3 Structure of the routine

With respect to the analysis carried out in Chapt. 3, the function implemented for the fitting routine does not simulate CDF in the whole (H,K) plane. Experimental data is available as a set of two scans along H0 and HH so, instead of simulating the phenomenon in the whole 2D reciprocal lattice and then isolating the two cuts, we can run the simulation solely along H0 and HH in the first place. This drastically reduces computational cost and therefore allows us to run a much more accurate fitting. The whole code used for the fitting can be found in Appendix B.

As anticipated in 3.4, the behavior of experimental curves can not be faithfully reproduced leaving ω_0 constant in temperature. Based on those results, we argued that we might anticipate ω_0 to have a growing character with respect to temperature. In this context, indeed, we said that the T increase would lead to an increase in overall peak amplitude, but simultaneously the value of ω_0 would also rise, thus producing the opposite effect. The combination of these two is suspected to be causing the experimentally observed "squeeze" of intensity maxima in correspondence of CDF positions in reciprocal space. Moreover, we claimed that being $\omega_0 = \nu \cdot (\text{HWHM})^2$, the mild temperature dependence of FWHM observed in experimental curves would support the idea of ω_0 being $\omega_0(\text{T})$. For this reason I decided to leave ω_0 completely free to take different values as temperature changes. The same was done for γ as well, given that its effect is supposedly much more important at lower temperatures, where quantum effects become more relevant. This lets the fitting routine adjust their values in such a way that the residual is minimized, and it also gives us an expression of those parameters as a function of temperature, allowing us to interpret their physical meaning and suppose possible implications.

According to these considerations, the set of fitting parameters is actually a 9×13 matrix, where:

$PAR(1, T) = \omega_0(T)$

$PAR(2, 1) = \Omega$

$PAR(3,T) = \gamma(T)$

$PAR(4,1) = \nu$

$PAR(5,1) = Q_c$

$PAR(6,1) = \Gamma - peak^{(amplitude)}$

$PAR(7,1) = \Gamma - peak^{(FWHM)}$

$PAR(8,1) = C$ *(multiplying constant for the CDF intensity)*

$PAR(9,1) =$ *rigid shift*

Where all other parameters (besides ω_0 and γ) only use the first element of each row. Clearly this adds some computational cost and the routine will need to run more iterations to obtain a reliable result, but it allows us to achieve a much more realistic output, and adds fundamental physical insight to the values taken by ω_0 and γ. The MATLAB®, function used for the fit is *lsqcurvefit* which is a non-linear least square solver in the sense that it seeks coefficients PAR defining:

$$min\|SIMULATION(PAR,T) - EXP.DATA\|_2^2$$

through the default *trust-region-reflective* algorithm [56].

4.4 Fitting results

The results yielded by the fit performed on the BSCCO sample and a plot of Ω, ω_0 γ are shown respectively in Fig.s 4.3 and 4.4, whereas the equivalent for the YBCO sample can be found in Fig.s 4.5 and 4.6. Extracted parameters are indicated in Tab.s 4.7 and 4.8 together with their temperature dependence.

As one can observe from plots and tables of parameters, data relative to the YBCO sample was fitted without the peak in Γ. This is justified acknowledging that the measurement associated to the lowest momentum value was acquired at q $\approx$ 0.15 r.l.u. and, as it appears clear from the top-right plot in Fig. 4.5, the rise attributed to the Γ-peak only affects the first experimental point, being already very weakly contributing at q $\approx$ 0.17 r.l.u. This means that if we fit this data-set with the elastic peak as well, the fitting algorithm struggles to find appropriate values for its amplitude and width, and ends up running an unnecessarily large number of iterations to produce a result almost identical to that which we otherwise get without

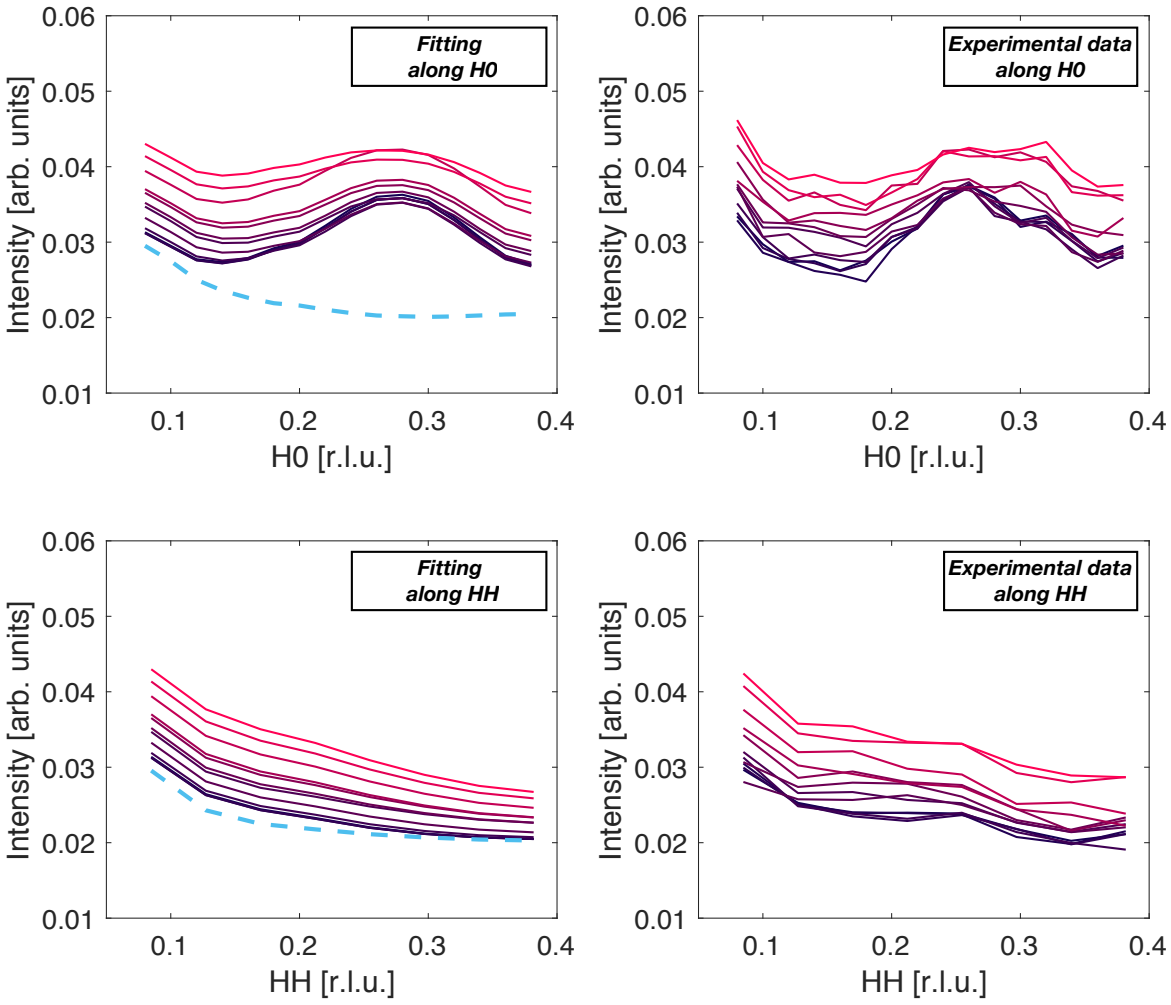

Figure 4.3: Fitting result and experimental data: BSCCO

Fitting results (left panels) and experimental values (right panels) are shown separately for H0 (top) and HH (bottom). Higher temperatures are parametrically indicated by lighter red curves. The light blue dotted line indicates the background, made up of the rigid shift and the lorentzian peak in Γ.

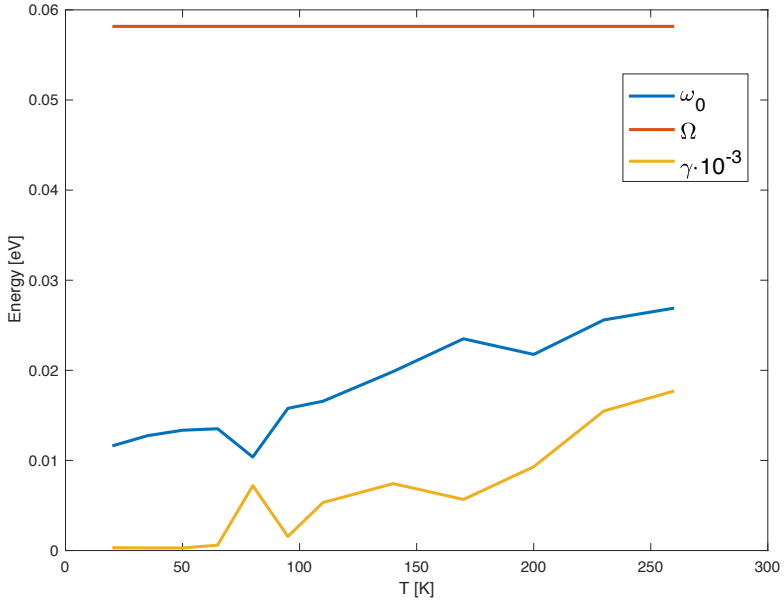

Figure 4.4: Extracted temperature dependence of ω_0 and γ, and value of Ω in BSCCO

Note that γ [1] has been multiplied by 10^{-3} in order to be able to plot it on the same scale.

considering the peak at all. Additionally, fitted parameters concerning the Γ-peak turn out to be affected by a huge error, as can be proven acting on initial guesses passed on to *lsqcurvefit*: upon wide swings (orders of magnitude) the fitted results always end up in the proximity of the guess itself, proving that the fitting function is not actually optimizing their values. Simply put, it *does not know* what to do with them. This is luckily not the case for the other parameters, which have more stringent constraints due to the role they play in determining the functional shape of $I^{sim}(q)$ curves. Conversely, as shown earlier in Fig. 3.6, on the BSCCO sample the lowest momentum value is $q \approx 0.08$ r.l.u., implying a much more prominent influence of the elastic peak in the scans, as it occurs in Fig. 4.3. As a consequence, the fitting routine fails in providing an accurate reproduction of data if the elastic rise close to Γ is neglected. The light blue dotted line in Fig. 4.3 visually displays the importance of the background with respect to the CDF fitted profiles.

Concerning ω_0 and Ω, Fig.s 4.4 and 4.6 reproduce their temperature dependence extracted from the fit. Ω is constant by construction and correctly falls at higher values with respect to ω_0, reasonably around few tens of meV. ω_0 confirms the suppositions made earlier regarding its possibility to be slightly growing with T, thus producing the "squeeze-effect" of intensity maxima in Q_c. ω_0 convincingly shows a quasi-linear behavior at high T, while slowing its descent at lower T. A rise in ω_0

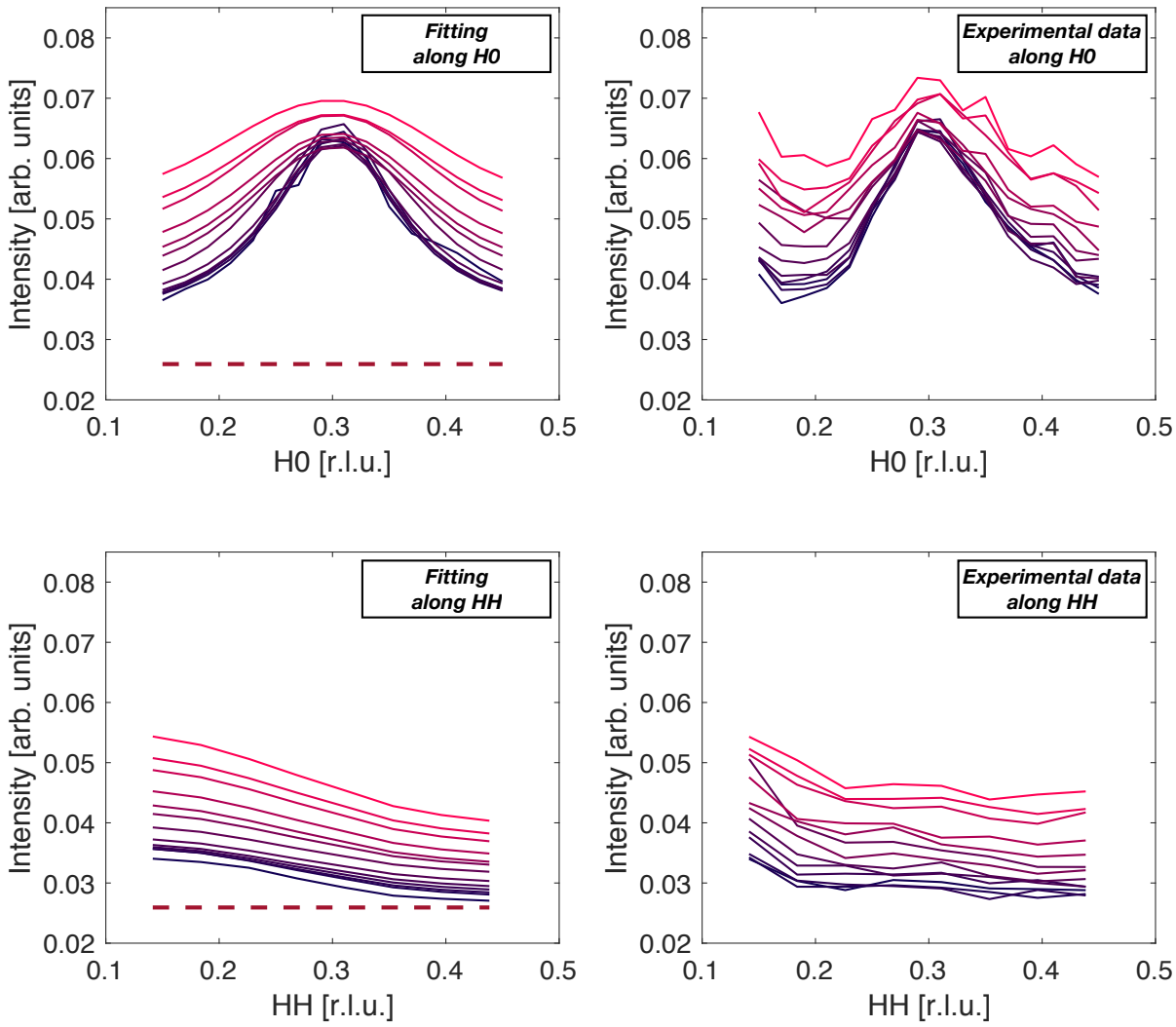

Figure 4.5: Fitting result and experimental data: YBCO

Fitting results (left panels) and experimental values (right panels) are shown separately for H0 (top) and HH (bottom). Higher temperatures are parametrically indicated by lighter red curves. The dark red dotted line indicates the background, made up only of a rigid shift.

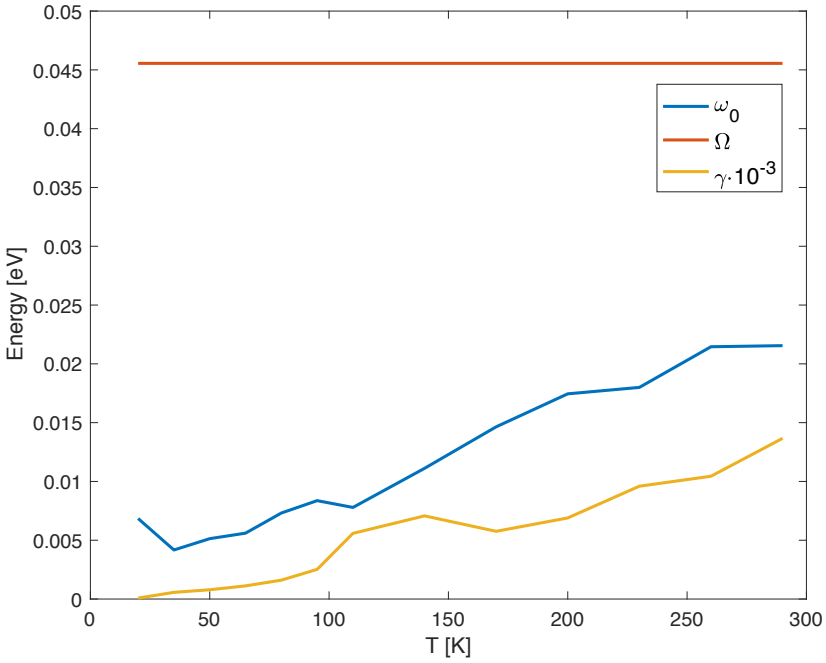

Figure 4.6: Extracted temperature dependence of ω_0 and γ, and value of Ω in YBCO

Note that γ [1] has been multiplied by 10^{-3} in order to be able to plot it on the same scale.

T *[K]*	20	35	50	65	80	95	110	140	170	200	230	260
ω_0 *[meV]*	11.6	12.7	13.3	13.5	10.4	15.8	16.6	19.9	23.5	21.7	25.6	26.9
Ω *[meV]*	58.2											
γ *[1]*	0.31	0.29	0.28	0.60	7.21	1.56	5.33	7.43	5.67	9.30	15.49	17.70
ν *$[eV/(r.l.u.)^2]$*	2.02											
Q_c *[r.l.u.]*	0.28											
$\Gamma - peak^{(amplitude)}$ *[arb.units]*	1.03											
$\Gamma - peak^{(FWHM)}$ *[r.l.u.]*	0.002											
C *[1]*	1.76											
Offset *[arb.units]*	0.02											

Figure 4.7: Extracted parameters in BSCCO.

ω_0 and γ are shown as a function of temperature, all other parameters are kept constant.

T *[K]*	20	35	50	65	80	95	110	140	170	200	230	260	290
ω_0 *[meV]*	6.85	4.17	5.13	5.60	7.31	8.37	7.79	11.11	14.64	17.45	17.99	21.45	21.55
Ω *[meV]*	45.55												
γ *[1]*	0.08	0.57	0.79	1.12	1.60	2.52	5.58	7.07	5.76	6.89	9.59	10.44	13.66
ν *[eV/(r.l.u.)^2]*	1.26												
Q_c *[r.l.u.]*	0.30												
C *[1]*	0.19												
Offset *[arb.units]*	0.026												

Figure 4.8: Extracted parameters in YBCO.
ω_0 and γ are shown as a function of temperature, all other parameters are kept constant.

also entails a mild increase in I(q)^{FWHM} due to the relation $\frac{\omega_0}{\nu} \approx (\text{HWHM})^2$ which, assuming fixed ν, connects values taken by ω_0 to the correlation length ξ of these charge density modulations since, as anticipated in Sect. 1.4, $\xi \sim \frac{1}{HWHM}$. This means that if $\omega_0 \xrightarrow[T\to 0]{} 0$ then also HWHM $\to 0$, meaning $\xi \to \infty$ [34]. A divergence of the correlation length of CDF at null temperature would imply the existence of a QCP, which would have strong implications on the nature of the pseudogap, making the locus of points T* (in phase diagrams) the dividing line between two actual different phases. For a more rigorous explanation of quantum phase transitions the reader can refer to Ref. [57]. Nevertheless, as anticipated in Sect. 1.4 and shown in Fig. 3.9, it appears (from spectra) that charge density fluctuations have finite energy even at very low temperatures, which would imply that they are indeed dynamical. This is at the core of the discussion regarding their difference with respect to "ordinary" stationary and critical charge density waves. It is quite encouraging to notice how this saturation effect on the value of ω_0 is confirmed by our results (see Fig.s 4.3, 4.5), even though we should note that, despite showing a reasonable overall behavior, ω_0 is quantitatively slightly too high with respect to values expected and observed from HR spectra. Nonetheless, we must always keep in mind that data used for the fitting was acquired with a resolution of approximately 60 meV, we then have to restrain ourselves from jumping to conclusions based on few meV differences, because they are actually quite indistinguishable with our resolution.

The value of the Landau damping γ is only relevant at low temperatures, in the "quantum regime" (let us say below T_c), so its fitted temperature dependence at high T should be disregarded. Actually, the role of γ is believed to manifest itself when superconductivity is quenched by strong magnetic fields, in which case it is believed to diverge as $T \to 0$; in this description, it would be the ratio $\frac{\omega_0}{\gamma}$, (instead of ω_0 alone), that would tend to zero. The divergence of γ would imply the presence of an *anomalous QCP*, being it related to the divergence of a temporal correlation length, rather than a spatial one (i.e. ξ) as it regularly occurs. This is the context behind the formulation of γ, which is currently purely theoretical and far from being demonstrated. I anyhow included it in the simulations for completeness.

It is encouraging to notice how fitted curves reproduce faithfully experimental ones, even in terms of particular features such as gaps between peaks at different temperatures and lines crossings (see Fig. 4.3), showing very little noise, except for the curve at 20 K in Fig. 4.5. Additionally, it is quite promising to see how the same function, running on the same algorithm, works very well on both samples which have a rather different peak shape and position. This is hopefully given by the fact that parameters taken into consideration by the model are enough to fully characterize the CDF phenomenon in all cuprate families, providing a fair degree of universality.

Lastly, I shall note that the fitting routine yielded these results free of constraints. Only initial guesses were given, as necessarily imposed by the nature of the solver, but no lower or upper boundaries were set beyond the necessity for all parameters to be positive amounts. This adds reliability to our results and hints at a fair level of robustness for the routine itself. On the other hand though, I noticed a significant dependence of quantitative results to initial guesses, meaning that even if fitted curves do not display pronounced variations, and still reflect experimental ones quite accurately, extracted values of ω_0, Ω, ν are affected to a noteworthy extent; nevertheless hardly ever falling outside reasonable intervals. This is likely given by the large number of fitting parameters required by our equations, which unlocks degrees of freedom for the solver and lowers confidence on each single result alone. In light of this, it might be interesting, were this possible, to ascertain some parameters through independent experiments to then fix them and run the simulation on fewer remaining ones.

The faithful and quantitative match, both in terms of temperature dependence and curve shape (in q-space) between fitted curves and modeled ones along both H0 and HH, is surely stimulating. It calls for more measurements to be made in order to

gain further physical insight into charge order excitations phenomena, and sustain the mutual beneficial interplay between theory and experiment through adjustments of models and the availability of higher resolution measurements.

Conclusions and future perspectives

These results have helped us shed light onto the phenomenon of short-ranged dynamical charge density fluctuations occurring in high-T_c superconducting cuprates. As highlighted, CDF are ubiquitous to all cuprate families and they occur in a broad area of these materials' phase diagrams. We studied them in slightly overdoped YBCO and BSCCO where they are predominant, in order to be able to isolate them as best as we could, this was deemed the best possible approach in order to find a suitable correspondence with the theoretical model at hand.

Experimental evidence proved that the existence of the broad peak associated to CDF in the 20 - 290 K temperature range is indisputable, thus underlying its inherent difference from well known medium-ranged static CDW, which tend to 'steal the spotlight' more often than not.

A comprehensive analysis of all parametric dependencies of the model underlined its potential suitability for the description of these charge excitations through promising qualitative matches, justifying further interest in developing quantitative relations.

Then, once a rigid offset and an elastic peak in Γ were added to the simulations, in order to account for unrelated phenomena entailing a non-negligible contribution to RIXS spectra, the theoretical model we used provided very encouraging results being able to reproduce the quasi-elastic intensity curves in momentum space along both H0 and HH to a very satisfying extent in the whole considered temperature range.

It remains unknown whether this match would be equally accurate if the fit was carried out over each single spectrum, thus also using all the information encoded in the energy-loss dimension. As indicated in Sect. 4.1, this would require the acquisition of ultra-high resolution spectra over a broad range of temperatures, and would inevitably lead to a considerable increase in computational cost. Nevertheless, were this technically possible, it would be an extremely interesting further development for this work. Additionally it should be reminded that this fitting relies on the assumption that RIXS experiments are able to directly access the charge suscepti-

bility $\chi(q,\omega)$ of cuprates, and this could be an approximation to be revised if more accurate expressions of RIXS cross sections came along for future elaborations.

Moreover, the very short correlation length of charge density modulations responsible for the BP -corroborated by our results on ω_0- pointed out that, as proposed by recent studies ([1], [26], [34]), they could very well be the key channel mediating the isotropic scattering of other mobile carriers. Indeed, as proposed in the mentioned Ref.s, the pervading presence of CDF above T^*, could suggest a relation of causality with the linear-in-T dependence of the resistivity of cuprates in their normal state, thus supposedly explaining the microscopic mechanism behind the *strange-metal* phenomenology. Actual first quantitative calculations carried out in this direction seem to go along well with observed behaviors and properties [26].

It is safe to say that the discovery of these novel charge density modulations has strong implications on our current understanding of the underlying mechanisms behind the behavior of several phases of cuprate high-T_c superconductors, although still highlighting our lack of a comprehensive knowledge on these topics. This work focused on providing evidence that a phenomenological description of CDF can be reliably instrumental to the formulation of theoretical models, which in turns can yield insightful predictions, enforcing a mutually beneficial relation between theory and experiment, in a virtuous loop.

A Appendix: computation times

In order to exemplify the decision-making process used for the practical implementation of equation 3.1 and of the fitting routine itself I present here a brief reasoning regarding computation times. All results presented in Chapt. 4 and **??** demanded no longer than a couple minutes to compute, even though I should note that time differences of up to a factor of two were noticed running the same program on different (but still quite performing) portable computers. This means that the issue of computation time is not a major concern in our case, even though few-minutes cutbacks can still ease the program development process significantly. This being said, it remains conceptually important not to write an overly redundant code. This brief reasoning also has the purpose of raising awareness on how small changes can heavily reflect on the final result in terms of duration. Particular prudence should be exercised in case, working on future developments, one decided to extend the fitting to the energy dimension as well, thus not only using quasi-elastic I(q) curves, but whole I(q,ω) spectra. In that case a whole new dimension would be added to parameters' space, certainly resulting in long delays.

Without moving on with such drastic changes, I hereby present the difference between two possible approaches for the simulation of intensity curves which are then passed on to the fitting routine. This passage will be iteratively called by the fitting algorithm *lsqcurvefit* until convergence is reached, and therefore needs to be as brief as possible. This function needs to return a matrix containing simulated intensity values as a function of vectors q and T with size equal to the experimental one, i.e. [length(H0) + length(HH)] $\times$ length(T). One possibility is thus to use command [Q, W, temp] = *meshgrid*(q,ω,T) to generate three-dimensional arrays Q, W, temp, and use them to create I(q, ω,T) directly as a 3D array itself, then integrating along dimension 2 (which, as indicated, corresponds to an energy integration) one ends up with I^{mesh}(q,T). The other possibility is using a loop-based function which, at each k^{th} iteration, computes two-dimensional I^{loop}(q,ω,T(k)), integrates along dimension 2, thus resulting in a vector, which can then be saved as a column in I^{loop}(q,T(k)). At iteration number k = *length*(T) a full I^{loop}(q,T) will be ready to be returned to the nonlinear solver. Each discussed procedure accounts for one single iteration relatively to the fitting.

This two approaches clearly result in the same output, but they do so with a quite significant duration difference. I calculated the computation time of each method as a function of the length n of q and ω defining the sizes of the simulation which, in this case, are kept equal. Figure A.1 shows the result, underlying the non equivalence of the two approaches.

Performing a polynomial fitting of the two curves, we find that computation times grow quasi-quadratically in both cases, with functional shapes:

$$t_{mesh}(n) \approx 5.57 \cdot 10^{-7} n^{2.254}$$

$$t_{loop}(n) \approx 3.52 \cdot 10^{-7} n^{2.254}$$

With the loop-based algorithm outperforming the meshgrid-based one. This was indeed the approach chosen to produce the simulations in this thesis. Furthermore, considering that the routine discussed in Chapt. **??** and shown in Appendix B works with n = 90, I calculated the average gain over many iterations as:

$$t^{\%}_{gain} \equiv \frac{t_{mesh}(90) - t_{loop}(90)}{t_{mesh}(90)} \approx 37\%$$

which is certainly a significant improvement considering that this difference will likely be reflected onto the total time required by the routine to carry out the fitting.

As I said, this is only one of the multiple adjustments and refinements that can be put in place, and it is surely not the only factor contributing to the overall computation time. One possibility moving forward could be generating the momentum dependent part of the simulation only along experimental H0 and HH, instead of using a theoretical q consisting of 90 points and then extracting only those corresponding to H0 and HH in the end. n $\approx 10^2$ could still be used for ω to guarantee a reliable result from the numerical integration.

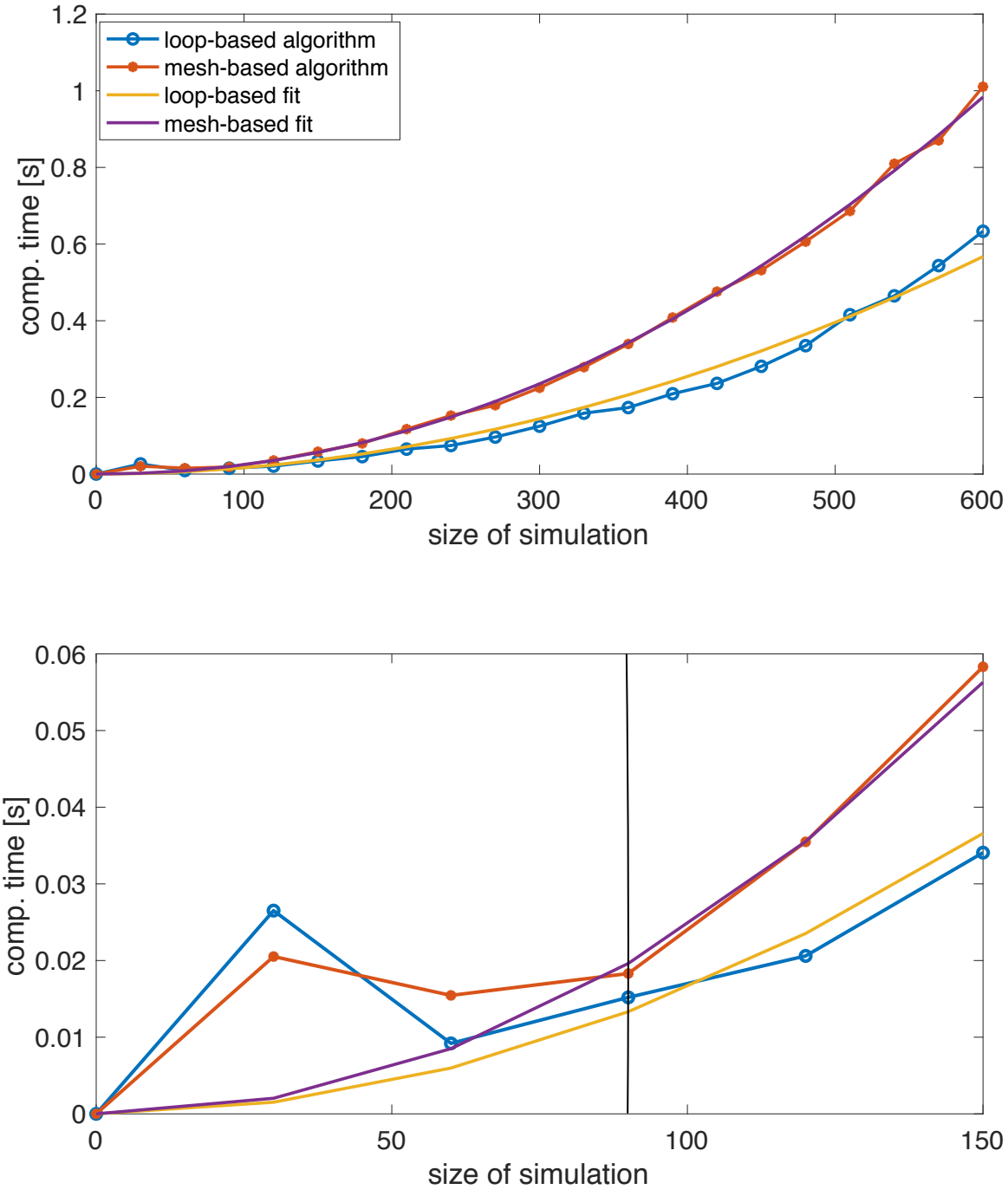

Figure A.1: Computation time analysis.

Top panel. Duration of each scheme plotted as a function of the dimension of q and ω. Yellow and purple lines show polynomial fittings.

Bottom panel. Same as above but zoomed in on the first few points, the black line cuts plots at n = 90, which is the dimension used for the fit on BSCCO.

B Appendix: fitting code (BSCCO)

```
clear
close all
clc


% "sizee" defines the dimension "n = 2*sizee" for the
   simulations
sizee = 45 ;

% Integration window (energy)
w_min = -0.1 ;
w_max = 0.035 ;


%% Import data

% Define momentum range to be used
% maximum range is h0=0.15-0.45 and hh=0.14-0.43

h0min = 0.08 ;
h0max = 0.45 ;

hhmin = h0min ;
hhmax = h0max ;

% Import all
I_hh_imported = importfile_hh_5("/Users/pietrocamisa/
   Desktop/Tesi Magistrale/Dati Bi2212/Integrali Bi2212.
   xlsx", "HH", 2, 9);
I_h0_imported = importfile_h0_5("/Users/pietrocamisa/
   Desktop/Tesi Magistrale/Dati Bi2212/Integrali Bi2212.
   xlsx", "H0", 2, 17);

T_v = [20,35,50,65,80,95,110,140,170,200,230,260] ;

h0 = I_h0_imported(:,1) ;
hh = I_hh_imported(:,1) ;

```

```
h0i = find( abs(h0-h0min) == min(abs(h0-h0min)) ) ;
h0e = find( abs(h0-h0max) == min(abs(h0-h0max)) ) ;

hhi = find( abs(hh-hhmin) == min(abs(hh-hhmin)) ) ;
hhe = find( abs(hh-hhmax) == min(abs(hh-hhmax)) ) ;

% Select only experimental data in the specified range
h0 = I_h0_imported(h0i:h0e,1) ;
I_h0_exp = I_h0_imported(h0i:h0e,2:end) ;

hh = I_hh_imported(hhi:hhe,1) ;
I_hh_exp = I_hh_imported(hhi:hhe,2:end) ;

clear I_h0_imported
clear I_hh_imported

% Define matrix of experimental data
I_exp = [I_h0_exp; I_hh_exp] ;

%% Simulation of CDF

fun = @(PAR,T_v) Simulation_5_loop(PAR,T_v,sizee,h0,hh,
   w_min,w_max) ;

%% Fit

tic

f_eval = 15e3 ;
f_iter = 5000 ;
f_tol = eps ;
f_step = eps ;
f_optimality = eps ;

% Initial guess
PAR0 = [12.5*ones(1,length(T_v))        ; ... % w0
        35*ones(1,length(T_v))          ; ... % OMEGA
        1*ones(1,length(T_v))           ; ... % gamma
        1.4*ones(1,length(T_v))         ; ... % ni
        0.3*ones(1,length(T_v))         ; ... % qc
        1*ones(1,length(T_v))           ; ... % amplitude
           GP
        0.08*ones(1,length(T_v))        ; ... % fwhm_gp
        1.2*ones(1,length(T_v))         ; ... % C
```

```
        0.015*ones(1,length(T_v))       ];    % offset

% Lower boundary for positivity
lb = [  0*ones(1,length(T_v))           ; ... % w0
        0*ones(1,length(T_v))           ; ... % OMEGA
        0*ones(1,length(T_v))           ; ... % gamma
        0*ones(1,length(T_v))           ; ... % ni
        0*ones(1,length(T_v))           ; ... % qc
        0*ones(1,length(T_v))           ; ... % amplitude
           GP
        0*ones(1,length(T_v))           ; ... % fwhm_gp
        0*ones(1,length(T_v))           ; ... % C
        0*ones(1,length(T_v))          ];    % offset

options = optimoptions('lsqcurvefit', 'FunctionTolerance'
   ,f_tol) ;
options.MaxFunctionEvaluations = f_eval ;
options.MaxIterations = f_iter ;
options.StepTolerance = f_step ;
options.OptimalityTolerance = f_optimality ;

[PAR,resnorm,residual,exitflag,output,lambda,J] =
   lsqcurvefit(fun,PAR0,T_v,I_exp,lb,[],options) ;

t = toc ;

%% Plots

my_plot_5(PAR,T_v,sizee,h0,hh,I_exp,w_min,w_max) ;

fprintf('\nSquared norm of the residual : %d\n\n',resnorm)
    ;
fprintf('\nComputation time : %d\n\n',t) ;
```

Listing B.1: Main script

```
function I_h0_imported = importfile_h0_5(workbookFile,
   sheetName, startRow, endRow)
%% Input handling

% If no sheet is specified, read first sheet
if nargin == 1 || isempty(sheetName)
    sheetName = 1;
end

```

```
% If row start and end points are not specified, define
   defaults
if nargin <= 3
    startRow = 2;
    endRow = 17;
end

%% Setup the Import Options
opts = spreadsheetImportOptions("NumVariables", 13);

% Specify sheet and range
opts.Sheet = sheetName;
opts.DataRange = "A" + startRow(1) + ":M" + endRow(1);

% Specify column names and types
opts.VariableNames = ["VarName1", "VarName2", "VarName3",
   "VarName4", "VarName5", "VarName6", "VarName7", "
   VarName8", "VarName9", "VarName10", "VarName11", "
   VarName12", "VarName13"];
opts.VariableTypes = ["double", "double", "double", "
   double", "double", "double", "double", "double", "
   double", "double", "double", "double", "double"];

% Import the data
I_h0_imported = readtable(workbookFile, opts, "UseExcel",
   false);

for idx = 2:length(startRow)
    opts.DataRange = "A" + startRow(idx) + ":M" + endRow(
       idx);
    tb = readtable(workbookFile, opts, "UseExcel", false);
    I_h0_imported = [I_h0_imported; tb]; %#ok<AGROW>
end

%% Convert to output type
I_h0_imported = table2array(I_h0_imported);
end
```

Listing B.2: Import experimental data along H0 from spreadsheet in Fig. 3.8.

```
function I_hh_imported = importfile_hh_5(workbookFile,
   sheetName, startRow, endRow)
%% Input handling

% If no sheet is specified, read first sheet
```

```
if nargin == 1 || isempty(sheetName)
    sheetName = 1;
end

% If row start and end points are not specified, define
   defaults
if nargin <= 3
    startRow = 2;
    endRow = 9;
end

%% Setup the Import Options
opts = spreadsheetImportOptions("NumVariables", 13);

% Specify sheet and range
opts.Sheet = sheetName;
opts.DataRange = "A" + startRow(1) + ":M" + endRow(1);

% Specify column names and types
opts.VariableNames = ["VarName1", "VarName2", "VarName3",
   "VarName4", "VarName5", "VarName6", "VarName7", "
   VarName8", "VarName9", "VarName10", "VarName11", "
   VarName12", "VarName13"];
opts.VariableTypes = ["double", "double", "double", "
   double", "double", "double", "double", "double", "
   double", "double", "double", "double", "double"];

% Import the data
I_hh_imported = readtable(workbookFile, opts, "UseExcel",
   false);

for idx = 2:length(startRow)
    opts.DataRange = "A" + startRow(idx) + ":M" + endRow(
       idx);
    tb = readtable(workbookFile, opts, "UseExcel", false);
    I_hh_imported = [I_hh_imported; tb]; %#ok<AGROW>
end

%% Convert to output type
I_hh_imported = table2array(I_hh_imported);
end
```

Listing B.3: Import experimental data along HH from spreadsheet in Fig. 3.8.

```
function I_th = Simulation_5_loop(PAR,T_v,sizee,h0,hh,
   w_min,w_max)

I_th_h0 = zeros(length(h0),length(T_v)) ;
I_th_hh = zeros(length(hh),length(T_v)) ;

% Loop in temperature: T_v stands for T_vector
for i = 1 : length(T_v)

e = 1.60217662e-19 ;                                % [C]
   electron charge
kb = 1.38064852e-23 ;                               % [(m^2kg)
   /s^2K] Boltz const

n = 2*sizee ;

q = linspace(-0.5,0.5,n) ;
w = linspace(-0.2,0.2,n)' ;
[Q,W] = meshgrid(q,-w) ; % "-w" because the equations we
   use consider a positive sign for antistokes

h0_ = zeros(1,length(h0)) ;
hh_ = zeros(1,length(hh)) ;
intensity_h0 = zeros(length(h0),1) ;
intensity_hh = zeros(length(hh),1) ;

% Energy resolution
coeff = 2*sqrt(2*log(2)) ;
fwhm_w = 0.06 ; % [eV]
sig_w = fwhm_w/(coeff) ;
resol = 1/(sig_w*sqrt(2*pi)) * exp(-W.^2 / (2*(sig_w)^2))
   ;

w0 = PAR(1,T_v == T_v(i))/1e3 ;
OMEGA = PAR(2,1)/1e3 ;
gamma = PAR(3, T_v == T_v(i)) ;
ni = PAR(4,1) ;
qc = PAR(5,1) ;

% Gamma peak
amp_GP = PAR(6,1)/1e3 ;
fwhm_GP = PAR(7,1) ;
GP = (amp_GP/pi) * ((fwhm_GP/2)./(Q.^2 + (fwhm_GP/2).^2))
   .* resol ;
```

```
C = PAR(8,1)/1e7 ;

eta1_h0 = (4 - 2*cos(2*pi*(Q-qc)) - 2*cos(2*pi*(0))) / (2*pi)^2 ;
eta2_h0 = (4 - 2*cos(2*pi*(Q+qc)) - 2*cos(2*pi*(0))) / (2*pi)^2 ;
eta3_h0 = (4 - 2*cos(2*pi*(Q)) - 2*cos(2*pi*(0+qc))) / (2*pi)^2 ;
eta4_h0 = (4 - 2*cos(2*pi*(Q)) - 2*cos(2*pi*(0-qc))) / (2*pi)^2 ;

eta1_hh = (4 - 2*cos(2*pi*(Q-qc)) - 2*cos(2*pi*(Q))) / (2*pi)^2 ;
eta2_hh = (4 - 2*cos(2*pi*(Q+qc)) - 2*cos(2*pi*(Q))) / (2*pi)^2 ;
eta3_hh = (4 - 2*cos(2*pi*(Q)) - 2*cos(2*pi*(Q+qc))) / (2*pi)^2 ;
eta4_hh = (4 - 2*cos(2*pi*(Q)) - 2*cos(2*pi*(Q-qc))) / (2*pi)^2 ;


D_h0 =                ( w0 + ni*eta1_h0 - 1i*W*gamma - W.^2/OMEGA ).^-1 + ...
                      ( w0 + ni*eta2_h0 - 1i*W*gamma - W.^2/OMEGA ).^-1 + ...
                      ( w0 + ni*eta3_h0 - 1i*W*gamma - W.^2/OMEGA ).^-1 + ...
                      ( w0 + ni*eta4_h0 - 1i*W*gamma - W.^2/OMEGA ).^-1 ;

D_hh =                ( w0 + ni*eta1_hh - 1i*W*gamma - W.^2/OMEGA ).^-1 + ...
                      ( w0 + ni*eta2_hh - 1i*W*gamma - W.^2/OMEGA ).^-1 + ...
                      ( w0 + ni*eta3_hh - 1i*W*gamma - W.^2/OMEGA ).^-1 + ...
                      ( w0 + ni*eta4_hh - 1i*W*gamma - W.^2/OMEGA ).^-1 ;

D_i_h0 = imag(D_h0) ;
D_i_hh = imag(D_hh) ;

b = (exp((e*W)/(kb*T_v(i))) - 1).^-1 ;

```

```
I_h0 = D_i_h0 .* b ;
I_hh = D_i_hh .* b ;

I_h0_conv = conv2(resol(:,1),1,I_h0,'same') ;
I_hh_conv = conv2(resol(:,1),1,I_hh,'same') ;

I_h0_conv = C * I_h0_conv + GP ;
I_hh_conv = C * I_hh_conv + GP ;

% Energy integration
w_index_max = find(abs(w-w_max) == min(abs(w-w_max))) ;
w_index_min = find(abs(w-w_min) == min(abs(w-w_min))) ;

scan_h0 = trapz(I_h0_conv(w_index_min:w_index_max,:)) ;
scan_hh = trapz(I_hh_conv(w_index_min:w_index_max,:)) ;

for j = 1 : length(h0)  % Extracts only points of q
   corresponding to experimental values: h0

        [~,h0_(j)] = find( abs(q-h0(j)) == min(abs(q-h0(j)
           )) ) ;
        intensity_h0(j) = scan_h0(h0_(j)) ;

     if j <= length(hh) % Extracts only points of q
        corresponding to experimental values: hh

        [~,hh_(j)] = find( abs(q-hh(j)) == min(abs(q-hh(j)
           )) ) ;
        intensity_hh(j) = scan_hh(hh_(j)) ;

     end
end

I_th_h0(:,i) = intensity_h0 ;
I_th_hh(:,i) = intensity_hh ;

end

I_th = PAR(9,1) + [I_th_h0 ; I_th_hh] ;

end
```

Listing B.4: Generation of the simulated intensity matrix

```
function I_th_sub = Simulation_5_sub(PAR,T_v,sizee,h0,hh,
   w_min,w_max)

I_th_h0 = zeros(length(h0),length(T_v)) ;
I_th_hh = zeros(length(hh),length(T_v)) ;

for i = 1 : length(T_v)

e = 1.60217662e-19 ;                                % [C]
   electron charge
kb = 1.38064852e-23 ;                               % [(m^2kg)
   /s^2K] Boltz const

n = 2*sizee ;

q = linspace(-0.5,0.5,n) ;
w = linspace(-0.2,0.2,n)' ;
[Q,W] = meshgrid(q,-w) ;

h0_ = zeros(1,length(h0)) ;
hh_ = zeros(1,length(hh)) ;
intensity_h0 = zeros(length(h0),1) ;
intensity_hh = zeros(length(hh),1) ;

% Energy resolution
coeff = 2*sqrt(2*log(2)) ;
fwhm_w = 0.05 ;                                             % [eV]
sig_w = fwhm_w/(coeff) ;
resol = 1/(sig_w*sqrt(2*pi)) * exp(-W.^2 / (2*(sig_w)^2))
   ;

w0 = PAR(1,T_v == T_v(i))/1e3 ;
OMEGA = PAR(2,1)/1e3 ;
gamma = PAR(3, T_v == T_v(i)) ;
ni = PAR(4,1) ;
qc = PAR(5,1) ;
C = PAR(8,1)/1e7 ;

eta1_h0 = (4 - 2*cos(2*pi*(Q-qc)) - 2*cos(2*pi*(0))) / (2*
   pi)^2 ;
eta2_h0 = (4 - 2*cos(2*pi*(Q+qc)) - 2*cos(2*pi*(0))) / (2*
   pi)^2 ;
eta3_h0 = (4 - 2*cos(2*pi*(Q)) - 2*cos(2*pi*(0+qc))) / (2*
   pi)^2 ;
```

```
eta4_h0 = (4 - 2*cos(2*pi*(Q)) - 2*cos(2*pi*(0-qc))) / (2*
   pi)^2 ;

eta1_hh = (4 - 2*cos(2*pi*(Q-qc)) - 2*cos(2*pi*(Q))) / (2*
   pi)^2 ;
eta2_hh = (4 - 2*cos(2*pi*(Q+qc)) - 2*cos(2*pi*(Q))) / (2*
   pi)^2 ;
eta3_hh = (4 - 2*cos(2*pi*(Q)) - 2*cos(2*pi*(Q+qc))) / (2*
   pi)^2 ;
eta4_hh = (4 - 2*cos(2*pi*(Q)) - 2*cos(2*pi*(Q-qc))) / (2*
   pi)^2 ;


D_h0 =               ( w0 + ni*eta1_h0 - 1i*W*gamma - W.^2/
   OMEGA ).^-1 + ...
                     ( w0 + ni*eta2_h0 - 1i*W*gamma - W.^2/
                        OMEGA ).^-1 + ...
                     ( w0 + ni*eta3_h0 - 1i*W*gamma - W.^2/
                        OMEGA ).^-1 + ...
                     ( w0 + ni*eta4_h0 - 1i*W*gamma - W.^2/
                        OMEGA ).^-1 ;

D_hh =               ( w0 + ni*eta1_hh - 1i*W*gamma - W.^2/
   OMEGA ).^-1 + ...
                     ( w0 + ni*eta2_hh - 1i*W*gamma - W.^2/
                        OMEGA ).^-1 + ...
                     ( w0 + ni*eta3_hh - 1i*W*gamma - W.^2/
                        OMEGA ).^-1 + ...
                     ( w0 + ni*eta4_hh - 1i*W*gamma - W.^2/
                        OMEGA ).^-1 ;

D_i_h0 = imag(D_h0) ;
D_i_hh = imag(D_hh) ;

b = (exp((e*W)/(kb*T_v(i))) - 1).^-1 ;

I_h0 = D_i_h0 .* b ;
I_hh = D_i_hh .* b ;

I_h0_conv = conv2(resol(:,1),1,I_h0,'same') ;
I_hh_conv = conv2(resol(:,1),1,I_hh,'same') ;

I_h0_conv = C * I_h0_conv ;
I_hh_conv = C * I_hh_conv ;
```

```
70
71  % Energy integration
72  w_index_max = find(abs(w-w_max) == min(abs(w-w_max))) ;
73  w_index_min = find(abs(w-w_min) == min(abs(w-w_min))) ;
74
75  scan_h0 = trapz(I_h0_conv(w_index_min:w_index_max,:)) ;
76  scan_hh = trapz(I_hh_conv(w_index_min:w_index_max,:)) ;
77
78  for j = 1 : length(h0)
79
80          [~,h0_(j)] = find( abs(q-h0(j)) == min(abs(q-h0(j)
               )) ) ;
81          intensity_h0(j) = scan_h0(h0_(j)) ;
82
83       if j <= length(hh)
84
85          [~,hh_(j)] = find( abs(q-hh(j)) == min(abs(q-hh(j)
               )) ) ;
86          intensity_hh(j) = scan_hh(hh_(j)) ;
87
88       end
89  end
90
91  I_th_h0(:,i) = intensity_h0 ;
92  I_th_hh(:,i) = intensity_hh ;
93
94  end
95
96  I_th_sub = PAR(9,1) + [I_th_h0 ; I_th_hh] ;
97
98  end
```

Listing B.5: Generate intensity matrix without background for subtraction

```
1
2  function my_plot_5(PAR,T_v,sizee,h0,hh,I_exp,w_min,w_max)
3
4  % Return the simulation evaluated with the parameters
       extracted from the fit
5  I_th = Simulation_5_loop(PAR,T_v,sizee,h0,hh,w_min,w_max)
       ;
6
7  fontsize = 13 ;
8  ylimit = [0.01, 0.06] ;
9  xlimit = [0.05, 0.4] ;
```

```
10
11 figure('name','Simulations vs Data')
12
13 % Fitting along h0
14 subplot(2,2,1)
15 for i = 1 : length(T_v)
16     hold on; box on
17     plot(h0,I_th(1:length(h0),i),'linewidth',1,'Color', [
       T_v(i)/T_v(end) 0 0.33 ] ) ;
18
19 end
20 if size(PAR,1) > 7
21     I_th_sub = Simulation_5_sub(PAR,T_v,sizee,h0,hh,w_min,
       w_max) ;
22     BGR = I_th(1:length(h0),1)-I_th_sub(1:length(h0),1)+
       PAR(9,1) ;
23     plot(h0,BGR,'--','linewidth',2) ;
24 else
25     plot(h0,PAR(7,1)*ones(length(h0),1),'--','linewidth'
       ,2) ;
26 end
27 hold off
28 xlabel('H0 [r.l.u.]') ;
29 ylabel('Intensity [arb. units]') ;
30 xlim(xlimit) ;
31 ylim(ylimit) ;
32 set(gca, 'FontSize', fontsize) ;
33
34
35 % Experimental data along h0
36 subplot(2,2,2)
37 for i = 1 : length(T_v)
38     hold on; box on
39     plot(h0,I_exp(1:length(h0),i),'linewidth',1,'Color', [
       T_v(i)/T_v(end) 0 0.33 ] ) ;
40 end
41 hold off
42 xlabel('H0 [r.l.u.]') ;
43 ylabel('Intensity [arb. units]') ;
44 xlim(xlimit) ;
45 ylim(ylimit) ;
46 set(gca, 'FontSize', fontsize) ;
47
48
```

```
% Fitting along hh
subplot(2,2,3)
for i = 1 : length(T_v)
    hold on; box on
    plot(hh,I_th(length(h0)+1:end,i),'linewidth',1,'Color'
       , [T_v(i)/T_v(end) 0 0.33 ] ) ;

end
if size(PAR,1) > 7
    I_th_sub = Simulation_5_sub(PAR,T_v,sizee,h0,hh,w_min,
       w_max) ;
    BGR = I_th(1+length(h0):end,1)-I_th_sub(1+length(h0):
       end,1)+PAR(9,1) ;
    plot(hh,BGR,'--','linewidth',2) ;
else
    plot(hh,PAR(7,1)*ones(length(hh),1),'--','linewidth'
       ,2) ;
end
hold off
xlabel('HH [r.l.u.]') ;
ylabel('Intensity [arb. units]') ;
xlim(xlimit) ;
ylim(ylimit) ;
set(gca, 'FontSize', fontsize) ;


% Experimental data along hh
subplot(2,2,4)
for i = 1 : length(T_v)
    hold on; box on
    plot(hh,I_exp(length(h0)+1:end,i),'linewidth',1,'Color
       ', [T_v(i)/T_v(end) 0 0.33 ] ) ;

end
hold off
xlabel('HH [r.l.u.]') ;
ylabel('Intensity [arb. units]') ;
xlim(xlimit) ;
ylim(ylimit) ;
set(gca, 'FontSize', fontsize) ;

% omega_0 versus OMEGA_BAR
w0 = PAR(1,:)*1e-3 ;
OMEGA = PAR(2,1)*1e-3*ones(1,length(T_v)) ;
```

```
gamma = PAR(3,:)*1e-3 ;

figure('name','Omega')
plot(T_v,w0,'linewidth',2) ;
hold on; box on
plot(T_v,OMEGA,'linewidth',2) ;
plot(T_v,gamma,'linewidth',2) ;
xlabel('T [K]') ;
ylabel('Energy [eV]') ;
legend('\omega_0','\Omega','\gamma\cdot10^{-3}','FontSize'
   ,15) ;
hold off

end
```

Listing B.6: Produce plots displayed in figures 4.3 and 4.4

References

[1] R. Arpaia et al. "Dynamical charge density fluctuations pervading the phase diagram of a Cu-based high-Tc superconductor". In: *Science* 365.6456 (Aug. 2019), pp. 906–910. DOI: 10.1126/science.aav1315. URL: https://doi.org/10.1126/science.aav1315.

[2] G. Ghiringhelli et al. "Long-Range Incommensurate Charge Fluctuations in $(Y, Nd)Ba_2Cu_3O_{6+x}$". In: *Science* 337.6096 (July 2012), pp. 821–825. DOI: 10.1126/science.1223532. URL: https://doi.org/10.1126/science.1223532.

[3] R. O. Jones. "Density functional theory: Its origins, rise to prominence, and future". In: *Reviews of Modern Physics* 87.3 (Aug. 2015), pp. 897–923. DOI: 10.1103/revmodphys.87.897. URL: https://doi.org/10.1103/revmodphys.87.897.

[4] J. Zaanen, G. A. Sawatzky, and J. W. Allen. "Band gaps and electronic structure of transition-metal compounds". In: *Physical Review Letters* 55.4 (July 1985), pp. 418–421. DOI: 10.1103/physrevlett.55.418. URL: https://doi.org/10.1103/physrevlett.55.418.

[5] Nikolay Plakida. *High-Temperature Cuprate Superconductors*. Springer Berlin Heidelberg, 2010. DOI: 10.1007/978-3-642-12633-8. URL: https://doi.org/10.1007/978-3-642-12633-8.

[6] Maddury Somayazulu et al. "Evidence for Superconductivity above 260 K in Lanthanum Superhydride at Megabar Pressures". In: *Physical Review Letters* 122.2 (Jan. 2019). DOI: 10.1103/physrevlett.122.027001. URL: https://doi.org/10.1103/physrevlett.122.027001.

[7] Pia Jensen Ray. "Master's thesis: Structural investigation of La(2-x)Sr(x)CuO(4+y) - Following staging as a function of temperature". In: (2016). DOI: 10.6084/M9.FIGSHARE.2075680.V2.

[8] Lillian Hoddeson. "John Bardeen and the BCS Theory of Superconductivity". In: *MRS Bulletin* 24.1 (Jan. 1999), pp. 50–55. DOI: 10.1557/s0883769400051745. URL: https://doi.org/10.1557/s0883769400051745.

[9] B. Keimer et al. *High Temperature Superconductivity in the Cuprates*. 2014. arXiv: 1409.4673 [cond-mat.supr-con].

[10] J. G. Bednorz and K. A. Muller. "Possible high-T_c superconductivity in the Ba-La-Cu-O system". In: *Zeitschrift for Physik B Condensed Matter* 64.2 (June 1986), pp. 189–193. DOI: 10.1007/bf01303701. URL: https://doi.org/10.1007/bf01303701.

[11] C. C. Tsuei and J. R. Kirtley. "Pairing symmetry in cuprate superconductors". In: *Reviews of Modern Physics* 72.4 (Oct. 2000), pp. 969–1016. DOI: 10.1103/revmodphys.72.969. URL: https://doi.org/10.1103/revmodphys.72.969.

[12] Riccardo Comin and Andrea Damascelli. "Resonant x-ray scattering studies of charge order in cuprates". In: (2015). DOI: 10.1146/annurev-conmatphys-031115-011401. eprint: arXiv:1509.03313.

[13] Catherine E. Housecroft and Alan G. Sharpe. *Inorganic Chemistry*. Pearson Education Limited, 2001.

[14] A.J. Leggett. "Cuprate superconductivity". In: *Quantum Liquids*. Oxford University Press, Sept. 2006, pp. 283–348. DOI: 10.1093/acprof:oso/9780198526438.003.0007. URL: https://doi.org/10.1093/acprof:oso/9780198526438.003.0007.

[15] Marco Moretti Sala. "Magnetic and Inelastic soft x-rays scattering". PhD thesis. Politecnico di Milano, 2000.

[16] N. Barišić et al. "Universal sheet resistance and revised phase diagram of the cuprate high-temperature superconductors". In: *Proceedings of the National Academy of Sciences of the United States of America* 110 (July 2013). DOI: 10.1073/pnas.1301989110.

[17] Greta Dallea. "Collective excitations in high temperature superconducting cuprates studied by resonant inelastic x-rays scattering". PhD thesis. Politecnico di Milano, 2016.

[18] Luuk J. P. Ament et al. "Resonant inelastic x-ray scattering studies of elementary excitations". In: *Reviews of Modern Physics* 83.2 (June 2011), pp. 705–767. DOI: 10.1103/revmodphys.83.705. URL: https://doi.org/10.1103/revmodphys.83.705.

[19] S. Blundell. *Magnetism in Condensed Matter*. Oxford Master Series in Condensed Matter Physics. OUP Oxford, 2001. ISBN: 9780198505914. URL: https://books.google.it/books?id=OGhGmgEACAAJ.

[20] Lucio Braicovich and Giacomo Ghiringhelli. "High-resolution resonant inelastic soft X-ray scattering (RIXS) A new spectroscopy for the study of charge, orbital, spin and lattice excitations in materials with strong electron correlation". In: *Il Nuovo Saggiatore* 35 (Oct. 2019).

[21] M. K. Wu et al. "Superconductivity at 93 K in a new mixed-phase Y-Ba-Cu-O compound system at ambient pressure". In: *Physical Review Letters* 58.9 (Mar. 1987), pp. 908–910. DOI: 10.1103/physrevlett.58.908. URL: https://doi.org/10.1103/physrevlett.58.908.

[22] Reza Baghdadi et al. "Toward $YBa_2Cu_3O7\delta$ Nanoscale Structures for Hybrid Devices". In: *IEEE Transactions on Applied Superconductivity* 25.3 (June 2015), pp. 1–4. DOI: 10.1109/tasc.2014.2362991. URL: https://doi.org/10.1109/tasc.2014.2362991.

[23] Riccardo Arpaia et al. "Probing the phase diagram of cuprates with $YBa_2Cu_3O_{7-\delta}$ thin films and nanowires". In: *Physical Review Materials* 2.2 (Feb. 2018). DOI: 10.1103/physrevmaterials.2.024804. URL: https://doi.org/10.1103/physrevmaterials.2.024804.

[24] J. E. Hoffman. "A Four Unit Cell Periodic Pattern of Quasi-Particle States Surrounding Vortex Cores in $Bi_2Sr_2CaCu_2O_{8+\delta}$". In: *Science* 295.5554 (Jan. 2002), pp. 466–469. DOI: 10.1126/science.1066974. URL: https://doi.org/10.1126/science.1066974.

[25] D. E. Moncton, J. D. Axe, and F. J. DiSalvo. "Neutron scattering study of the charge-density wave transitions in 2H-$TaSe_2$ and 2H-$NbSe_2$". In: *Physical Review B* 16.2 (July 1977), pp. 801–819. DOI: 10.1103/physrevb.16.801. URL: https://doi.org/10.1103/physrevb.16.801.

[26] Carlo Di Castro. "Revival of Charge Density Waves and Charge Density Fluctuations in Cuprate High-Temperature Superconductors". In: *Condensed Matter* 5.4 (2020). ISSN: 2410-3896. DOI: 10.3390/condmat5040070. URL: https://www.mdpi.com/2410-3896/5/4/70.

[27] Tao Wu et al. "Incipient charge order observed by NMR in the normal state of $YBa_2Cu_3O_y$". In: *Nature Communications* 6.1 (Mar. 2015). ISSN: 2041-1723. DOI: 10.1038/ncomms7438. URL: http://dx.doi.org/10.1038/ncomms7438.

[28] Tao Wu et al. "Magnetic-field-induced charge-stripe order in the high-temperature superconductor $YBa_2Cu_3O_y$". In: *Nature* 477.7363 (Sept. 2011), pp. 191–194. DOI: 10.1038/nature10345. URL: https://doi.org/10.1038/nature10345.

[29] S. Blanco-Canosa et al. "Momentum-Dependent Charge Correlations in $YBa_2Cu_3O_{6+\delta}$ Superconductors Probed by Resonant X-Ray Scattering: Evidence for Three Competing Phases". In: *Physical Review Letters* 110.18 (May 2013). DOI: 10.1103/physrevlett.110.187001. URL: https://doi.org/10.1103/physrevlett.110.187001.

[30] M. Hashimoto et al. "Direct observation of bulk charge modulations in optimally doped $Bi_{1.5}Pb_{0.6}Sr_{1.54}CaCu_2O_8 + \delta$". In: *Physical Review B* 89.22 (June 2014). DOI: 10.1103/physrevb.89.220511. URL: https://doi.org/10.1103/physrevb.89.220511.

[31] J. Chang et al. “Direct observation of competition between superconductivity and charge density wave order in $YBa_2Cu_3O_{6.67}$”. In: *Nature Physics* 8.12 (Oct. 2012), pp. 871–876. DOI: 10.1038/nphys2456. URL: https://doi.org/10.1038/nphys2456.

[32] K. Fujita et al. “Simultaneous Transitions in Cuprate Momentum-Space Topology and Electronic Symmetry Breaking”. In: *Science* 344.6184 (May 2014), pp. 612–616. DOI: 10.1126/science.1248783. URL: https://doi.org/10.1126/science.1248783.

[33] J. M. Tranquada et al. “Coexistence of, and Competition between, Superconductivity and Charge-Stripe Order in $La_{1.6x}Nd_{0.4}Sr_xCuO_4$”. In: *Physical Review Letters* 78.2 (Jan. 1997), pp. 338–341. ISSN: 1079-7114. DOI: 10.1103/physrevlett.78.338. URL: http://dx.doi.org/10.1103/PhysRevLett.78.338.

[34] Götz Seibold et al. “Strange metal behaviour from charge density fluctuations in cuprates”. In: *Communications Physics* 4.1 (Jan. 2021). DOI: 10.1038/s42005-020-00505-z. URL: https://doi.org/10.1038/s42005-020-00505-z.

[35] European Synchrotron Radiation Facility. *RESONANT INELASTIC X-RAY SCATTERING END STATION*. URL: http://www.esrf.eu/home/UsersAndScience/Experiments/EMD/ID32/RIXS.html. (accessed: 08.03.2021).

[36] P. Abbamonte. “A Structural Probe of the Doped Holes in Cuprate Superconductors”. In: *Science* 297.5581 (July 2002), pp. 581–584. DOI: 10.1126/science.1070903. URL: https://doi.org/10.1126/science.1070903.

[37] Alfred Q. R. Baron. *Introduction to High-Resolution Inelastic X-Ray Scattering*. 2015. eprint: arXiv:1504.01098.

[38] Frank de Groot and Akio Kotani. *Core Level Spectroscopy of Solids*. CRC Press, Mar. 2008. DOI: 10.1201/9781420008425. URL: https://doi.org/10.1201/9781420008425.

[39] Hlynur Gretarsson et al. “IRIXS: a resonant inelastic X-ray scattering instrument dedicated to X-rays in the intermediate energy range”. In: *Journal of Synchrotron Radiation* 27.2 (Feb. 2020), pp. 538–544. DOI: 10.1107/s1600577519017119. URL: https://doi.org/10.1107/s1600577519017119.

[40] N.B. Brookes et al. “The beamline ID32 at the ESRF for soft X-ray high energy resolution resonant inelastic X-ray scattering and polarisation dependent X-ray absorption spectroscopy”. In: *Nuclear Instruments and Methods in Physics Research Section A: Accelerators, Spectrometers, Detectors and Associated Equipment* 903 (Sept. 2018), pp. 175–192. DOI: 10.1016/j.nima.2018.07.001. URL: https://doi.org/10.1016/j.nima.2018.07.001.

[41] L. Braicovich et al. “The simultaneous measurement of energy and linear polarization of the scattered radiation in resonant inelastic soft x-ray scattering”. In: *Review of Scientific Instruments* 85.11 (Nov. 2014), p. 115104. DOI: 10.1063/1.4900959. URL: https://doi.org/10.1063/1.4900959.

[42] K. Kummer et al. “RixsToolBox: software for the analysis of soft X-ray RIXS data acquired with 2D detectors”. In: *Journal of Synchrotron Radiation* 24.2 (Feb. 2017), pp. 531–536. DOI: 10.1107/s1600577517000832. URL: https://doi.org/10.1107/s1600577517000832.

[43] M Moretti Sala et al. “Energy and symmetry of dd excitations in undoped layered cuprates measured by Cu L_3 resonant inelastic x-ray scattering”. In: *New Journal of Physics* 13.4 (Apr. 2011), p. 043026. DOI: 10.1088/1367-2630/13/4/043026. URL: https://doi.org/10.1088/1367-2630/13/4/043026.

[44] L. Braicovich et al. “Magnetic Excitations and Phase Separation in the Underdoped $La_{2-x}Sr_xCuO_4$ Superconductor Measured by Resonant Inelastic X-Ray Scattering”. In: *Physical Review Letters* 104.7 (Feb. 2010). DOI: 10.1103/physrevlett.104.077002. URL: https://doi.org/10.1103/physrevlett.104.077002.

[45] *d-d Excitations in Transition-Metal Oxides*. Springer Berlin Heidelberg, Dec. 2000. DOI: 10.1007/3-540-45342-3. URL: https://doi.org/10.1007/3-540-45342-3.

[46] “Ligand field theory and its applications”. In: *Choice Reviews Online* 38.07 (Mar. 2001), pp. 38–3916–38–3916. DOI: 10.5860/choice.38-3916. URL: https://doi.org/10.5860/choice.38-3916.

[47] Matteo Rossi et al. “Experimental Determination of Momentum-Resolved Electron-Phonon Coupling”. In: *Phys. Rev. Lett.* 123 (2 July 2019), p. 027001. DOI: 10.1103/PhysRevLett.123.027001. URL: https://link.aps.org/doi/10.1103/PhysRevLett.123.027001.

[48] Lucio Braicovich et al. “Determining the electron-phonon coupling in superconducting cuprates by resonant inelastic x-ray scattering: Methods and results on $Nd_{1+x}Ba_{2-x}Cu_3O_{7-\delta}$”. In: *Phys. Rev. Research* 2 (2 May 2020), p. 023231. DOI: 10.1103/PhysRevResearch.2.023231. URL: https://link.aps.org/doi/10.1103/PhysRevResearch.2.023231.

[49] Roberto Fumagalli et al. “Polarization-resolved Cu L_3-edge resonant inelastic x-ray scattering of orbital and spin excitations in $NdBa_2Cu_3O_{7\delta}$”. In: *Physical Review B* 99 (Apr. 2019). DOI: 10.1103/PhysRevB.99.134517.

[50] Nan Yang et al. “Charge localization at the interface between La1-xSrxMnO_3 and the ”infinite layers” cuprate $CaCuO_2$”. In: *Journal of Applied Physics*

112.12 (Dec. 2012), p. 123901. DOI: 10.1063/1.4768680. URL: https://doi.org/10.1063/1.4768680.

[51] G. Chabot-Couture et al. "Polarization dependence and symmetry analysis in indirect K-edge RIXS". In: (2010). DOI: 10.1103/PhysRevB.82.035113. eprint: arXiv:1003.5348.

[52] Jiemin Li et al. "Multiorbital charge-density wave excitations and concomitant phonon anomalies in $Bi_2Sr_2LaCuO_{6+\delta}$". In: (2020). DOI: 10.5281/ZENODO.3890415. URL: https://zenodo.org/record/3890415.

[53] John A. Hertz. "Quantum critical phenomena". In: *Physical Review B* 14.3 (Aug. 1976), pp. 1165–1184. DOI: 10.1103/physrevb.14.1165. URL: https://doi.org/10.1103/physrevb.14.1165.

[54] A. J. Millis. "Effect of a nonzero temperature on quantum critical points in itinerant fermion systems". In: *Physical Review B* 48.10 (Sept. 1993), pp. 7183–7196. DOI: 10.1103/physrevb.48.7183. URL: https://doi.org/10.1103/physrevb.48.7183.

[55] G. Seibold et al. "Supplementary Information: Strange metal behaviour from charge density fluctuations in cuprates". This work has not yet been completed and published. 2020.

[56] Andrew R Conn, Nicholas IM Gould, and Philippe L Toint. *Trust-region methods*. 2000.

[57] Subir Sachdev. *Quantum Phase Transitions*. Cambridge University Press, 2009. DOI: 10.1017/cbo9780511973765. URL: https://doi.org/10.1017/cbo9780511973765.

Politecnico di Milano

P.zza Leonardo da Vinci 32, Building 8
20133 Milano (MI)

www.fisi.polimi.it/en